CHEMICAL REVIEWS

pubs.acs.org/CR

Review

Noble-Metal Nanoframes and Their Catalytic Applications

Tung-Han Yang, Jaewan Ahn, Shi Shi, Peng Wang, Ruoqi Gao, and Dong Qin*

Cite This: *Chem. Rev.* 2021, 121, 796–833

Read Online

ACCESS | Metrics & More | Article Recommendations

ABSTRACT: Noble-metal nanoframes consisting of interconnected, ultrathin ridges have received considerable attention in the field of heterogeneous catalysis. The enthusiasm arises from the high utilization efficiency of atoms for significantly reducing the material loading while enhancing the catalytic performance. In this review article, we offer a comprehensive assessment of research endeavors in the design and rational synthesis of noble-metal nanoframes for applications in catalysis. We start with a brief introduction to the unique characteristics of nanoframes, followed by a discussion of the synthetic strategies and their controls in terms of structure and composition. We then present case studies to elucidate mechanistic details behind the synthesis of mono-, bi-, and multimetallic nanoframes, as well as heterostructured and hybrid systems. We discuss their performance in electrocatalysis, thermal catalysis, and photocatalysis. Finally, we highlight recent progress in addressing the structural and compositional stability issues of nanoframes for the assurance of robustness in catalytic applications.

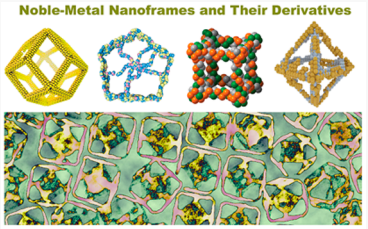

CONTENTS

1. INTRODUCTION

Heterogeneous catalysis built around noble-metal nanocrystals is central to the chemical, energy, and automobile industries.[1−4] Over the past several decades, nanocrystals made of Pd, Pt, Rh, Ru, Ir, Ag, and Au and combinations of those have received great interest owing to their favorable electronic structures for achieving high catalytic activity and/or selectivity toward a broad spectrum of reactions. These materials often exhibit their

Special Issue: Advanced Materials and Methods for Catalysis and Electrocatalysis by Transition Metals

Received: August 31, 2020
Published: December 4, 2020

https://dx.doi.org/10.1021/acs.chemrev.0c00940
Chem. Rev. 2021, 121, 796–833

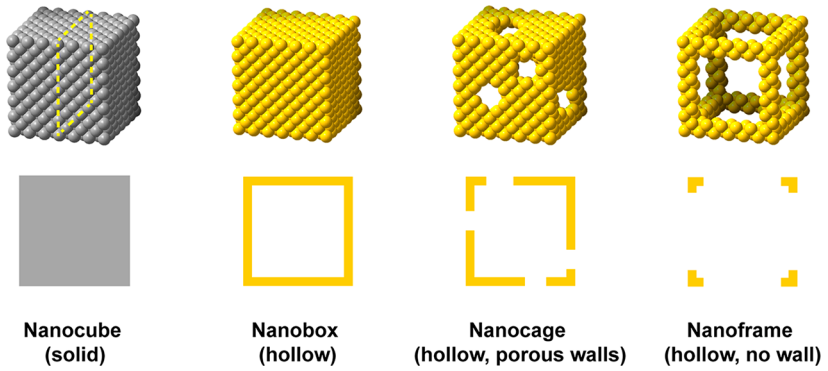

Figure 1. (top) Atomic models of a nanocube (with a solid interior), nanobox (with a hollow interior), nanocage (with a hollow interior and porous walls), and nanoframe (with a hollow interior and no wall), respectively. (bottom) Cross-sectional views corresponding to the plane marked by the dashed lines.

resistance to corrosion for sustaining long-term durability in a wide variety of catalytic processes.[5−23] However, because of their extraordinary low abundances in the Earth's crust and the ever-increasing demands from various industries, there is an urgent need to utilize this extremely rare resource in a cost-effective and sustainable manner without compromising the catalytic performance. To this end, it is pivotal to maximize the mass-based catalytic activity of the noble-metal nanocrystals.

The mass activity of a catalytic material can be augmented by optimizing the size, composition, surface structure (e.g., the type of facet and defect), and/or internal structure (i.e., solid vs hollow) of the corresponding nanocrystals.[5−23] Taking an electrocatalyst as an example, its mass activity (i.e., current density per unit mass) is a product of its specific activity (i.e., current density per unit electrochemical surface area) and its specific surface area (i.e., electrochemical surface area per unit mass).[7,9,13,18,19,22,23] As expected, any increase in specific activity or enlargement in specific surface area of the electrocatalyst will augment its mass activity. It is generally accepted that the specific activity of an electrocatalyst is determined by the surface in terms of both composition and structure. When the composition is optimized, the specific activity can be further increased through the formation of a specific type of facet. In the case of an oxygen reduction reaction (ORR), it was reported that the specific activity of 12 nm Pt concave cubes enclosed by {720} high-index facets was 6.3, 1.3, and 5.7 times, respectively, as high as those of Pt cubes enclosed by {100} facets, Pt octahedra encased by {111} facets, and the commercial Pt/C catalyst covered by a mix of {111} and {100} facets.[24] This and many other examples provide a strong motivation for engineering the surface structure of noble-metal nanocrystals tailored for catalytic applications.

The specific surface area of a nanocrystal is directly proportional to the utilization efficiency of atoms or inversely proportional to the particle size. When the size of a nanocrystal is larger than tens of nanometers, most of the atoms will be buried in the bulk and wasted, because only those on the outermost surface will directly participate in the catalytic reaction.[25−27] As such, one should reduce the particle size as much as possible in an effort to increase the utilization efficiency of atoms and thus enlarge the specific surface area. Taking a 20 nm Pt cube as an example, only 6% of the atoms are located on the surface, and the specific surface area is 14 $m^2\ g^{-1}$. When the edge length of the cube is reduced to 3 nm, ∼39% of the atoms will be located on the surface, while the specific surface area will drastically increase to 93 $m^2\ g^{-1}$.[22] This back-of-envelope calculation suggests that, in many cases, engineering the surface structure (or composition) of a catalytic material alone is not adequate to maximize the mass activity. One also needs to improve the utilization efficiency of atoms and thus increase the specific surface area by downsizing the catalytic particles. This argument justifies the popular use of Pt particles of 3−5 nm in diameter as the commercial catalyst toward ORR. At such small sizes, however, it becomes extremely difficult to enhance their specific activity by precisely engineering the surface structure, creating a dilemma for maximizing the mass activity.[27] Furthermore, the catalytic durability of such minuscule particles tends to be plagued by dissolution or detachment from the support, in addition to sintering into larger particles, during the catalytic operation.[28] To a large extent, this durability issue can be attributed to the small contact area between a tiny particle and the catalytic support, leading to a weakened interaction.

The aforementioned dilemma can be addressed by switching from conventional solid particles to hollow nanocrystals featuring a highly open structure.[22,23,29−32] Notable examples include nanoboxes, nanocages, and nanoframes, as illustrated in Figure 1. In terms of structure, the primary difference between these hollow nanocrystals lies in the porosity of their walls. Nanoboxes typically have pore-free walls that effectively isolate the hollow interior from the external environment. In contrast, nanocages refer to hollow nanocrystals comprised of walls containing small pores that allow the inner surface to participate in the catalytic reaction.[22,29] As a result, the utilization efficiency of atoms can be almost doubled relative to that of nanoboxes. For example, when the wall thickness of a nanocage is reduced to ∼1 nm or four atomic layers, the utilization efficiency of atoms can be increased to 50%, while its surface structure can still be optimized to match a specific catalytic reaction. More significantly, such a high utilization efficiency is essentially independent of the overall size of the nanocages. At a larger size, the nanocages will become less susceptible to dissolution, detachment, and sintering during the catalytic reaction because of the increase in contact area with the supporting substrate.[22,29] In a previous study, it was reported that the mass activity of 14 nm Pt icosahedral nanocages featuring {111} facets, twin boundaries, and ultrathin (1.3 nm) walls only dropped from 1.28 to 0.76 A mg_{Pt}^{-1} after 5000 cycles of an accelerated durability test, and the terminal activity was still much greater than the original activity of the commercial Pt/C catalyst.[33] Despite the successes in fabricating mono-, bi-, and trimetallic nanocages, it remains a challenge to control the size and distribution of the pores in the walls. In particular, when the pores are too small, the

https://dx.doi.org/10.1021/acs.chemrev.0c00940
Chem. Rev. 2021, 121, 796−833

nanocages would become inefficient to catalyze reactions that involve relatively large molecules.

Among the three types of hollow nanocrystals, the surface atoms on nanoframes are the most accessible to reactant and solvent molecules of different sizes, because nanoframes consist of interconnected ridges only, with no wall at all.[30−32] In essence, each ultrathin (typically, <5 nm) ridge of a nanoframe can be considered as a nanorod or a linear aggregation of nanoparticles fused together through oriented attachment. As illustrated in Figure 2, for example, a cubic nanoframe can be considered as a highly open architecture assembled from 12 nanorods. Although it remains a challenge to engineer the surface structure of the ultrathin ridges of a nanoframe through a facet-controlled synthesis, the ridges typically contain high densities of low-coordination atoms on the surface.[30−32,34−37] Additionally, during the synthesis of nanoframes, the use of oxidative etching and/or galvanic replacement often results in the formation of surfaces enriched in atomic steps, vacancies, dislocations, stacking faults, as well as grain and twin boundaries featuring lattice strains.[34−37] These active sites can be leveraged to increase the specific activity and thus augment catalytic performance toward various reactions. Altogether, nanoframes offer a multitude of advantages for catalysis, including a large surface-to-volume ratio, highly reactive surface, and enhancement in terms of catalytic activity and durability. In a study reported in 2014, rhombic dodecahedral nanoframes made of Pt_3Ni, together with an overall size of 20.1 nm and 24 ridges of ∼2 nm in thickness, exhibited a mass activity of 5.7 A mg_{Pt}^{-1} at 0.9 V toward ORR, far exceeding the 2020 target (0.44 A mg_{Pt}^{-1} at 0.9 V) set by the U.S. Department of Energy (DOE).[38] Remarkably, the nanoframes also exhibited superior durability relative to the commercial Pt/C catalyst during an accelerated durability test.

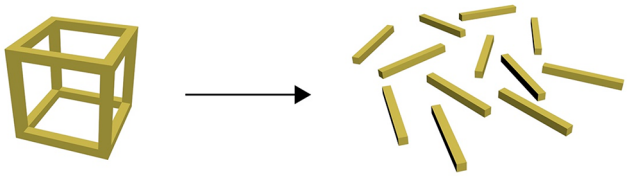

Figure 2. Model of a cubic nanoframe, which can be considered as a 3-D assembly of 12 identical nanorods.

Table 1. Summary of Metal Nanoframes That Have Been Successfully Synthesized Using the Five Different Methods

synthetic method	metals	shape/morphology	refs
template-assisted assembly of nanoscale building blocks	Au	triangle, tripod	52, 53
face-selected carving of solid nanocrystals	Pd	cube, octahedron, cuboctahedron, concave cube	54, 55
	Pt−Cu	octahedron, rhombic dodecahedron	56, 57
	Pt−Ni	octahedron, rhombic dodecahedron, tetrahexahedron	38, 43, 58−60
	Rh−Cu	octahedron, truncated octahedron, pentagonal rod	61, 62
	Pt−Cu−Co	rhombic dodecahedron	63
	Pt−Ni−Co	hexapod	64
	Pt−Ni−Sn	rhombic dodecahedron	65
	Au@Pd	cube	66
edge-selected deposition of a different metal on a template, followed by etching	Au−Ag	cube, octahedron, decahedron, icosahedron, pentagonal rod, triangle	34, 67−70
	Ag−Pd	cube, triangle	70−72
	Pt−Au	triangle	48
	Pt−Pd	cube	73
	Pt−Cu	decahedron, octopod, concave octopod	35, 36
	Ru−Pd	octahedron, cuboctahedron	74, 75
	Rh−Pd	cube	76
	Ir−Cu	rhombic dodecahedron	77
	Ir−Ni	rhombic dodecahedron	78
	Ag−Au−Pt	cube	79
	Pt−Cu−Mn	decahedron	37
	Ir−Ni−Cu	double-layered rhombic dodecahedron	44
	Pt−Cu@Pt−Cu−Ni	rhombic dodecahedron	50
dealloying of hollow alloy nanocrystals	Au−Ag	cube	41, 42
	Ir−Cu−Au	rhombic dodecahedron	77
	Au@Au	cube, truncated octahedron	80
	Pd@Au	cube, truncated octahedron	80
	Pt@Au	cube, truncated octahedron	80
nanoframe-directed deposition	Pt@Au	cube, octahedron, triangle, ring, hexagon	81, 82
	Pt−Au@Au	double-layered triangle, ring, hexagon, tripod	45
	Pt−Ni@Au	rhombic dodecahedron	83
	Au@Cu_2O	cube	46
	AgCl@Ag	cube	47
	Pt−Ni@MOF	rhombic dodecahedron	49

https://dx.doi.org/10.1021/acs.chemrev.0c00940
Chem. Rev. 2021, 121, 796−833

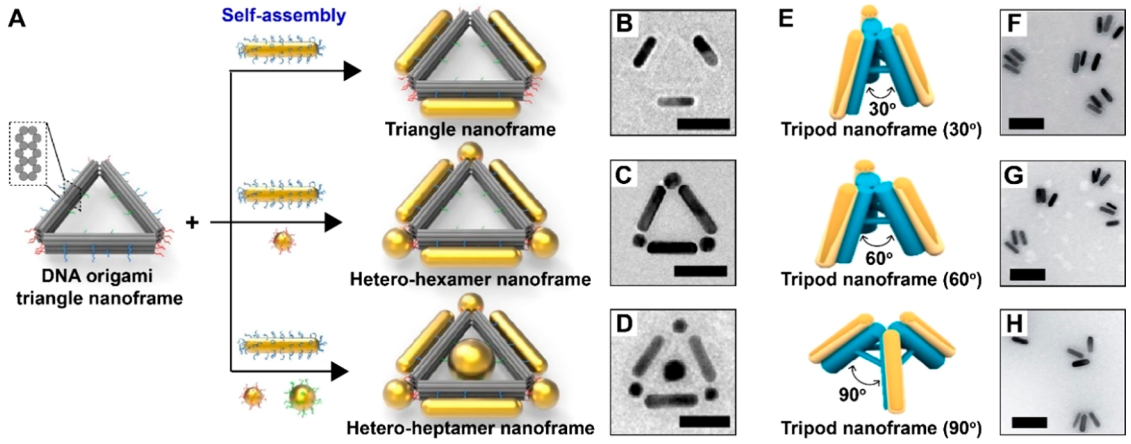

Figure 3. (A) Schematic illustration showing the formation of nanoframes containing isotropic and anisotropic Au nanostructures using the DNA origami technique. The hybridization of DNA-functionalized Au nanorods and/or Au nanoparticles (yellow color) with complementary probe strands on the DNA 2-D origami triangle nanoframe (gray color) resulted in the formation of Au-based 2-D triangle, heterohexamer, and heteroheptamer nanoframes. (B–D) TEM images of the a self-assembled (B) triangle, (C) heterohexamer, and (D) heteroheptamer nanoframe. Scale bars: 50 nm. (E) Schematic illustration showing the formation of reconfigurable DNA 3-D origami tripod nanoframes (blue color) from Au nanorods (yellow color). By controlling the interarm angles of the DNA origami tripod templates via a toehold-mediated strand-displacement reaction, the internanorod angles of the 3-D Au nanorod-based tripod nanoframes could be tuned. (F–H) TEM images of the self-assembled 3-D Au nanorod-based tripod nanoframes with the internanorod angles approaching (F) 30°, (G) 60°, and (H) 90°. Scale bars: 100 nm. (A–D) Modified with permission from ref 52. Copyright 2017 Wiley-VCH Verlag GmbH & Co. (E–H) Modified with permission from ref 53. Copyright 2017 American Chemical Society.

In addition to their attractive features for catalysis, nanoframes made of Au and Ag are promising plasmonic materials, because their cavities can be used to localize and manipulate the light at the nanoscale.[39−42] For example, on the basis of the results from experimental and computational studies, cubic nanoframes made of a Au−Ag alloy could generate intense electric fields in the interior, as well as at the outer corners, with their intensities comparable to those at the corner sites of Ag nanocubes.[39,40] In particular, by manipulating the length and thickness of the ridges, the localized surface plasmon resonance (LSPR) peaks of Ag−Ag nanoframes could be tuned from the visible to the near-infrared region.[41,42] These results suggest that nanoframes offer a highly tunable system to maneuver the plasmon-enhanced light−matter interaction for various applications.

The first synthesis of noble-metal nanoframes was reported in 2007.[41] The authors fabricated Au-based cubic nanoframes by selectively removing the Ag atoms from Au−Ag alloy nanoboxes using an aqueous etchant based on $Fe(NO_3)_3$ or NH_4OH. Thanks to the incredible progress in recent years, now it is feasible to design and rationally fabricate nanoframes with tunable compositions and morphologies to achieve the desired properties for catalytic and plasmonic applications.[30−32] Notable examples include those mainly comprised of one of the noble metals, as well as their bi- and trimetallic combinations. Note that it is insufficient to only use "composition" to describe a bi- or trimetallic system, because their properties are also strongly dependent on the spatial distributions and atomic ordering of the constituent elements.[7] With the recent development in nanochemistry, it is feasible to control the spatial distributions of constituent elements and, thus, the directionality of nanoscale phase segregation in bimetallic nanoframes.[38,43] This ability allows one to control the compositional heterogeneity on the surface of a bimetallic nanoframe, promising enhanced catalytic performance. Today, nanoframes with many distinctive morphologies have been reported, including those in the architecture of a three-dimensional (3-D) cube, cuboctahedron, octahedron, rhombic dodecahedron, decahedron, icosahedron, tripod, hexapod, and pentagonal rod, as well as a two-dimensional (2-D) triangle, hexagon, and circle.[30−32] Additionally, nanoframes such as octopods enclosed by high-index facets have been prepared in high yields.[35] Remarkably, nanoframes featuring complex and/or hybrid structures have also been realized.[44−51] These new variants have enabled a wide variety of applications, including those related to catalysis for energy conversion and environmental protection, as well as plasmonically enhanced spectroscopy and photothermal cancer therapy.

Herein, we aim to present a comprehensive account of noble-metal nanoframes, with a focus on our current understanding of their synthetic methods, unique properties, and catalytic applications. We start with a brief introduction to the synthetic strategies, mainly including a template-assisted assembly of nanoscale building blocks, template-directed deposition, etching, dealloying of atoms, or a combination of these processes. We then present a number of representative case studies from the literature to illustrate the critical concepts and elucidate the underlying mechanisms. Next, we showcase progress in leveraging the unique features of noble-metal nanoframes for developing catalysts with enhanced performance. Finally, we discuss strategies for improving the thermal and chemical stability of noble-metal nanoframes. Throughout our discussion, we also provide perspectives with regard to the challenges and future directions of development for this relatively new form of noble-metal nanocrystals.

2. SYNTHETIC APPROACHES

The synthesis of noble-metal nanoframes typically involves the use of a sacrificial template to assist or direct the formation of a framelike structure, and the template is often fabricated in advance using a different protocol. Here we broadly divide the methods into five categories: template-assisted assembly of nanoscale building blocks;[52,53] face-selected carving of solid nanocrystals;[38,43,54−66] edge-selected deposition of a different metal on a template, followed by etching;[34−37,44,48,50,67−79] dealloying of hollow alloy nanocrystals;[41,42,77,80] and nano-

https://dx.doi.org/10.1021/acs.chemrev.0c00940
Chem. Rev. 2021, 121, 796−833

frame-directed deposition.[45−47,49,81−83] Table 1 lists the nanoframes, diverse in shape/morphology and composition, that have been fabricated using these methods.

2.1. Template-Assisted Assembly of Nanoscale Building Blocks

As illustrated in Figure 2, a nanoframe can be conceptually viewed as an end-to-end assembly of multiple nanorods. In this regard, the assembly of nanoscale building blocks offers an attractive route to nanoframes. With the advancement of a deoxyribonucleic acid (DNA) origami technique that involves the programmable folding of a single-stranded DNA by numerous helper strands, it is possible to obtain arbitrary 2-D and 3-D DNA origami nanostructures with controls in spatial addressability and shapes.[52,53,84,85] For example, DNA origami nanostructures have been created in the forms of a 2-D square and triangle and a 3-D cube, ellipsoid, hemisphere, tetrahedron, and toroid.[84,85] By maneuvering the individual helper strand to create a sequence-dependent surface tag, one can use the diverse framelike DNA origami nanostructures with addressable binding sites as a template for the programmable organization of nanoparticles, nanorods, or a combination of them, into nanoframes. In particular, this approach offers a promising route to the fabrication of complex nanoframes that are difficult to obtain using a conventional wet-chemical synthesis, making it feasible to increase the structural diversity of nanoframes for achieving distinctive properties. Many recent studies of the DNA origami technique focused on the use of Au-based nanostructures as the building blocks.[85] As such, the optical properties of the resultant nanoframes can be tailored by controlling the geometric features, including the size and aspect ratio of the building blocks, as well as the separation and orientation between the constituent components.

Figure 3A demonstrates how the unique structural feature of a 2-D triangular DNA origami frame can provide a template to direct the assembly of both isotropic and anisotropic Au nanoparticles into nanoframes.[52] The triangular DNA origami frame (50 nm in edge length) was created by folding a single-stranded circular genomic DNA through a set of short-staple strands. Its interior and exterior edges and vertices were functionalized to establish the binding sites for the attachment of DNA-functionalized Au nanorods (12 nm in width and 37 nm in length) and nanoparticles (15 or 25 nm in diameter). Specifically, the exterior edges of the frame were decorated with one set of seven copies of single-stranded DNA probes (blue color) to attach Au nanorods; the vertices of the frame were modified with one set of six copies of single-stranded DNA overhangs (red color) to anchor 15 nm Au nanoparticles; and the interior edges of the frame were presented with six single-stranded DNA capture strands to secure 25 nm Au nanoparticles in the center. Transmission electron microscopy (TEM) confirmed that the Au nanoparticles and nanorods were placed at the specific positions on the origami surface to form unique nanoframes in the forms of a triangle (Figure 3B), heterohexamer (Figure 3C), and heteroheptamer (Figure 3D), respectively, after the hybridization of the designed DNA origami template with the Au-based building blocks.

In addition to the aforementioned 2-D nanoframes, 3-D nanoframes could be fabricated through the programmable transformation of DNA origami decorated with Au nanostructures. As illustrated in Figure 3E, three DNA-functionalized Au nanorods (12 nm in width and 38 nm in length) were assembled onto a reconfigurable DNA origami tripod consisting of three arms for the construction of a 3-D nanoframe.[53] Each arm (50 nm in length) of the DNA origami tripod had 14 DNA duplexes packed into a honeycomb lattice to accommodate the curvature of the Au nanorods. Remarkably, by tuning the interarm angles (~30°, 60°, or 90°) of the DNA origami tripod template via a toehold-mediated strand-displacement reaction, the angle between adjacent nanorods could be tuned, as demonstrated by the TEM images in Figure 3F−H.

In summary, DNA-based self-assembly provides a powerful tool for the rational fabrication of customized nanoframes in considerable complexity by incorporating noble-metal building blocks presynthesized with proper sizes and shapes. The as-fabricated nanoframes offer a well-controlled system for tuning the plasmonic properties. As a major drawback, this self-assembly approach involving molecular interactions in highly ionic solutions is often limited by structural instability, complex experimental procedures, low throughput, and small production volume. These technical issues will eventually limit the scale and scope of applications for the nanoframes fabricated using this method.

2.2. Face-Selected Carving of Solid Nanocrystals

Figure 4 illustrates two wet-chemical methods that leverage the intrinsic surface inhomogeneity to selectively carve atoms from

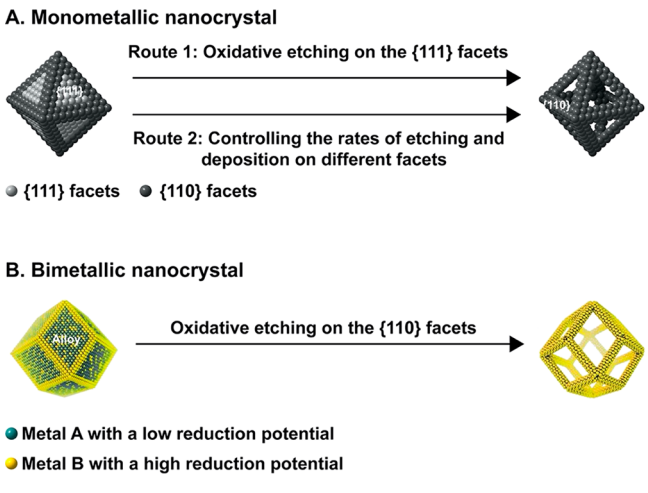

Figure 4. Schematic illustration of two protocols that rely on the carving of atoms from side faces for the transformation of (A) monometallic octahedron and (B) bimetallic rhombic dodecahedron into a nanoframe. (A) Modified with permission from ref 55. Copyright 2017 American Chemical Society. (B) Modified with permission from ref 38. Copyright 2014 AAAS.

solid nanocrystals for their transformation into nanoframes. For a monometallic nanocrystal, surface inhomogeneity exists among atoms located at faces, edges, and vertices due to their difference in coordination number. It can also arise from crystallographic defects such as a vacancy, dislocation, and twin/grain boundary. In general, the site with the highest surface free energy is most vulnerable to oxidative etching. For example, an octahedral nanocrystal made of a face-centered cubic (fcc) metal, enclosed by {111} facets for the faces, {100} facets for the vertices, and {110} facets for the edges, can be transformed into an octahedral nanoframe by carving along the faces (see Figure 4A). For nanocrystals made of noble metals, it is feasible to activate oxidative etching by combining the O_2 from air and a halide ion, such as Cl^-, Br^-, and I^-, to create an etchant.[20,22,23]

https://dx.doi.org/10.1021/acs.chemrev.0c00940
Chem. Rev. 2021, 121, 796−833

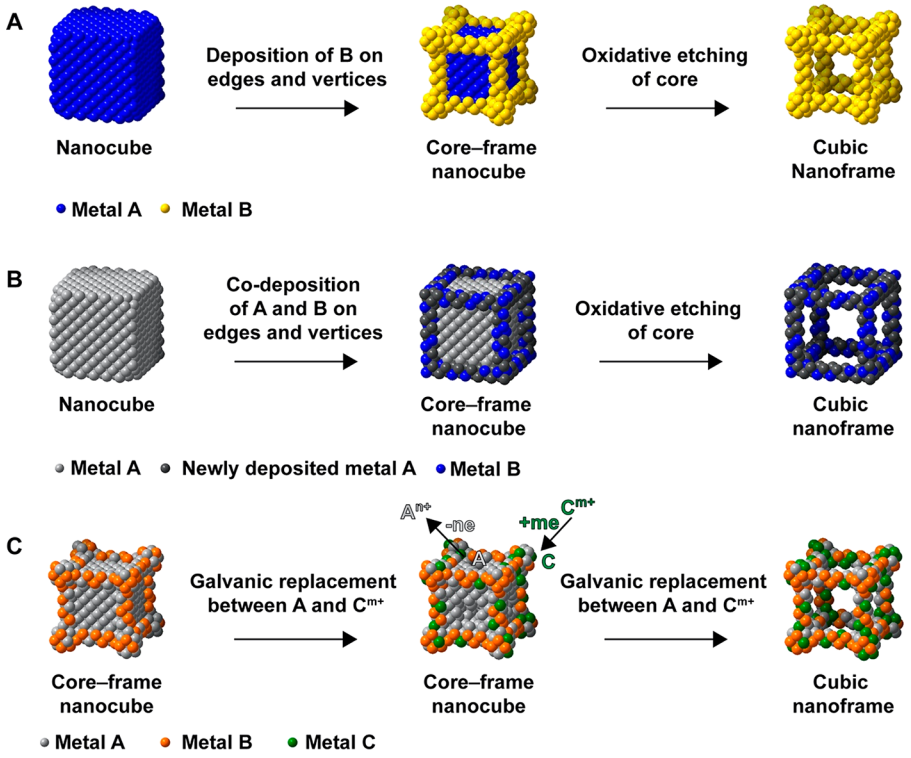

Figure 5. (A) Schematic illustration showing the fabrication of cubic nanoframes made of metal B by selectively depositing it on the edges and vertices of a nanocube made of metal A, followed by the selective removal of metal A in the core via etching. (B) Schematic illustration showing the fabrication of nanoframes made of an A–B alloy through a site-selected codeposition of A and B on the edges and vertices of a nanocube made of metal A, followed by the removal of metal A in the core via etching. (C) Schematic illustration showing the fabrication of nanoframes made of an A–B–C alloy by titrating C^{m+} ions into an aqueous suspension of A@A–B core–frame nanocubes to induce a galvanic replacement with metal A in the core. (A) Modified with permission from ref 76. Copyright 2016 Wiley-VCH Verlag GmbH & Co. (B) Modified with permission from ref 71. Copyright 2016 Wiley-VCH Verlag GmbH & Co. (C) Modified with permission from ref 79. Copyright 2019 American Chemical Society.

More interestingly, the strength of such an etchant can be tailored by varying the halide involved.

In general, it is nontrivial to level the extents of carving among different faces, making it difficult to generate nanoframes with the same thickness for all edges. This issue can be addressed by introducing a reducing agent into the reaction system to complement the carving process with deposition.[55] In this case, the metal ions derived from oxidative etching can be reduced to atoms for their redeposition onto the nanocrystal but likely at places different from the etching sites. Significantly, by choosing a reducing agent with a proper reduction power, one can control the etching and deposition rates, $R_{etching}$ and $R_{deposition}$, to balance these two processes at different sites on the nanocrystal. When $R_{etching}$ is greater than $R_{deposition}$ on faces but comparable to $R_{deposition}$ along edges and vertices, the carving will be largely confined to the faces, while leaving the edges and vertices intact, for the transformation of a solid nanocrystal into a nanoframe.

Moving beyond the monometallic system, Figure 4B illustrates the capability of a face-selected carving to transform a bimetallic nanocrystal into an alloy nanoframe in the rhombic dodecahedral shape.[38] In this case, a surface inhomogeneity originating from elemental composition determines the selectivity of carving for the different sites of a nanocrystal. Specifically, when the faces of the rhombic dodecahedron are enriched by metal A with a lower reduction potential, while the edges and vertices are dominated by metal B with a higher reduction potential, the oxidative etchant will selectively attack and dissolve atoms from the faces, while the edges and vertices will be retained. With the involvement of the Kirkendall effect,[57] a well-known phenomenon arising from the difference in diffusion rate between two interdiffusing atomic species in an alloy, it is possible to synthesize a surface-segregated bimetallic rhombic dodecahedron whose faces are enriched in metal A, while the edges and vertices are dominated by metal B (see Section 3.2).

In summary, oxidative etching offers a powerful tool to carve atoms from solid nanocrystals in a site-selected fashion for the fabrication of mono- and bimetallic nanoframes, with a possible extension to multimetallic systems. Despite the remarkable success, a mechanistic understanding of the carving process remains elusive. In most cases, people have to rely on the use of a trial-and-error approach in identifying the optimal protocols, with essentially no information on the intermediate structures and their temporal evolution. The development of in situ characterization techniques is expected to offer an opportunity to shed light on the mechanistic details underpinning the transformation from a solid nanocrystal to a nanoframe.

2.3. Edge-Selected Deposition of a Different Metal on a Template, Followed by Etching

Instead of directly carving atoms from a nanocrystal, one can selectively deposit a different metal onto its edges and vertices for the generation of a core–frame nanocrystal, followed by removal of the core through oxidative etching. Figure 5 shows three slightly different protocols that explore the landscape of surface energy in directing site-selected deposition on a cubic seed. For a cubic nanocrystal made of an fcc metal, the surface energies decrease in the order of edges, vertices, and faces when the faces are passivated by a capping agent.[86,87] As such, the

https://dx.doi.org/10.1021/acs.chemrev.0c00940
Chem. Rev. 2021, 121, 796–833

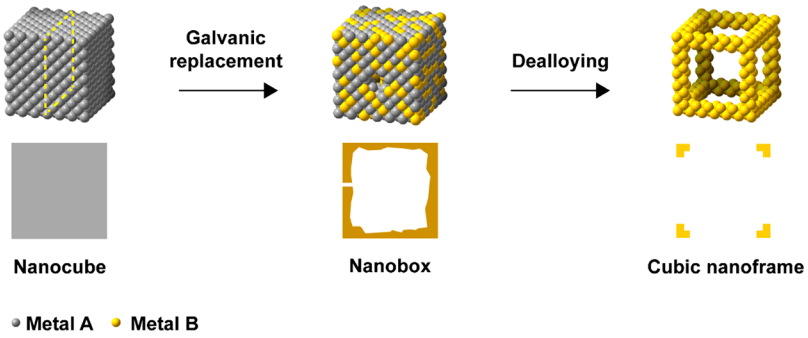

Figure 6. Schematic illustration showing the formation of an A−B alloy nanobox through a galvanic replacement reaction and then a B-based cubic nanoframe by dealloying metal A from the walls of the A−B nanobox with a chemical etchant. Modified with permission from ref 41. Copyright 2007 American Chemical Society.

second metal tends to be selectively deposited on the edges and vertices higher in energy than the faces for the generation of a core−frame nanocube. When the core is selectively etched away, a cubic nanoframe largely comprised of the second metal will be left behind.

Figure 5A illustrates the transformation of a cubic nanocrystal into a nanoframe when the metal A in the original nanocrystal is less reactive than the deposited metal B.[73,76] In this case, the B atoms derived from the reduction of a precursor should only nucleate and grow from the edges and vertices. If the rate of atom deposition is faster than that of surface diffusion to faces, the deposited B atoms will be confined to their original sites for the generation of an A@B core−frame nanocube. Upon etching of metal A from the core while leaving the frames intact, a cubic nanoframe based on metal B will be obtained. When the amount of metal B being deposited is controlled, the ridges of the nanoframes can be made as thin as a few nanometers.

When metal A is more reactive than the deposited metal B, there will be a galvanic replacement between the original nanocrystal and the salt precursor to metal B. For example, it has been well-documented that a galvanic replacement reaction will occur when Ag nanocrystals are mixed with a precursor, such as $AuCl_4^-$, $PdCl_4^{2-}$, or $PtCl_4^{2-}$, to a less reactive metal.[88] Because the original nanocrystal will be spontaneously oxidized and dissolved, partially or completely, it can no longer be used to direct the site-selected deposition of the second metal for the generation of a bimetallic nanocrystal with a core−frame structure. In this case, one can simultaneously introduce a precursor (e.g., A^{n+} ions) to metal A to help push back the galvanic replacement reaction, together with the use of a faster reduction reaction to compete with and thereby suppress the galvanic reaction.[69,71] For example, when both Ag^+ and $PdCl_4^{2-}$ are cotitrated into a suspension of Ag nanocubes in the presence of a reducing agent, the added Ag^+ and $PdCl_4^{2-}$ will be quickly reduced by the reducing agent for the generation of Ag and Pd atoms without the involvement of a replacement reaction.[71] When the faces of the Ag nanocube are capped by poly(vinylpyrrolidone) (PVP), the Ag and Pd atoms will be codeposited on the edges and vertices only. Figure 5B illustrates the fabrication of an A−B alloy nanoframe through a site-selected deposition of both A and B atoms on the edges and vertices of a cubic nanocrystal made of metal A, followed by the removal of metal A in the core via oxidative etching.[71] By simply varying the feeding ratio between the two precursors during cotitration, this route offers a tight control over the ratio of atoms being deposited for the fabrication of A−B alloy nanoframes with different elemental compositions.

Instead of using a chemical etchant to remove the core from a core−frame nanocrystal for the generation of a nanoframe, one can leverage galvanic replacement to achieve the transformation. As illustrated in Figure 5C, when C^{m+} ions are introduced into an aqueous suspension of the A@A−B core−frame nanocubes shown in Figure 5B, they will undertake a galvanic replacement reaction with metal A in the core for the production of C atoms at the expense of A atoms.[79] Specifically, A atoms are oxidized and dissolved from the faces in the form of A^{n+} ions, while the resultant C atoms derived from the galvanic reaction are deposited on the edges and vertices in an orthogonal manner, leading to the formation of A−B−C trimetallic cubic nanoframes. This strategy works for various salt precursors, including $AuCl_4^-$, $PdCl_4^{2-}$, and $PtCl_4^{2-}$, and it offers an ability to exquisitely control the oxidation of metal A and thus the dissolution rate of the core by leveraging the stoichiometry involved in the galvanic replacement reaction.

In summary, a site-selected deposition of a different metal on preformed nanocrystals offers a simple and straightforward route to the fabrication of core−frame nanocrystals and then nanoframes with well-defined composition and morphology after the removal of the core. Despite the remarkable success, it remains a challenge to push such a batch-based synthesis toward the production of nanoframes in large quantities. At the current stage of development, the site-selected deposition requires the use of a titration protocol to control the local concentration of the precursor and thus promote heterogeneous nucleation/growth while eliminating homogeneous nucleation in the reaction solution.[69,71,73,74,76,79] Additionally, there is always interdiffusion between the atoms in the core and the frame during the deposition and/or etching process.[89] As a result, the final products are typically made of two or more elements.

2.4. Dealloying of Hollow Alloy Nanocrystals

As demonstrated in Section 2.2, a solid alloy nanocrystal can be transformed into a nanoframe by selectively dissolving one type of atom from the side faces through oxidative etching. In this case, the site selectivity is typically achieved by manipulating the elemental distributions among the faces, edges, and vertices when the alloy nanocrystals are synthesized. This requirement can be relaxed by switching to hollow alloy nanocrystals, in which the atoms situated on faces are typically more reactive than those at the edges and vertices due to the presence of a tensile strain on the face with an ultrathin thickness. Figure 6 illustrates this concept by showing the transformation of a solid nanocube into an alloy nanobox and then a nanoframe.[41,42] In the first step, a galvanic replacement reaction between metal A in the nanocube and a precursor to metal B is initiated on the faces

https://dx.doi.org/10.1021/acs.chemrev.0c00940
Chem. Rev. 2021, 121, 796−833

of the nanocube for the creation of pinholes, followed by the continuous carving of metal A to form a partially hollow nanostructure and finally a nanobox with pore-free walls composed of an A−B alloy. In the second step, when metal A is dealloyed using a chemical etchant, the nanobox evolves into a cubic nanoframe made of almost pure B. It is worth mentioning that the precursor used for the galvanic reaction can also serve as an etchant to facilitate the dealloying process during which the B atoms will be concomitantly produced and deposited onto the surface. However, the coupling between the dealloying of metal A and the deposition of B makes it difficult to precisely control the wall thickness and porosity of the resultant nanoframe. The quality of the hollow alloy nanocrystals fabricated using a galvanic replacement reaction also plays an essential role in determining the success of such a transformation process. In most cases, the final nanoframes are comprised of an alloy rather than a pure metal due to the difficulty in achieving complete dealloying.

2.5. Nanoframe-Directed Deposition

In principle, nanoframes can directly serve as a template for the deposition of a different metal to increase the diversity in terms of composition while improving their mechanical strength and even enhancing their catalytic and/or plasmonic properties.[45,81−83] This methodology has been applied to the fabrication of bi- and multimetallic nanoframes with a variety of compositions. Figure 7 outlines the general concept, which is

Figure 7. Schematic illustration showing the use of a preformed metal nanoframe as a seed for the deposition of another metal. Depending on the growth mode, the deposited metal can evolve into a complete shell on the ridges of the nanoframe or discrete islands (or spikes) randomly distributed on the ridges.

essentially the same as the conventional seed-mediated growth except for the use of hollow and porous nanocrystals as the seeds. Depending on the growth mode, the deposited metal can either evolve into a complete shell on the ridges of the nanoframe or grow into islands or spikes randomly distributed on the skeleton of the nanoframe.[90] The final morphology is mainly determined by the ratio between the deposition rate ($R_{deposition}$) and the surface diffusion rate ($R_{diffusion}$) of the adatoms. In general, faster diffusion favors the formation of a complete shell, whereas faster deposition favors the island growth mode. During the synthesis, the precursor for the deposited metal is typically titrated into the suspension of nanoframes in order to eliminate homogeneous nucleation. Again, there should be no galvanic replacement reaction between the nanoframes and the precursor being added. Otherwise, the nanoframes could be easily destroyed due to their ultrathin ridges. A similar protocol should be extendible to the deposition of other functional materials such as semiconductors onto the surface of metal nanoframes.[46,47,49] In practice, this method has not been widely explored in the literature primarily because of the limitation arising from the small quantities of nanoframes, as well as their structural fragility.

3. CASE STUDIES

As discussed in Section 2, noble-metal nanoframes can be fabricated using a number of different methods. In this section, we focus on some representative examples reported in the literature to further illustrate the mechanistic understanding behind each synthesis for tailoring the structures and properties of nanoframes. The examples are presented in the order of increasing complexity in terms of elemental composition and structure.

3.1. Monometallic Nanoframes

By definition, monometallic nanoframes should be comprised of one element only. The self-assembly approach discussed in Section 2.1 offers immediate access to such nanostructures by employing monometallic building blocks.[52,53] A face-selected carving of monometallic nanocrystals through oxidative etching offers an alternative approach (see Figure 4A). In an early study, Xia and co-workers demonstrated the fabrication of single-crystal Pd nanoframes.[54] In a typical experiment, the reaction solution containing Na_2PdCl_4 (a precursor to Pd), ethylene glycol (EG, a solvent and a reducing agent), water (a solvent), O_2 dissolved in water (an oxidant), and PVP (a colloidal stabilizer) was heated in air at 100 °C for 28 h. In the initial stage, the Na_2PdCl_4 was reduced by EG to generate Pd atoms. Although the presence of O_2 and Cl^- ions in the reaction solution could oxidize and dissolve the Pd atoms to a certain extent, the chemical reduction was in dominance. As such, the as-produced Pd atoms were able to nucleate and grow into nanocubes (Figure 8A). Afterward, oxidative etching of the Pd nanocubes became a dominant process because of the depletion of the precursor. Similar to a corrosion process, the etching tended to be initiated locally for the generation of small pits on the faces of the nanocubes (Figure 8B). As the etching was continued, more Pd atoms were carved out from the interior, leading to the evolution of the nanocubes into nanoboxes and then nanocages (Figure 8C). At the end, a combination of additional etching and Ostwald ripening transformed the nanocages into nanoframes (Figure 8D).

In a more recent study, Jin and co-workers refined the protocol and demonstrated the fabrication of Pd octahedral nanoframes by balancing the etching and deposition rates on different facets of a Pd octahedral nanocrystal.[55] Figure 9A outlines the typical process that includes the dispersion of preformed Pd octahedra in *N*,*N*-dimethylformamide (DMF) containing formaldehyde (HCHO, a reducing agent), KI (the source of I^- ions), and PVP (a colloidal stabilizer). Next, the reaction vessel was vacuumed and then filled with a certain amount of pure O_2 gas to form an etchant based on the O_2/I^- pair, before it was capped and heated at 100 °C for 1 h. On the one hand, during the heating process, Pd atoms were oxidized and removed from the octahedron due to the oxidative etching caused by O_2/I^- and dissolved into the solution in the form of Pd^{2+} ions. On the other hand, the dissolved Pd^{2+} ions were reduced by HCHO to generate Pd atoms for their subsequent redeposition onto the octahedron. By simply varying the

https://dx.doi.org/10.1021/acs.chemrev.0c00940
Chem. Rev. 2021, 121, 796−833

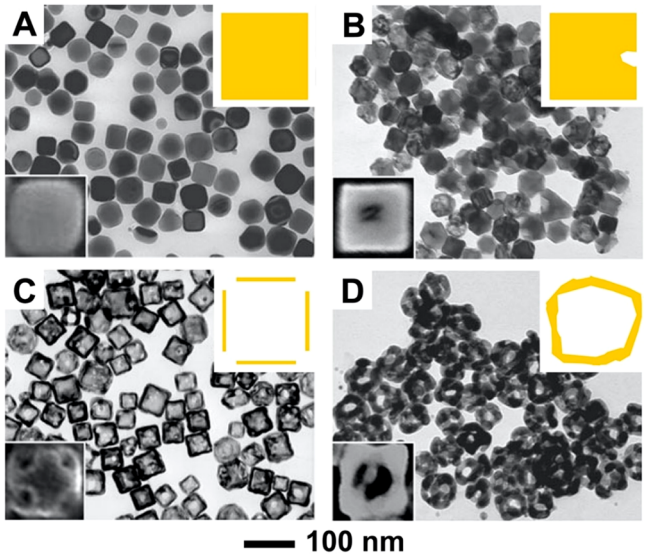

Figure 8. TEM images of the products obtained at different stages of a one-pot synthesis of Pd nanocrystals that involved reduction and oxidative etching, as well as Ostwald ripening. The lower left insets show SEM images of the individual particles taken from each sample, respectively. The models in the upper right insets illustrate the typical morphologies of the corresponding samples. Reproduced with permission from ref 54. Copyright 2005 Wiley-VCH Verlag GmbH & Co.

concentration of HCHO to maneuver the reducing power, it was feasible to manipulate the rates of oxidative etching and deposition, $R_{etching}$ and $R_{deposition}$, on the faces, edges, and vertices of the octahedron, respectively. When $R_{etching}$ became larger than $R_{deposition}$ on the faces while these two rates were comparable to each other along the edges and vertices, the Pd atoms were predominantly carved from the faces rather than the edges and vertices, leading to the evolution of a solid octahedron into an octahedral nanoframe. Figure 9 B–D shows high-angle annular dark-field scanning TEM (HAADF-STEM) images of the nanostructures obtained at different stages of the synthesis.

To our best knowledge, there are only two examples of truly monometallic nanoframes, with the first one fabricated for Au through self-assembly[52,53] and the second one synthesized for Pd by selectively carving out atoms from the faces of solid nanocrystals.[54,55] In principle, the approach based on site-selected carving should be extendible to other noble metals, but the extension has not been so straightforward. The difficulty can be attributed to the inherently greater reactivity for the atoms located at edges and vertices relative to those situated on faces. As such, the edges and vertices are more susceptible to etching than the faces. This order of reactivity can be potentially reversed by introducing a proper capping agent to selectively passivate the edges and vertices and/or an etching promotor for the faces.[86–88]

3.2. Bi- and Multimetallic Nanoframes

Most of the metal nanoframes reported in the literature contain two or more elements. Compared with the monometallic counterpart, bi- and multimetallic systems usually exhibit enhanced and tunable properties for use in catalysis due to the charge transfer between different elements and the possible synergistic effect.[7,8,22] Nevertheless, it is not a trivial task to fabricate bi- and multimetallic nanoframes with precise compositions, because it requires a dedicated control of alloying and dealloying over different length scales, as discussed in Sections 2.2–2.5.

Face-Selected Carving of Bimetallic Nanocrystals. In a study reported in 2014, Pt_3Ni rhombic dodecahedral nanoframes comprised of 24 ridges (thickness: ~2 nm) were successfully fabricated through the face-selected etching of Ni from the phase-segregated $PtNi_3$ rhombic dodecahedral nanocrystals by following the mechanism described in Figure 4B.[38] Figure 10A shows a schematic diagram that details the transformation of a $PtNi_3$ solid nanocrystal into a Pt_3Ni nanoframe. First, aqueous H_2PtCl_6 and aqueous $Ni(NO_3)_2$ were mixed in oleylamine (OAm), followed by heating to 160 °C to remove the water and then to 270 °C for 3 min to obtain $PtNi_3$ rhombic dodecahedral nanocrystals. The $PtNi_3$ nanocrystals were then collected and redispersed in hexadecane in the presence of OAm, followed by aging in air at 120 °C for 12 h to produce Pt_3Ni rhombic dodecahedral nanoframes. The structural and compositional evolutions were studied using TEM (Figure 10B–D), X-ray diffraction (XRD), and energy-dispersive X-ray spectroscopy (EDS) throughout the transformation process at regular intervals. Remarkably, the nanoframes could be dispersed on a commercial carbon support and subsequently heated in an Ar atmosphere between 370 and 400 °C for the development of a Pt skin on the nanoframe via atomic diffusion (Figure 10E). It is worth mentioning that the removal

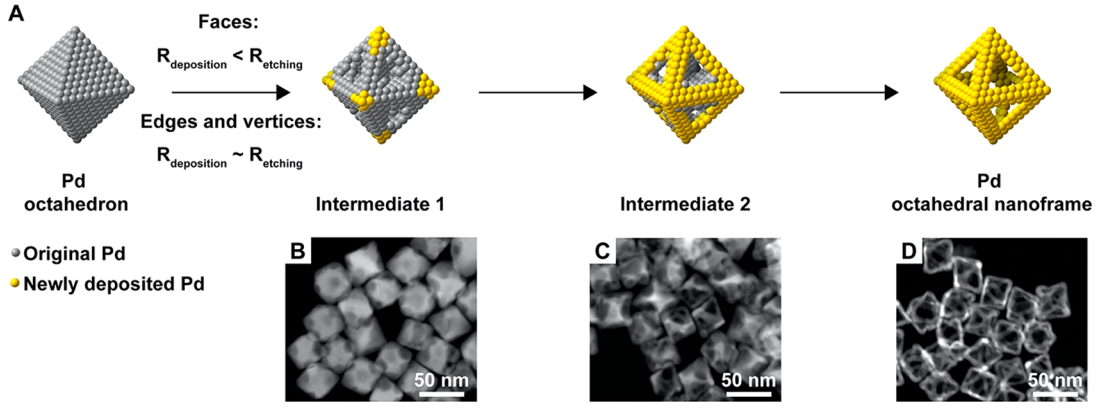

Figure 9. (A) Schematic diagram illustrating the transformation of a Pd octahedron into an octahedral nanoframe by controlling the etching and deposition rates at different sites. (B–D) HAADF-STEM images of the typical nanostructures obtained at different stages of a synthesis. Reproduced with permission from ref 55. Copyright 2017 American Chemical Society.

https://dx.doi.org/10.1021/acs.chemrev.0c00940
Chem. Rev. 2021, 121, 796–833

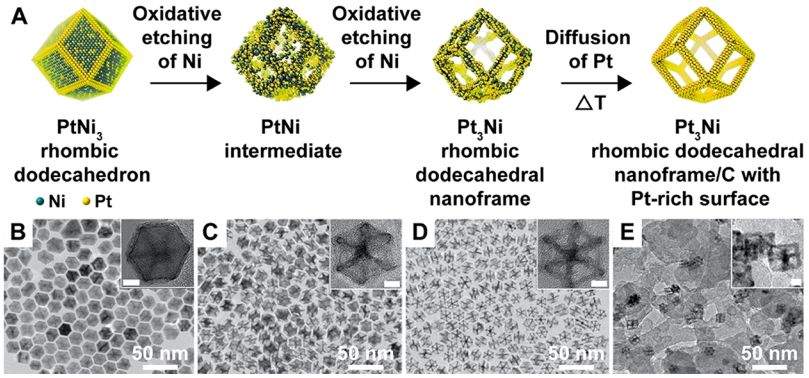

Figure 10. (A) Schematic illustration of major steps involved in the evolution from a phase-segregated $PtNi_3$ rhombic dodecahedral nanocrystal to a Pt_3Ni nanoframe with Pt-enriched surface through face-selected carving and post-synthesis thermal treatment. (B–E) TEM images of the (B) initial solid $PtNi_3$ rhombic dodecahedral nanocrystals, (C) PtNi intermediate obtained at t = 6 h, (D) Pt_3Ni nanoframes obtained at t = 12 h, and (E) Pt_3Ni nanoframes after the deposition on a carbon support and then thermal treatment to enrich the surface with Pt. The scale bars in all the insets are 5 nm. Reproduced with permission from ref 38. Copyright 2014 AAAS.

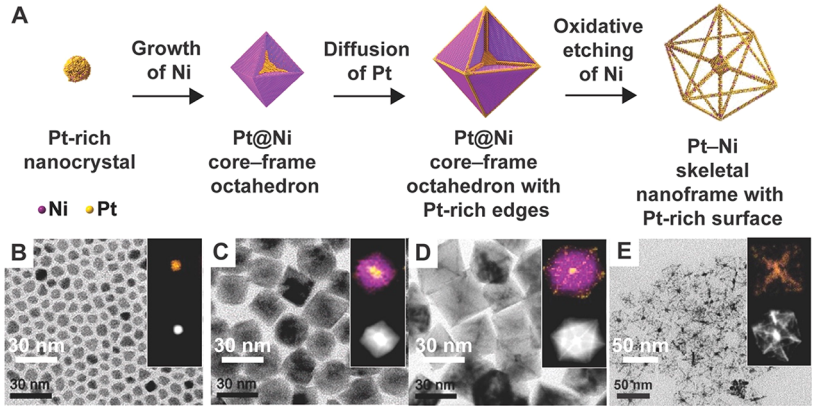

Figure 11. (A) Schematic illustration showing the formation of a Pt@Ni core–shell octahedral nanocrystal with Pt-rich edges and then a Pt–Ni skeletal nanoframe through the control of phase segregation and post-synthesis etching. (B–D) TEM images of the nanostructures obtained at different time points into a synthesis: (B) 25 min, (C) 1 h, and (D) 5 h. (E) TEM image of the final Pt–Ni skeletal nanoframes with a Pt-rich surface after the post-synthesis etching. The insets show the corresponding EDS elemental mapping. Reproduced with permission from ref 43. Copyright 2015 American Chemical Society.

of the core was a spontaneous oxidation process facilitated by the OAm adsorbed on the surface. The X-ray photoelectron spectroscopy (XPS) data revealed that the surface of the solid nanocrystals was composed of elemental Pt and partially oxidized Ni. The latter species readily formed a soluble complex with OAm for their easy removal from the nanocrystal. This process would continue, until the composition had shifted from $PtNi_3$ to PtNi and finally Pt_3Ni, at which point the composition became stable to discourage further dissolution of Ni in this manner. The carving occurred at the faces of $PtNi_3$ rhombic dodecahedra likely because of a higher Pt content at the edges and vertices (e.g., in the form of stable Pt_3Ni). Such a spatial difference in composition can be attributed to the higher reactivity associated with the low-coordination atoms at edges and vertices. The preferential dissolution of Ni from the edges and vertices would leave behind Pt atoms, increasing the fraction of Pt atoms at these sites.

In another study, Pt-enriched skeletal nanoframes were fabricated from Pt@Ni core–shell octahedral nanocrystals through geometrically induced nanoscale phase segregation.[43] Figure 11A shows a schematic of the synthesis. In a standard protocol, Pt@Ni core–shell nanocrystals were first prepared by mixing $Pt(acac)_2$, $Ni(acac)_2$ (acac = acetylacetonate), stearic acid, and octadecylamine (ODA) at 170 °C and continued with heating for 5 h under 1 atm of CO. It was argued that the CO molecule could act as both a reducing agent and a surface stabilizer. In the early stage, Pt-rich Pt–Ni nanocrystals were formed (Figure 11B) at 25 min into the synthesis. The growth of the Ni phase was followed, leading to the formation of Pt@Ni core–shell octahedral nanocrystals by t = 1 h (Figure 11C). With the increase of reaction time to 5 h, the Pt atoms migrated to the {110} facets (i.e., edges) of the octahedra through atomic diffusion, followed by phase segregation to increase the local concentration of Pt at the edges of the octahedra (Figure 11D). Afterward, the phase-segregated octahedra were placed in acetic acid and heated at 100 °C in air for 1 h to preferentially remove the Ni component, yielding Pt–Ni skeletal nanoframes with a Pt-enriched surface (Figure 11E). The corresponding elemental mapping data were shown in the insets of Figure 11B–E, demonstrating the change of Pt (yellow) and Ni (purple) distributions during the synthesis.

The roles played by CO molecules during the nanocrystal growth and phase segregation were systemically investigated in this study through a number of control experiments. When CO was replaced with inert Ar, the resultant nanocrystals became concave octahedra, and there was no surface segregation of Pt to

https://dx.doi.org/10.1021/acs.chemrev.0c00940
Chem. Rev. 2021, 121, 796–833

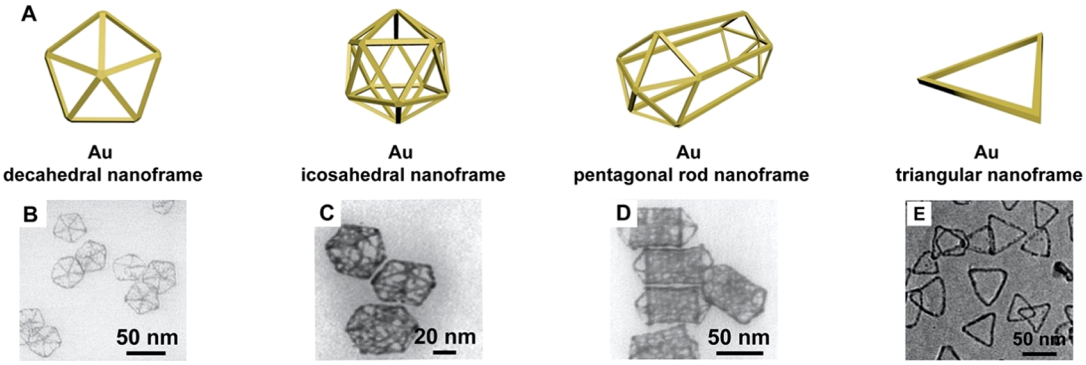

Figure 12. (A) Models of Au nanoframes in the shapes of decahedron, icosahedron, pentagonal rod, and triangle, respectively. (B–E) TEM images of the corresponding nanoframes fabricated using a similar protocol that involved edge-selected deposition and wet-chemical etching. (B–D) Reproduced with permission from ref 67. Copyright 2011 American Chemical Society. (E) Reproduced with permission from ref 68. Copyright 2013 Wiley-VCH Verlag GmbH & Co.

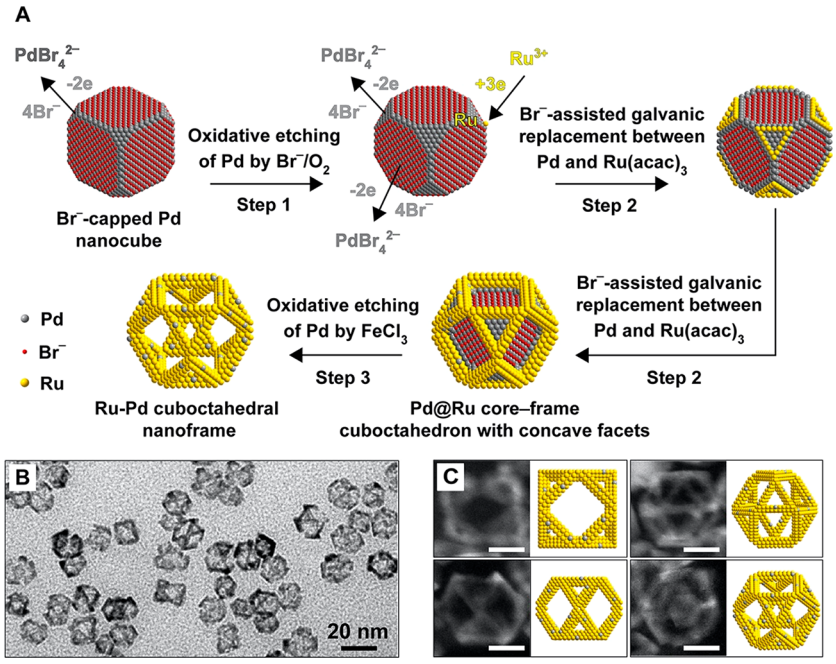

Figure 13. (A) Schematic illustration showing the major steps involved in the formation of an fcc-Ru–Pd cuboctahedral nanoframe by starting with a Br^--capped Pd nanocube. (B) TEM and (C) HAADF-STEM images, together with the corresponding models, of the cuboctahedral nanoframes viewed along the ⟨100⟩, ⟨110⟩, ⟨211⟩, and ⟨111⟩ directions, respectively. The scale bars in (C) are 5 nm. Reproduced with permission from ref 75. Copyright 2019 American Chemical Society.

the edges, suggesting the role of CO as an agent to induce the directional migration of Pt atoms. Additionally, the morphology of the phase-segregated Pt@Ni core–shell octahedral nanocrystals implied the additional role of CO as a stabilizer toward the Ni(111) surface. The authors further performed density functional theory (DFT) calculations to elucidate the mechanistic details responsible for the CO-induced stabilization.[43] When the Pt atoms diffuse from the bulk Pt–Ni alloy to the surface, they must overcome a relatively significant energy barrier in the subsurface region. When the synthesis was conducted under Ar atmosphere, the energy barrier was too high to overcome at the reaction temperature used. In contrast, with the involvement of CO molecules in the reaction for their adsorption on the surface, DFT calculations suggested that the energy barrier was significantly reduced. Although there was still a relatively high energy barrier for the bulk-to-edge diffusion, the bulk-to-vertex diffusion became a thermodynamically favorable process, leading to the formation of Pt pillars along the ⟨100⟩ direction. It was argued that the change in internal strain energy induced by the adsorption of CO on Pt would result in the directional diffusion of Pt atoms to the {110} facets to form a connected network along all of the edges, because the {110} sites were energetically more favorable for placing Pt atoms.

Edge-Selected Deposition on a Template, Followed by Etching. In a set of studies, it was demonstrated that Au-based nanoframes could be obtained through the selective deposition of Au on the edges and vertices of Ag nanocrystals with various shapes, followed by selective removal of the Ag core (Figure 5A).[39,67−70] In one report, Ag decahedra, icosahedra, or pentagonal rods were reacted with $HAuCl_4$ in the presence of ascorbic acid (a reducing agent) and KOH (a reagent to adjust the reduction power of ascorbic acid), followed by the addition of H_2O_2 to selectively remove the Ag core for the generation of nanoframes with various morphologies (Figure 12B–D).[67] This

https://dx.doi.org/10.1021/acs.chemrev.0c00940
Chem. Rev. 2021, 121, 796–833

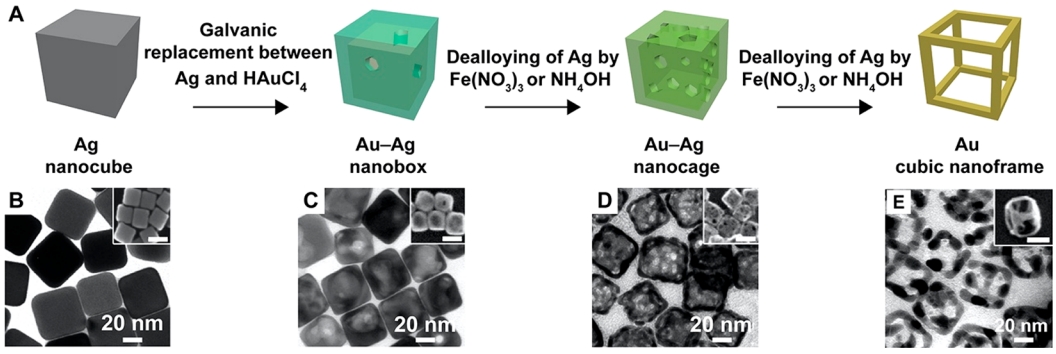

Figure 14. (A) Schematic illustration showing the formation of a Au−Ag nanobox, Au−Ag nanocage, and then a Au cubic nanoframe via galvanic replacement and the dealloying of Ag atoms with an aqueous etchant based on $Fe(NO_3)_3$ or NH_4OH. (B−E) TEM images of (B) Ag nanocubes; (C) Au−Ag nanoboxes obtained by reacting the nanocubes with aqueous $HAuCl_4$; as well as (D) Au−Ag nanocages and (E) Au nanoframes obtained by etching the nanoboxes with different amounts of aqueous $Fe(NO_3)_3$. The insets in (B−E) are the corresponding SEM images, with the scale bars being 50 nm. Reproduced with permission from ref 41. Copyright 2007 American Chemical Society.

study identified several reaction parameters that needed to be optimized in generating the nanoframes, including the pH value of the reaction solution, the titration rate of $HAuCl_4$, and the concentration of the reducing agent. It was argued that the citrate used in the synthesis of Ag nanocrystals could remain on the {111} facets, leading to the selective deposition of Au atoms onto the edges and vertices of the nanocrystals for the formation of nanoframes. In another report, Ag triangular nanoprisms were employed as the template for the deposition of Au around the three edges (Figure 12A,E).[68] After the selective removal of Ag using a mixture of H_2O_2 and NH_4OH, triangular nanoframes were obtained. Taken together, these studies demonstrate that the same mechanism could be applied to the synthesis of both 3-D and 2-D nanoframes. It is worth acknowledging that the aforementioned nanoframes should be made of Au−Ag alloys rather than pure Au due to the easy interdiffusion and mixing between these two elements during the deposition and/or etching process.

In addition to Au, nanoframes based on other noble metals such as Ru, Rh, and Pt have also been reported in the literature by following a similar strategy that involved a combination of deposition and etching.[73−76] While most noble metals are typically deposited on templates with a matched fcc structure, Ru offers a particular challenge, because it assumes a hexagonal close-packing (hcp) structure in its bulk form. As such, a lattice mismatch tends to increase the interfacial energy and thus prevent the formation of a continuous Ru layer.[74,75] In one demonstration, it was shown that nanoframes made of fcc Ru−Pd alloy could be fabricated through a kinetically controlled, conformal deposition of Ru atoms on the vertices and edges of Pd-truncated octahedra, followed by a selective removal of the Pd core via Fe(III)-based wet etching.[74]

Built upon this success, a recent study explored the mechanistic details involved in the formation of fcc Ru−Pd nanoframes using a similar synthetic approach.[75] Figure 13A illustrates the proposed mechanism that combines an oxidative etching and galvanic replacement for the transformation of a Pd nanocube into a Pd@Ru core-frame cuboctahedron, followed by the conversion into a cuboctahedral nanoframe upon the removal of Pd core. In a typical synthesis, 10 nm Pd nanocubes were mixed with $Ru(acac)_3$, KBr, and PVP in triethylene glycol (TEG, a solvent and reducing agent) before the reaction progressed at 180 °C for 6 h. Next, the solid products were collected, washed, and redispersed in an aqueous solution of $FeCl_3$, PVP, KBr, and HCl for the selective removal of Pd. Figure 13B shows a TEM image of the nanoframes featuring ultrathin ridges. Figure 13C shows HAADF-STEM images captured from the nanoframes with different orientations relative to the electron beam. Because of the interdiffusion between Pd and Ru, the final product should be made of a Ru−Pd alloy dominated by Ru.

To understand the role of Br^- ions in the synthesis, a set of control experiments was performed. It was found that the Pd nanocubes became severely truncated when the concentration of KBr was increased. In contrast, when a low concentration of KBr was involved in the synthesis, the cubic shape of the Pd templates was preserved. These results confirmed that the Br^- ions and O_2 dissolved in the reaction solution could create an etchant for the oxidative etching of Pd, leading to truncation at the vertices of the Pd nanocubes. To support the argument that a galvanic replacement reaction contributes to the deposition of Ru on the vertices and edges of Pd cuboctahedra, the concentration of the Ru(III) precursor was varied. When less Ru(III) precursor was used compared to the case of a standard protocol, the Pd nanocubes underwent less truncation. In comparison, if the concentration of Ru(III) precursor was increased, the Pd nanocubes could no longer be preserved. It was argued that the Br^- ions would help facilitate the galvanic replacement between Pd atoms and Ru(III) precursor through the following reaction:

$$2Ru^{3+}_{(aq)} + 3Pd_{(s)} + 12Br^-_{(aq)} \rightarrow 2Ru_{(s)} + 3PdBr_4^{2-}{}_{(aq)} \quad (1)$$

Interestingly, the size of the Pd nanocubes also affected the outcome of a synthesis. When the size was reduced from 10 to 6 nm, cuboctahedral nanoframes were still obtained. However, when the size was increased to 18 nm, the Ru atoms were deposited in an island-growth manner, completely different from the conformal deposition observed in the standard protocol. Likely, the vertices on a larger Pd nanocube occupy a smaller area relative to the total surface area, making it possible to suppress the oxidative etching and the Br^--assisted galvanic reaction at these sites higher in surface energy. In this case, the Ru(III) precursor would be primarily reduced by TEG, rather than Pd, to form Ru atoms, followed by their deposition onto the Pd seeds. When the deposition rate was faster than that of surface diffusion, the Ru atoms would follow the island-growth mode.

https://dx.doi.org/10.1021/acs.chemrev.0c00940
Chem. Rev. 2021, 121, 796−833

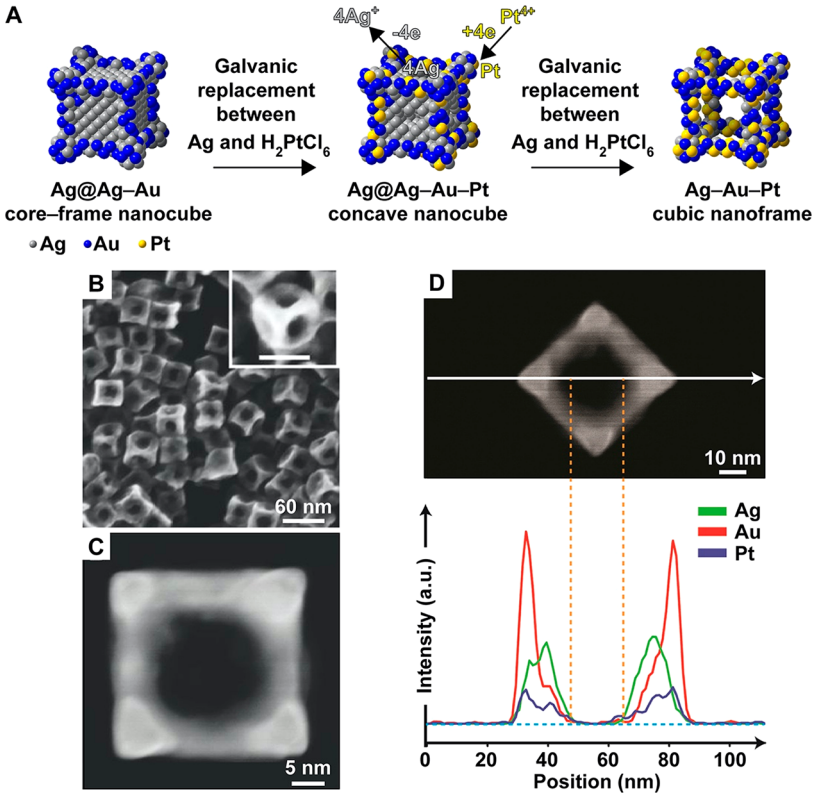

Figure 15. (A) Schematic illustration showing the formation of a Ag–Au–Pt cubic nanoframe via the galvanic replacement reaction between a Ag@Ag–Au core–frame nanocube and H_2PtCl_6. (B) SEM image of the resultant nanoframes and (C) HAADF-STEM image of an individual nanoframe. The scale bar in the inset of (B) is 40 nm. (D) HAADF-STEM image of the same nanoframe in (C) but with the raster angle rotated by 45° and the corresponding EDS line-scan profiles of Ag, Au, and Pt, respectively. Reproduced with permission from ref 79. Copyright 2019 American Chemical Society.

Dealloying of Hollow Nanocrystals. As discussed in Section 2.4 and Figure 6A, the first synthesis of bimetallic nanoframes was demonstrated using the galvanic replacement reaction between $AuCl_4^-$ and a sacrificial template based on Ag, together with the involvement of a dealloying process.[41] Figure 14A shows a schematic diagram to illustrate the transformation of a Ag nanocube into a Au–Ag cubic nanoframe through a two-step process that involves galvanic replacement and dealloying. In the first step, galvanic replacement was initiated by mixing 50 nm Ag nanocubes (Figure 14B) with aqueous $HAuCl_4$, leading to the production of one Au atom at the expense of three Ag atoms, which were oxidized into Ag^+ ions for their dissolution into the solution phase. The reaction can be described as follows.

$$3Ag_{(s)} + AuCl_4^-{}_{(aq)} \rightarrow Au_{(s)} + 3Ag^+{}_{(aq)} + 4Cl^-{}_{(aq)} \quad (2)$$

As the reaction proceeded, the Ag nanocubes were transformed into nanoboxes (Figure 14C), whose walls were composed of a Au–Ag alloy due to the interdiffusion between the two elements. In the second step, the nanoboxes were treated with a wet etchant such as aqueous $Fe(NO_3)_3$ or NH_4OH to selectively oxidize and dissolve Ag atoms but not Au atoms. As more Ag atoms were dissolved from the walls, the nanoboxes were transformed into nanocages decorated with pores (Figure 14D) and, finally, into cubic nanoframes mainly comprised of Au (Figure 14E). The ridge thickness of the resultant nanoframes could be reduced to ~5 nm when the amount of $HAuCl_4$ used in the galvanic step was controlled and with the selection of a proper etchant for the dealloying step.[41,42]

Galvanic Replacement. The galvanic replacement reaction between a metal template and a precursor to another metal can be directly employed to fabricate bi- and multimetallic nanoframes.[88] The success relies on tightly controlling the spatial confinement of the oxidation and reduction reactions to different sites on the surface of a template nanocrystal. In a recent study, we reported the production of Ag–Au–Pt trimetallic cubic nanoframes by leveraging the galvanic replacement reaction between Ag@Ag–Au core–frame nanocubes and H_2PtCl_6.[79] Figure 15A shows a schematic diagram of the synthesis. The template consists of a cubic Ag core with side faces framed by a Au–Ag alloy at the edges and vertices. As such, the Ag-dominated side faces are well-separated from the alloy regions located at edges and vertices. Because Ag is more prone to oxidation relative to the Ag–Au alloy, Ag atoms will be preferentially carved out from the faces upon the introduction of a precursor that can engage in a galvanic replacement reaction with Ag.

In a typical process, the Ag@Ag–Au core–frame nanocubes were prepared using a protocol that involved Ag nanocubes, ascorbic acid (a reducing agent), NaOH (a pH modifier), and cetyltrimethylammonium chloride (CTAC, a colloidal stabilizer) in an aqueous medium. The as-obtained particles were collected and then redispersed in an aqueous solution containing CTAC, followed by the dropwise titration of aqueous H_2PtCl_6. Initially, when Ag atoms were selectively oxidized from the center of each side face of the nanocube to form a cavity, the Pt(IV) precursor would be reduced to Pt atoms, followed by their deposition at edges and vertices for the generation of Ag@Ag–Au–Pt core–frame nanocubes. Because the Pt atoms could

https://dx.doi.org/10.1021/acs.chemrev.0c00940
Chem. Rev. 2021, 121, 796–833

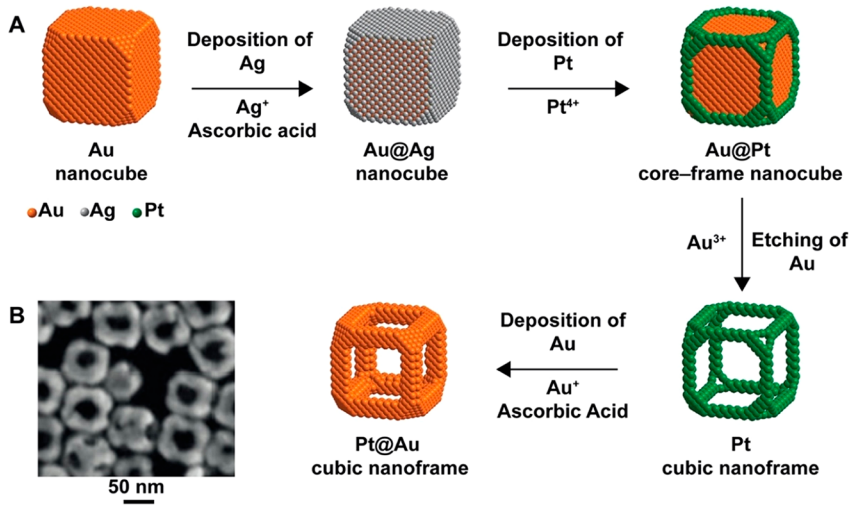

Figure 16. (A) Schematic illustration showing the transformation of a Au nanocube into a Au@Pt core–frame nanocube, and then a Pt cubic nanoframe after the removal of Au core, followed the deposition of Pt for the generation of a Pt@Au cubic nanoframe. (B) SEM image of the final product of Pt@Au nanoframes. Modified with permission from ref 82. Copyright 2015 Wiley-VCH Verlag GmbH & Co.

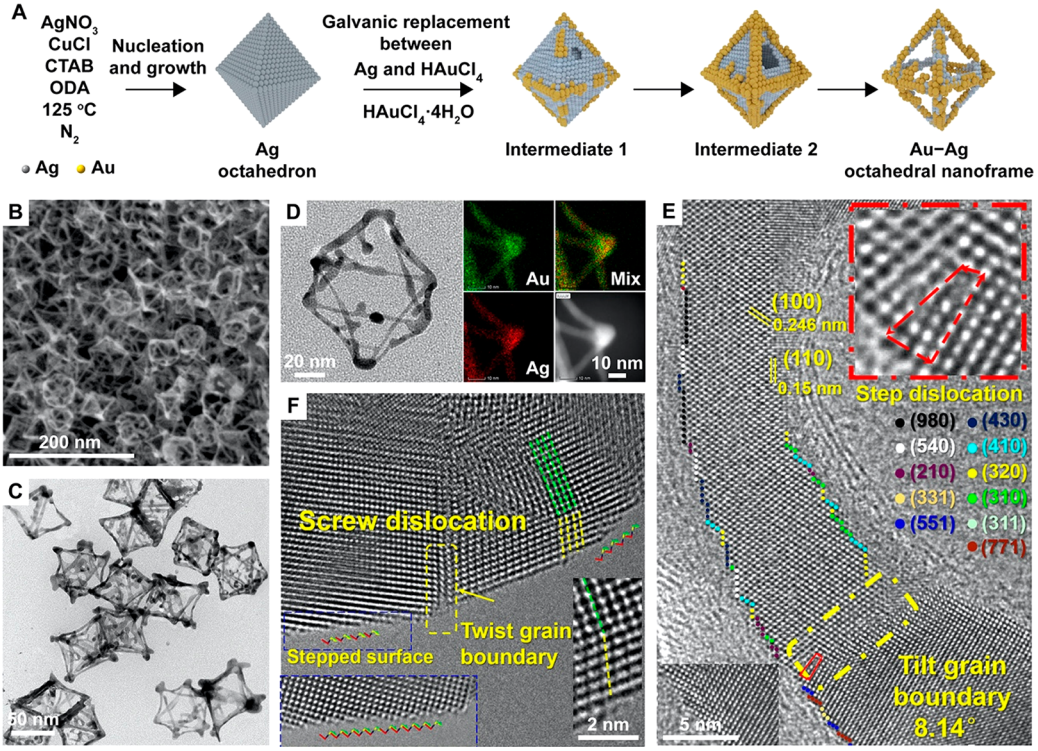

Figure 17. (A) Schematic illustration showing the formation of Au–Ag octahedral nanoframes via the galvanic replacement reaction between Ag octahedral nanocrystals and $HAuCl_4$ precursor in a one-pot synthesis. (B) SEM and (C) TEM images of Au–Ag octahedral nanoframes. (D) EDS elemental mapping of a Au–Ag octahedral nanoframe. (E) HRTEM image showing the atomic details on one of the edges, displaying an edge dislocation, high-index surface atoms, point defects, and tilt grain boundaries. (F) HRTEM image detailing one of the vertices, revealing stepped surface atoms, screw dislocations, and twist grain boundaries. Reproduced with permission from ref 34. Copyright 2019 Nature Publishing Group.

interdiffuse throughout the structure to form a thin trimetallic alloy at the sites surrounding, but not within, the cavity, the oxidation of Ag would be confined to the cavity at the center of each side face. As the reaction progressed, the cavities would grow in an orthogonal manner, intersecting each other at the center of the nanocube to eventually generate Ag–Au–Pt cubic nanoframes (Figure 15B,C). According to the EDS line-scan profiles of Ag, Au, and Pt (Figure 15D) for a cubic nanoframe, the center was devoid of any signal due to the hollow structure, while the region surrounding it consisted of all three elements. The deposition of the third metal via the galvanic reaction was proven to be crucial to the successful transformation of the template into the nanoframe structure by a control experiment, in which H_2PtCl_6 was replaced with $Fe(NO_3)_3$ as an etchant. Because Fe(III) was able to oxidize Ag without generating a metal atom in the process, it could not drill a hole through the center but rather delocalize oxidation over the entire surface of the template. This result confirmed that the creation of an alloy

https://dx.doi.org/10.1021/acs.chemrev.0c00940
Chem. Rev. 2021, 121, 796–833

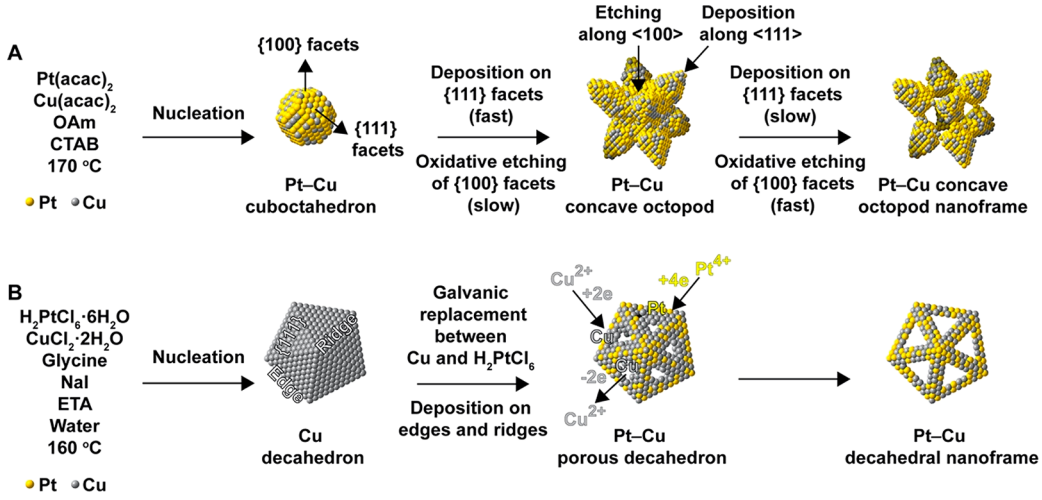

Figure 18. (A) Schematic illustration showing the formation of Pt−Cu concave octopod nanoframes using a one-pot synthesis. (B) Schematic illustration of the major steps involved in the formation of Pt−Cu fivefold-twinned decahedral nanoframes using a one-pot method. (A) Reproduced with permission from ref 35. Copyright 2017 American Chemical Society. (B) Reproduced with permission from ref 36. Copyright 2016 Wiley-VCH Verlag GmbH & Co.

region around the cavity helped confine the carving of Ag to the center of each side face.

By leveraging the stoichiometry and reduction potential of the precursor, we demonstrated that cubic nanoframes with different sizes and compositions could be obtained by simply replacing H_2PtCl_6 with another precursor such as K_2PtCl_4, Na_2PdCl_4, or $HAuCl_4$ in a standard protocol.[79] For example, when H_2PtCl_6 was replaced by K_2PtCl_4, Ag−Au−Pt nanoframes with smaller holes were obtained, because each Pt(II) could only oxidize two Ag atoms during the galvanic reaction. Interestingly, when Na_2PdCl_4 was used, the Ag−Au−Pd nanoframes with a large size for the holes were obtained owing to the increase in the extent of galvanic replacement. We could also use the same procedure to fabricate Ag−Au bimetallic nanoframes by switching to $HAuCl_4$. Collectively, our results demonstrated that the galvanic replacement reaction between Ag@Ag−Au nanocubes and a precursor could be employed to conveniently produce bi- and multimetallic nanoframes with different thicknesses for the ridges.

Nanoframe-Directed Deposition. Figure 16A shows an approach that utilizes the concept of nanoframe-directed deposition for the transformation of a Au nanocube into a Pt@Au nanoframe.[82] In the first step, a thin layer of Ag is coated on the surface of a Au nanocube, making it possible to deposit Pt on the edges and vertices through the galvanic replacement reaction between Ag and Pt(IV) precursor. In the second step, upon the introduction of Au(III) ions as an etchant, the inner Au core is selectively oxidized and then dissolved, in the form of Au(I) ions, into the reaction solution, leading to the formation of a Pt nanoframe. Finally, when a reducing agent is introduced, the Au(I) ions are reduced to generate Au atoms, followed by their redeposition onto the skeleton of the Pt nanoframe for the generation of a Pt@Au nanoframe. Figure 16B shows the scanning electron microscopy (SEM) image of the final product. A similar approach has also been demonstrated to transform Au nanoplates into Pt@Au nanorings. It has been argued that the use of a Pt nanoframe as a template for the deposition of Au could prevent the resultant nanostructure from deformation. Because these bimetallic nanoframes embrace both the plasmonic properties of Au and the catalytic properties of Pt, they represent a new class of materials for potential applications in sensing, catalysis, and biomedical research.[45,81,82]

One-Pot Synthesis. Most of the syntheses of bi- and multimetallic nanoframes discussed so far involve multiple, separate steps, making it difficult to scale them up for the production in large quantities. This problem can be addressed by switching to a one-pot synthesis, in which solid nanocrystals are formed and subsequently transformed into nanoframes in the same reaction container. In general, the ingredients for such a synthesis should include metal precursors, reducing agent(s), a colloidal stabilizer, a surface capping agent, coordination ligand(s), as well as a chemical etchant.[34−37,56,62,77]

In one demonstration, Au−Ag octahedral nanoframes rich in crystallographic defects were prepared in a one-pot synthesis by leveraging a galvanic replacement reaction.[34] Figure 17A shows a schematic illustration of the synthesis, where cetyltrimethylammonium bromide (CTAB, a structure-directing and a complexing agent) was dissolved in ODA (a solvent and a reducing agent) and kept under a N_2 environment at 125 °C for 1 h, and then $AgNO_3$ (a metal precursor) and CuCl (a coreducing agent) were added, followed by stirring for 36 min to generate Ag octahedral nanocrystals. Afterward, $HAuCl_4$ (a metal precursor) was rapidly injected to initiate a galvanic replacement reaction with the just-formed Ag octahedra, leading to the formation of Au−Ag octahedral nanoframes. In this process, the Br^- derived from CTAB and the Au(I) arising from the reduction of Au(III) would form a Au(I)−Br complex that has a lower redox potential, resulting in the controlled oxidation of Ag atoms by a slower galvanic replacement reaction. The Au atoms derived from the galvanic reaction would be initially deposited on the edges and vertices of the Ag octahedra due to the high reactivity of low-coordination atoms, while the capping of faces by ODA and CTAB would retard the deposition of Au. With enough Au atoms deposited at the edges and vertices, the underlying Ag atoms would be passivated against further oxidation, directing the galvanic reaction to the faces covered by {111} facets for the generation of cavities. While the Au would continue to grow at the edges and vertices, the released Ag(I) could remain in the solution by complexing with ODA and CTAB, further enlarging the cavities. At the same time, the high interdiffusion rate between Ag and Au atoms at the elevated

https://dx.doi.org/10.1021/acs.chemrev.0c00940
Chem. Rev. 2021, 121, 796−833

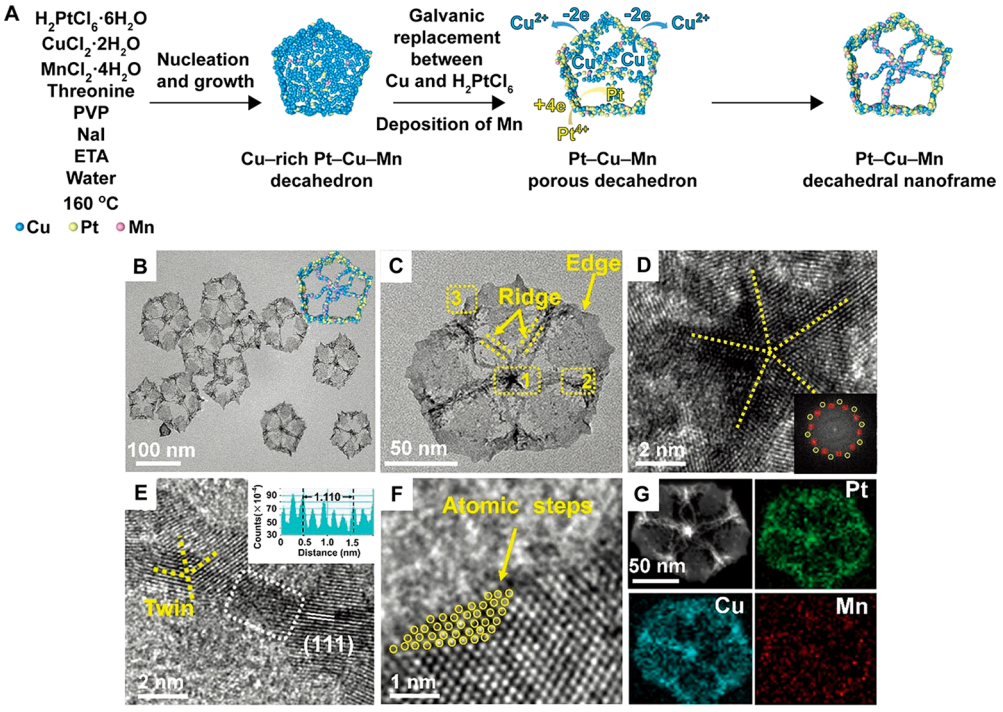

Figure 19. (A) Schematic illustration showing the formation of Pt−Cu−Mn decahedral nanoframes using a one-pot synthesis. (B, C) TEM images of the decahedral nanoframes. (D−F) HRTEM images taken from the yellow dotted squares 1, 2, and 3 in (C), respectively. (G) EDS elemental mapping of the decahedral nanoframes. Reproduced with permission from ref 37. Copyright 2020 Wiley-VCH Verlag GmbH & Co.

reaction temperature would promote the formation of a Au−Ag alloy at the edges and vertices of the nanocrystals. At the end, the Ag core could be fully removed by the galvanic reaction, leaving behind Au−Ag octahedral nanoframes.

Figure 17B−D shows SEM images, TEM images, and an elemental mapping, respectively, of the resultant Au−Ag octahedral nanoframes with the Au-to-Ag atomic ratio close to 3:1. High-resolution electron microscopy analyses revealed the lattice details of the Au−Ag octahedral nanoframes. Figure 17E shows a high-resolution TEM (HRTEM) image of the nanoframe viewed along the ⟨111⟩ zone axis, indicating that its surface was full of zigzag atomic steps, with the high-index facets denoted by different colors, as well as an edge dislocation with a tilt angle of 8.14° (inset). Additionally, a variety of other defects including a screw dislocation, a twist grain boundary, and stepped atoms were also observed, as shown in Figure 17F. To further support these findings, the samples were characterized by XRD, XPS, and X-ray absorption near-edge structure (XANES), respectively. It was found that the XRD peaks of the nanoframes were broadened as a function of the reaction time after adding $HAuCl_4$, suggesting a decrease in crystallinity for the nanoframe structure. Also, the XPS results showed an upshift for the Au 4f peaks, indicating the depletion of Au d-orbitals upon the formation of nanoframes. Finally, the XANES data showed that the coordination number of Au atoms in the nanoframes was decreased from 12 (bulk Au) to 9.4, and the bond length decreased slightly from 2.86 to 2.84 Å, suggesting a lattice contraction due to the presence of crystal defects.

Figure 18A shows the second example of a one-pot synthesis for the fabrication of $PtCu_2$ concave octopod nanoframes by balancing the rates of etching and growth.[35] In a typical synthesis, $Pt(acac)_2$ (a metal precursor) and $Cu(acac)_2$ (a metal precursor) powders were introduced into a mixture of OAm (a reducing agent) and CTAB (a colloidal stabilizer and the source of Br^-) in an autoclave reactor and then heated at 170 °C for 24 h. In the nucleation stage, when the O_2/Br^- etching pair was present in the reaction solution, Pt and Cu precursors were reduced by OAm for the formation of Pt−Cu cuboctahedral seeds enclosed by a mix of {111} and {100} facets, a thermodynamically favored shape. In the growth stage, Pt atoms derived from the reduction of $Pt(acac)_2$ were preferentially deposited on the {111} facets of Pt−Cu cuboctahedra due to the selective binding of Br^- to the {100} facets. When the rates of reduction and deposition were faster than those of etching and surface diffusion, the Pt−Cu cuboctahedra were transformed into concave nanocubes. As the Pt precursor in the reaction solution was gradually consumed over time, oxidative etching by Br^-/O_2 along {100} facets eventually prevailed over the deposition of Pt and Cu atoms on the {111} facets, leading to the transformation of solid nanocrystals into the concave octopod nanoframes.

Figure 18B shows a third example of a one-pot synthesis for the production of Pt−Cu fivefold-twinned decahedral nanoframes by coupling coreduction with a galvanic replacement reaction.[36] In a typical synthesis, $H_2PtCl_6·6H_2O$ (a metal precursor), $CuCl_2·2H_2O$ (a metal precursor), and ethanolamine (ETA, a reducing agent) were successively introduced into a solution containing glycine (a complexing agent), NaI (a complexing agent), and PVP (a colloidal stabilizer). The mixture was then loaded into an autoclave reactor and heated at 160 °C for 16 h. Because of the involvement of glycine in the reaction solution, the reduction rate of Cu(II) precursor by ETA was faster than that of the Pt(IV) species, leading to the formation of Cu decahedral nanocrystals. Next, the galvanic replacement reaction between Pt(IV) and Cu occurred on the {111} facets of the decahedral nanocrystals. Concurrently, the dissolved Cu(II) and the remaining Pt(IV) were coreduced by ETA for the production of Cu and Pt atoms, followed by their codeposition

https://dx.doi.org/10.1021/acs.chemrev.0c00940
Chem. Rev. 2021, 121, 796−833

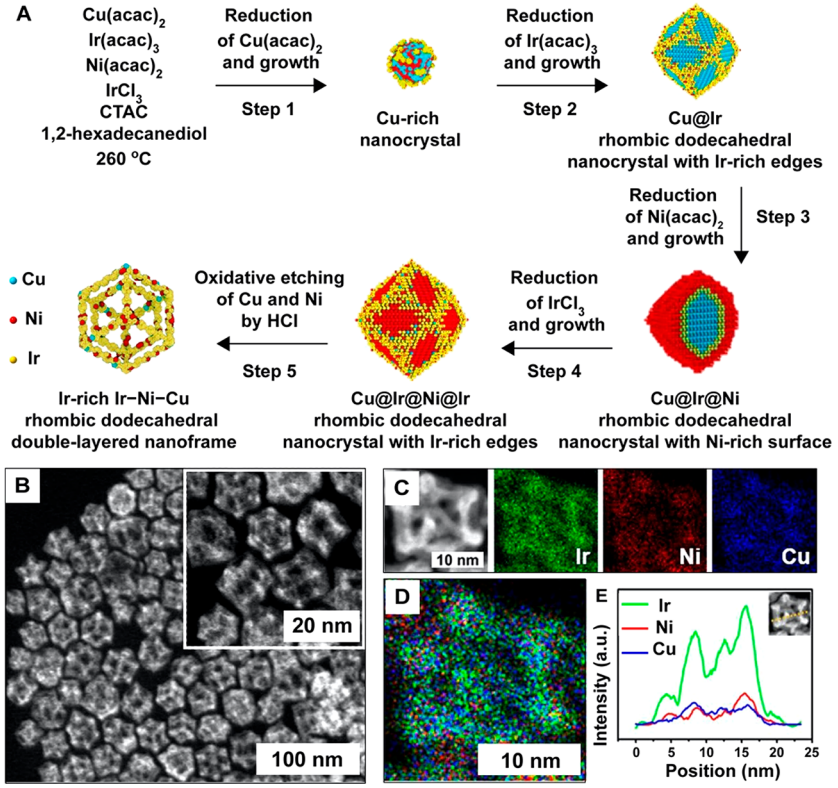

Figure 20. (A) Schematic illustration showing the one-pot synthesis of Cu@Ir@Ni@Ir triple-shelled nanocrystals with a rhombic dodecahedral morphology by leveraging the difference in kinetics for various precursors, followed by the formation of Ir−Ni−Cu double-layered nanoframes via the wet etching of Cu and Ni. (B) TEM image of final product. (C) HAADF-STEM image and the corresponding elemental mapping analysis of a double-layered nanoframe. (D) Elemental mapping analysis and (E) line profile data of a double-layered nanoframe. The colors in (D) correspond to Ir (green), Ni (red), and Cu (blue), respectively. Reproduced with permission from ref 44. Copyright 2017 American Chemical Society.

on the edges and ridges of the decahedral templates. Because the dissolution and deposition occurred on different sites, Pt−Cu decahedral nanoframes were obtained. There are also similar reports in the literature on the fabrication of Pt−Cu and Rh−Cu octahedral nanoframes, as well as Ir−Cu rhombic dodecahedral nanoframes.[56,62,77]

In addition to the fabrication of bimetallic nanoframes, the one-pot approach has also been successfully extended to the synthesis of trimetallic nanoframes. Figure 19A illustrates the formation of Pt−Cu−Mn decahedral nanoframes.[37] In a typical experiment, an aqueous solution containing PVP (a colloidal stabilizer), NaI (a complexing agent), and threonine (a reducing agent) was prepared, followed by the consecutive addition of H_2PtCl_6 (a metal precursor), $Cu(NO_3)_2$ (a metal precursor), $MnCl_2$ (a metal precursor), and ETA (a reducing agent) under stirring and sonication. The solution was then sealed in an autoclave reactor and heated at 160 °C. Samples were collected at different time points to monitor the reaction. At t = 8 h into the synthesis, Cu-rich decahedral nanocrystals were obtained, together with an atomic ratio of Pt/Cu/Mn = 13:85:3. This result suggested that the I^- ions strongly coordinated with Pt(IV) ions to decrease its reduction potential, allowing the reduction of Cu(II) to take place first and thus the formation of a Cu-rich decahedral nanocrystal. As the reaction time progressed to t = 12 h, the decahedral nanocrystals were gradually enlarged. The atomic ratio changed to Pt/Cu/Mn = 28:67:5, revealing that the content of Cu decreased while those of Pt and Mn were increased. Finally, at t = 16 h, well-defined decahedral nanoframes with very thin ridges were obtained. The atomic ratio was changed to Pt/Cu/Mn = 36:59:6, again indicating the relative increase in Pt and Mn over that of Cu. Taken together, it could be concluded that Cu-rich decahedral nanocrystals were first formed through the reduction of Cu(II) and thus nucleation and growth of Cu. Next, the galvanic replacement reaction between surface Cu atoms and the Pt(IV) precursor resulted in the formation of Pt atoms for their deposition at the high-energy sites such as ridges and edges of decahedra. Concurrently, the Mn(II) precursor would be reduced by the reducing agent to form Mn atoms for their deposition on the nanoframes throughout the synthesis, giving rise to its slight increase in content.

Figure 19B shows a TEM image of the Pt−Cu−Mn decahedral nanoframes with an average thickness of ∼1.8 nm for the ridges. Figure 19C,D shows the HRTEM image of one nanoframe and the corresponding fast Fourier transform pattern over the twin boundary region, respectively, both of which indicate the presence of a fivefold twin boundary at the vertex of the decahedral nanoframe. Also, the ridges of the nanoframe contained several twin boundaries (Figure 19E), while the edges possessed many atomic steps (Figure 19F), revealing the abundance of defect sites on the surface of the nanoframe. Moreover, EDS elemental mapping indicated the uniform distribution of Pt, Cu, and Mn across the Pt−Cu−Mn nanoframe (Figure 19G). To verify the presence of the compressive strain and evaluate its effects on the properties of the nanoframes, Pt−Cu−Mn pentagonal nanoframes with relatively less strain were prepared using the same protocol except for reducing the amount of threonine involved. Aberration-corrected scanning transmission electron microscopy (STEM) was then used to accurately measure the

https://dx.doi.org/10.1021/acs.chemrev.0c00940
Chem. Rev. 2021, 121, 796−833

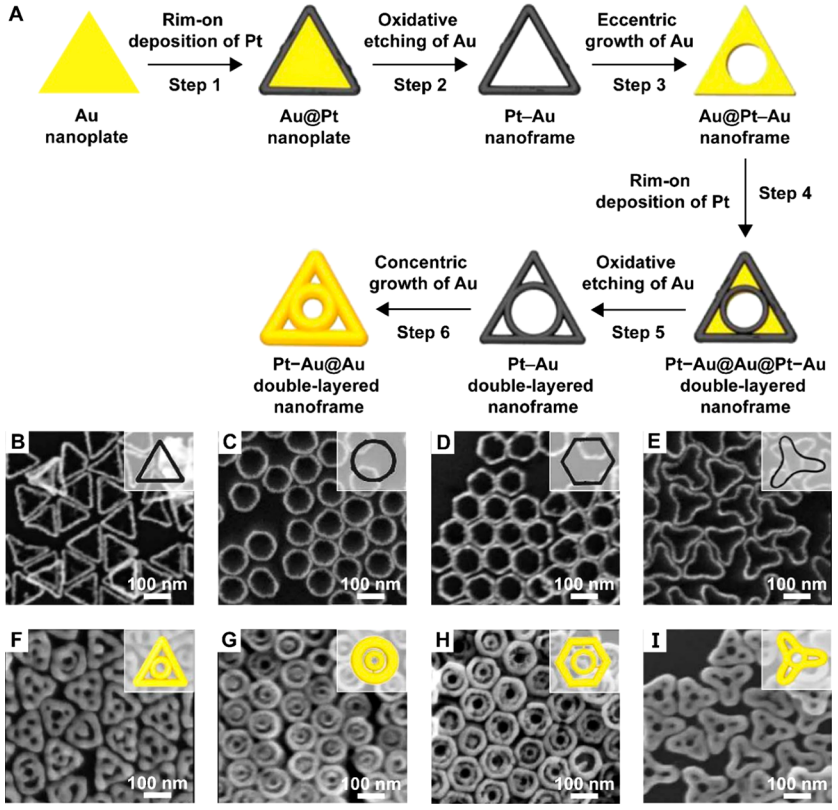

Figure 21. (A) Schematic illustration showing the formation of a Pt−Au@Au 2-D double-layered nanoframe from a Au nanoplate by controlling a series of heterogeneous growth and selective etching processes in a step-by-step manner. (B−E) SEM images of the resultant Pt−Au 2-D single-layered nanoframes with a variety of shapes after step 2: (B) triangle, (C) ring, (D) hexagon, and (E) tripod. (F−I) SEM images of the resultant 2-D double-layered Pt−Au@Au nanoframes with a variety of shapes after step 6: (F) triangle, (G) ring, (H) hexagon, and (I) tripod. The insets in (B−I) are the corresponding models. Reproduced with permission from ref 45. Copyright 2019 Nature Publishing Group.

interplanar spacing of (111) planes in the ridges of the two different samples of Pt−Cu−Mn nanoframes. The results indicated that the interplanar spacing in the ridge of decahedral nanoframes exhibited an obvious compression compared with that of pentagonal nanoframes, resulting in ∼1.5% compressive strain. Also, the XRD patterns recorded from the decahedral nanoframes, compared to that of pentagonal nanoframes, showed a positive shift that could also be attributed to the compressive strain. Geometric phase analysis revealed the formation of a distinct compression region on the decahedral nanoframes but not on the pentagonal nanoframes. Moreover, surface valence-band photoemission spectroscopy showed that the d-band center of the decahedral nanoframes was located at −2.32 eV, significantly downshifted from that (−2.04 eV) of the pentagonal nanoframes, which indicated the presence of compressive strain. Altogether, these analyses confirmed that the decahedral nanoframes had higher levels of compressive strain.

Although a one-pot synthesis greatly reduces the processing complexity for the fabrication of nanoframes in large quantities,[34−37,56,62,77] it remains challenging to perform rational syntheses of various nanoframes with good quality and high throughput. Part of the difficulty arises from the uncertainty in choosing suitable reagents for a specific synthesis to precisely control the nucleation, growth, and hollowing out processes of metal nanocrystals. In some cases, one reactant may play multiple roles in the synthesis. For example, halide ions (e.g., Cl^-, Br^-, and I^-) can serve as a coordination ligand to complex with the precursor ions. As such, they could make an impact on the reduction kinetics at the nucleation stage for controlling the internal structure of the seeds, including single-crystal, singly twinned, multiply twinned, and stacking-fault lined.[6,19] Furthermore, they can work as a capping agent for maneuvering the surface free energies of various types of facets on the seeds for directing their growth into nanocrystals with different shapes.[87] Finally, a combination of O_2/halide pair can also act as a powerful etchant to preferentially carve atoms from the faces of solid nanocrystals for their transformation into nanoframes.[20,88]

3.3. Nanoframes with Complex Morphologies and Nanoframe-Based Heterostructures

The discussion thus far was mostly restricted to the nanoframes that assume the contour of a simple polyhedron to help elucidate the design principles and mechanistic insights. Nevertheless, there are also major efforts in developing exotic nanoframe architectures and superstructures with advanced properties. These successes rely on creative engineering, together with process optimization, by following the aforementioned design principles.

Nanoframes with Complex Morphologies. In one case study, double-layered nanoframes (i.e., nanoframe@nanoframe) made of Ir, Ni, and Cu were produced using a one-pot synthesis.[44] When the difference in kinetics was leveraged among various precursors, Figure 20A shows a proposed pathway to synthesize Cu@Ir@Ni@Ir core−shell nanocrystals with a rhombic dodecahedral shape, followed by the transformation into Ir-rich Ir−Ni−Cu double-layered nanoframes via a wet etching of Ni and Cu. In a standard

https://dx.doi.org/10.1021/acs.chemrev.0c00940
Chem. Rev. 2021, 121, 796−833

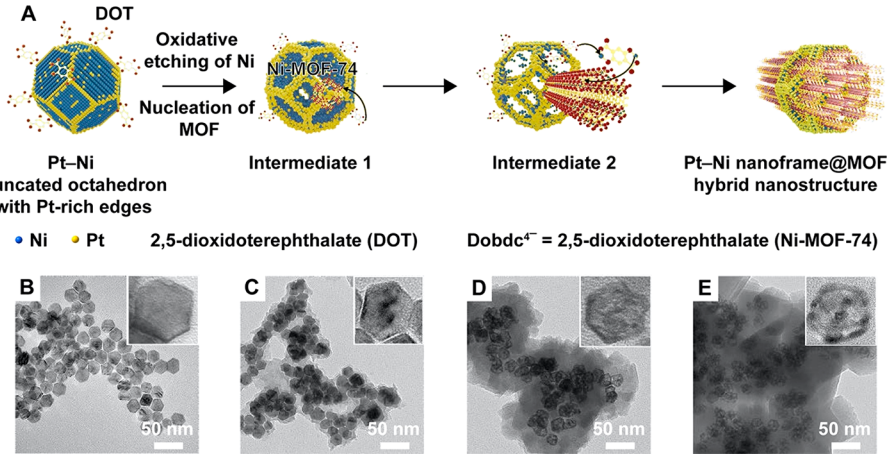

Figure 22. (A) Schematic illustration of the major steps involved in the formation of a Pt−Ni nanoframe@MOF hybrid nanostructure. (B−E) Representative TEM images of the (B) initial solid Pt−Ni truncated octahedral nanocrystals with Pt-rich edges at $t = 0$ h, (C) intermediate at $t = 0.5$ h, (D) intermediate at $t = 4$ h, and (E) the final Pt−Ni nanoframe@MOF hybrid nanostructures at $t = 12$ h, respectively. The scale bars in all insets are 10 nm. Reproduced with permission from ref 49. Copyright 2015 Nature Publishing Group.

protocol, a mixture of $Ir(acac)_3$, $IrCl_3$, $Ni(acac)_2$, $Cu(acac)_2$ CTAC, 1,2-hexadecanediol, and OAm was prepared and placed in a Schlenk tube under vacuum at 60 °C for 5 min and then heated to 260 °C. Initially, the $Cu(acac)_2$ precursor was first reduced to Cu atoms for their nucleation and growth, together with the deposition of small amounts of Ir and Ni, for the generation of a nanocrystal seed consisting of a Cu-rich core and IrNiCu alloy phase (step 1). Next, the seed evolved into a rhombic dodecahedral nanocrystal bearing Ir-rich edges due to the reduction of the $Ir(acac)_3$ precursor (step 2). As the reaction progressed, a larger rhombic dodecahedral nanocrystal with a Ni-rich layer on the surface was obtained owing to the reduction of $Ni(acac)_2$ and the accompanied growth (step 3). Finally, the unreacted $IrCl_3$ precursor was reduced to form Ir atoms for their growth on the Ni-rich surface, resulting in the formation of a Cu@Ir@Ni@Ir triple-shelled nanocrystal (step 4). After the removal of Cu and Ni by etching with HCl solution, a Ir−Ni−Cu double-layered nanoframe with an average composition of $Ir_{71}Ni_{24}Cu_5$ was formed (step 5). Figure 20B shows a TEM image of the final products, together with an elemental mapping analysis (Figure 20C,D). Note that the double-layered structures showed a slight difference between the compositions of the inner and outer nanoframes upon the removal of Ni and Cu, suggesting that interlayer diffusion might have taken place between the respective layers during the etching process.

In another case study, 2-D double-layered metal nanoframes were synthesized when a series of heterogeneous growth and selective etching processes were controlled in a step-by-step manner.[45] As one example, triangular Au nanoplates were transformed into double-layered nanoframes. Figure 21A shows a representative pathway that relies on rim-on deposition exclusively at the peripheries, selective etching (with the more reactive metal being removed by oxidation), eccentric growth (selective deposition at sites with the least lattice mismatch), and concentric growth (homogeneous deposition around the nanoframe). In step 1, the Au nanoplate seeds were initially mixed with CTAB, NaI, $AgNO_3$, and ascorbic acid in an aqueous solution to generate a thin layer of Ag at the high-energy vertices and edges of the Au nanoplates. Next, HCl and H_2PtCl_6 were added sequentially into the reaction solution for the generation of a layer of Pt at the vertices and edges of the Ag-coated Au nanoplates. It was argued that the Ag acted as a bridging layer to minimize the lattice mismatch between Au and Pt. In step 2, the as-obtained Au@Pt nanoplates were mixed with aqueous $HAuCl_4$ to initiate the etching process in the presence of CTAB and NaI, leading to the formation of Pt−Au nanoframes. Note that the EDS elemental analysis revealed some residual Au in the nanoframes, suggesting that Au and Pt formed an alloy at the interface. The oxidative etching between the Au atoms and $AuCl_4^-$ ions in the presence of excess Cl^- ions can be described as follows.

$$AuCl_4^-{}_{(aq)} + 2Au_{(s)} + 2Cl^-{}_{(aq)} \rightarrow 3AuCl_2^-{}_{(aq)} \quad (3)$$

In step 3, Pt−Au nanoframes were redispersed in an aqueous solution containing CTAB and NaI, followed by the sequential addition of $HAuCl_4$ and then ascorbic acid to generate Au@Pt−Au nanoframes through an eccentric growth. In steps 4 and 5, the Au@Pt−Au nanoframes were used as the templates to perform another round of rim-on deposition of Pt and selective etching of Au. Between these steps, the Au@Pt−Au nanoframes were transformed into Pt−Au@Au@Pt−Au nanoframes and then Pt−Au double-layered nanoframes. Finally, in step 6, the as-obtained Pt−Au double-layered nanoframes were added into an aqueous solution of CTAB and NaI, followed by the sequential addition of $AgNO_3$, $HAuCl_4$, and ascorbic acid, leading to the generation of Pt−Au@Au double-layered nanoframes via a concentric growth. Remarkably, these synthetic steps could be extended to the circular disks, hexagonal plates, or tripods for their transformation into the corresponding single- or double-layered nanoframes. Figure 21B−E,F−I shows, respectively, TEM images of the 2-D Pt−Au single-layered nanoframes and the Pt−Au@Au double-layered nanoframes with different shapes.

Heterostructured Nanoframes. Up to this point, we have focused on metal nanoframes with different compositions, structures, and morphologies. In recent years, there is a strong interest in integrating metal nanoframes with other functional materials for achieving high catalytic activity and/or selectivity.[46−49] To this end, several nanoframe@semiconductor hybrid nanostructures, such as Au@Cu_2O nanoframes, AgCl@Ag nanoframes, and Au-nanoprism/reduced graphene oxide/Pt-nanoframes, were successfully fabricated for photocatalytic applications, as discussed later in Section 4.3.[46−48] Additionally, Pt−Ni nanoframe@MOF (MOF = metal−organic framework)

https://dx.doi.org/10.1021/acs.chemrev.0c00940
Chem. Rev. 2021, 121, 796−833

hybrid nanostructures were recently prepared through in situ etching and growth.[49] Figure 22A shows a schematic diagram of this synthesis. In a standard protocol, $Pt(acac)_2$, $Ni(acac)_2$, PVP, and aniline were dissolved in benzyl alcohol, sealed in an autoclave reactor, and then allowed to react at 180 °C for 12 h to produce Pt−Ni truncated octahedral nanocrystals with Ni-rich faces and Pt-rich edges (Figure 22B). After they were washed, the nanocrystals were redispersed in DMF, followed by the addition of dihydroxyterephthalic acid, and the mixture was then sealed in another autoclave reactor. After reaction at 110 °C for another 12 h, Pt−Ni nanoframe@MOF hybrid nanostructures were obtained. Figure 22C shows the intermediate structure obtained at t = 0.5 h, indicating that a thin MOF shell with a weaker contrast had developed on the surface of the nanocrystals. At t = 4 h, the MOF shell grew into a much thicker layer, while the solid nanocrystal had evolved into a hollow structure, as shown in Figure 22D. Finally, at t = 12 h, Figure 22E confirms the formation of Pt−Ni nanoframe@MOF hybrid nanostructures. In this synthesis, the involvement of dihydroxyterephthalic acid, together with Ni^{2+}, led to the generation of a well-defined MOF of Ni_2dobdc (where $dobdc^{4-}$ refers to 2,5-dioxidoterephthalate), also known as Ni-MOF-74. The simultaneous etching of Ni and the growth of Ni-MOF-74 could be described as follows.

$$O_{2(g)} + 2H_2O_{(l)} + 4e^- \rightarrow 4OH^-_{(aq)} \quad (4)$$

$$2Ni_{(s)} \rightarrow 2Ni^{2+}_{(aq)} + 4e^- \quad (5)$$

$$2Ni^{2+}_{(aq)} + dobdc^{4-}_{(aq)} \rightarrow Ni_2dobdc_{(s)} \quad (6)$$

Eqs 4 and 5 were half reactions that together described the redox reaction between Ni and O_2, that is, $Ni + O_2 + 2H_2O \rightarrow 2Ni^{2+} + 4OH^-$, for carving Ni atoms from Pt−Ni truncated octahedra. Upon the removal of Ni atoms, the remaining Pt would be insufficient to form a shell on its own. On the one hand, it has been argued that the Pt atoms would segregate to the edges to form a nanoframe structure. On the other hand, the Ni^{2+} ions generated from oxidation could then be captured by the organic linker ($dobdc^{4-}$) in the vicinity to form the MOF in situ, as described by eq 6. Because the MOF would continue to precipitate out after consuming Ni^{2+} ions, the reaction equilibrium (eq 5) would shift toward the generation of more Ni^{2+}, accelerating the etching rate of Ni to promote the formation of Pt−Ni nanoframes. XRD patterns collected from the sample showed a set of peaks that were in agreement with previously published data on pure Ni-MOF-74, confirming its presence in the product. Additionally, the contrast in HAADF-STEM images, as well as the EDS elemental mapping images, showed Pt-rich nanoframes encapsulated by the Ni-dominated MOF, further supporting the formation of Pt−Ni nanoframe@MOF hybrid nanostructures. The unique frame-within-frame hybrid nanostructures could enhance the catalytic activity and selectivity toward the hydrogenation reaction owing to the synergistic effect between metal nanoframes and MOF, as discussed later in Section 4.2.2.

4. CATALYTIC APPLICATIONS

The open structure and high specific surface area intrinsic to nanoframes make them immediately useful in an array of catalytic applications. The catalytic performance of nanoframes can be further augmented by controlling their compositions and the spatial distributions of various elements (e.g., alloyed vs phase-segregated),[38,43] manipulating the crystal phase (e.g., fcc vs hcp),[74,75] engineering surface structure at the atomic scale (e.g., crystallographic defect, high-index facet, and strained lattice),[34−37] and/or integrating with other functional materials (e.g., nanoframe@MOF hybrid).[46−49] It is well-documented that metal nanoframes typically exhibit much better catalytic performance than their solid counterparts or other types of hollow nanocrystals, while helping minimize the use of rare, expensive precious metals. In this section, we provide both a technical discussion and an updated understanding of the structure−property relationship in the context of electrocatalysis, thermal catalysis, and photocatalysis, respectively.

4.1. Electrocatalysis

Electrocatalysis refers to the heterogeneous catalysis of a chemical reaction under the influence of an externally applied potential.[7,9,13,18,19,22,23,91−96] The catalytic material is typically deposited on the electrode to reduce the reaction overpotential by decreasing the activation energy barrier. At the current stage of development, most of the energy required for human activities comes from fossil fuels such as coal, oil, and natural gas, but none of these fuels seems to be sustainable. As such, energy production from renewable sources has been recognized as an important step toward the reduction of our future dependence on fossil fuels. For example, electrocatalytic water splitting for the direct production of hydrogen as a sustainable source for fuel cells offers an efficient and reliable platform for converting chemical energy to electricity with essentially zero emission.[91−94] In this section, we showcase recent progress in utilizing metal nanoframes as electrocatalysts toward reactions responsible for both fuel cells and water splitting.

4.1.1. Fuel Cells. Fuel cells are among the most promising energy solutions because of their high efficiency, zero carbon emission, quiet operation, and unlimited or renewable sources of the fuels.[91−94] For many decades, fuel cells have received great interest from both academia and industry, with a variety of target applications ranging from miniature power supplies to automobiles and large-scale heat and power plants. Fuel cells can be classified primarily according to the types of electrolytes involved, including proton-exchange membrane fuel cell (PEMFC), alkaline fuel cell (AFC), phosphoric acid fuel cell (PAFC), molten carbonate fuel cell (MCFC), and solid oxide fuel cell (SOFC). They all consist of a cathode, an anode, and an electrolyte that allows ions to move between the two electrodes. Among those, PEMFC utilizes a polymer electrolyte membrane (e.g., Nafion) to conduct protons for the ion-exchange purpose. It has attracted the most attention because of its low operating temperature, high power density, quick starting, and compact stack. In particular, PEMFC mainly consumes hydrogen, methanol, or formic acid as the fuel to produce electricity, with the byproducts including heat, H_2O, and CO_2 only. During the operation of a PEMFC, the fuel is oxidized at the anode to produce electrons and protons, while oxygen is reduced at the cathode.

Despite continued research and investment, most of the fuel cells based upon hydrogen, methanol, or formic acid have not yet made a broad impact on global power generation due to the combined issues related to performance, durability, and cost. One possibility to achieve the maximum performance and durability at a minimum cost is to design and fabricate the most efficient electrocatalysts. To this end, the platinum-group metals (PGMs, including Pt, Pd, Rh, Ru, and Ir) have been considered the prime choice of catalytic materials for the practical use of

https://dx.doi.org/10.1021/acs.chemrev.0c00940
Chem. Rev. 2021, 121, 796−833

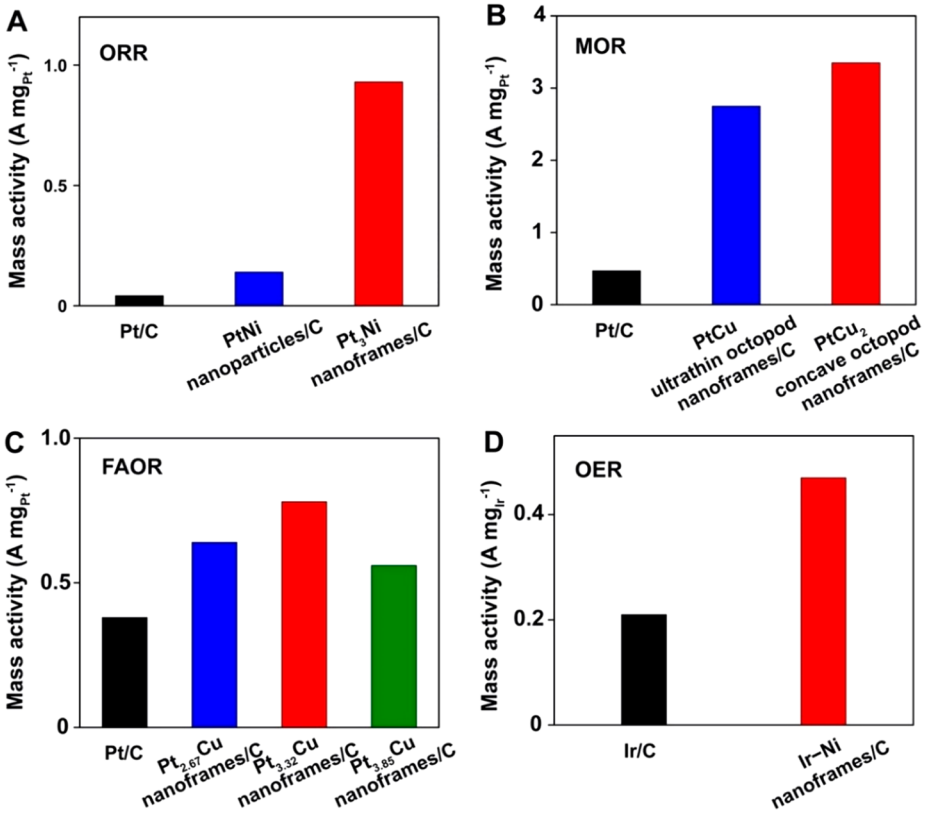

Figure 23. Applications of metal nanoframes in electrocatalysis. (A) Comparison of the mass activities of the commercial Pt/C and PtNi nanoparticles and Pt_3Ni nanoframes toward ORR. (B) Comparison of the mass activities of the commercial Pt/C, PtCu ultrathin octopod nanoframes, and $PtCu_2$ concave octopod nanoframes toward MOR. (C) Comparison of the mass activities of the commercial Pt/C, $Pt_{2.67}Cu$, $Pt_{3.32}Cu$, and $Pt_{3.85}Cu$ hierarchical trigonal bipyramid nanoframes toward FAOR. (D) Comparison of the mass activities of the commercial Ir/C and Ir–Ni nanoframes toward OER. (A) Reproduced with permission from ref 38. Copyright 2014 AAAS. (B) Reproduced with permission from ref 35. Copyright 2016 American Chemical Society. (C) Reproduced with permission from ref 110. Copyright 2015 Wiley-VCH Verlag GmbH & Co. (D) Reproduced with permission from ref 78. Copyright 2017 Elsevier.

PEMFCs on an industrial scale owing to their distinctive merits such as superb activity, high resistance to chemical attack, robust mechanical strength, and excellent high-temperature characteristics.[9,18,22,23] However, as limited by the mass activity and durability of the current Pt-based catalysts, for example, a large amount of this precious metal is required (~80 g) in order to achieve and maintain the power density needed for the operation of a midrange fuel cell vehicle.[22] Because PGMs are scarce in nature, any attempt to scale up the production of PEMFCs must minimize the loading of these elements. The U.S. DOE set a technical goal to research a mass activity of 0.44 A mg_{PGM}^{-1} at 0.9 V, with less than 40% loss in mass activity after 30 000 cycles, in using PEMFCs for transportation by the year of 2020. These technical targets have motivated scientists to develop more effective strategies for utilizing PGMs as cost-effective catalysts in PEMFCs. Driven by the multitude of advantages of metal nanoframes for catalysis, as presented in the previous sections, it is believed that one of the effective strategies for achieving the minimal use of these expensive metals while enhancing the catalytic properties of PGM-based catalysts for PEMFCs is to prepare them as nanoframes.

Oxygen Reduction Reaction. The working principle of PEMFC, with the use of hydrogen and oxygen gases to produce electricity, is illustrated by eqs 7–9.[9,18,23,91−94] At the anode of a PEMFC, a catalyst facilitates the hydrogen fuel to undertake an oxidation reaction (hydrogen oxidation reaction, HOR, eq 7) for the generation of protons and electrons. Through the electrolyte, the protons migrate from the anode to the cathode. Concurrently, electrons move from the anode to the cathode through an external circuit, producing the current output to drive an external device. At the cathode, another catalyst causes protons, electrons, and oxygen to react, generating water (ORR, eq 8). The overall reaction of PEMFC involving the use of hydrogen and oxygen is given in eq 9.

$$\text{anode reaction: } H_{2(g)} \rightarrow 2H^{+}_{(aq)} + 2e^{-} \quad (7)$$

$$\text{cathode reaction: } 1/2O_{2(g)} + 2H^{+}_{(aq)} + 2e^{-} \rightarrow H_2O_{(l)} \quad (8)$$

$$\text{overall reaction: } 1/2H_{2(g)} + O_{2(g)} \rightarrow H_2O_{(l)} \quad (9)$$

In general, the reaction rate of HOR on PGM-based catalysts is extremely fast. In comparison, the reaction rate of ORR on PGM-based catalysts is sluggish, which is ~5 orders of magnitude slower than that of HOR.[23] The slow ORR rate at the cathode restricts the overall performance of a PEMFC. To accelerate the ORR rate on the cathode, it is necessary to use a proper catalyst. Among PGMs, Pt is believed to be the best candidate as a catalytic material toward ORR. On the basis of theoretical calculations, a Pt catalyst has the optimum binding energy for O and OH intermediate species during ORR.[97,98] It is worth acknowledging that the catalysts should have moderate binding strength with the reaction intermediates, because either too strong or too weak binding will lead to difficulty in removing

https://dx.doi.org/10.1021/acs.chemrev.0c00940
Chem. Rev. 2021, 121, 796−833

the products or poor adsorption of the reactants, respectively. As a result, many research groups have focused on the optimization of Pt-based catalysts for accelerating ORR. In particular, because of the merits of nanoframes, many types of Pt-based nanoframes have been evaluated as catalysts for catalyzing ORR.

In one study, it was demonstrated that Pt cubic nanoframes could enhance both catalytic activity and durability toward ORR.[73] The Pt cubic nanoframes composed of ultrathin ridges ~2 nm in thickness were prepared through the edge-selected deposition of Pt on Pd nanocubes, followed by chemical etching of the Pd core. When benchmarked against the commercial Pt/C catalyst consisting of 2−3 nm Pt nanoparticles dispersed on a carbon support, the catalyst based on Pt cubic nanoframes exhibited both enhanced mass activity and durability toward ORR. It was found that the initial mass activity (at 0.9 V) of the Pt cubic nanoframes/C was 1.5 times higher than that of the commercial Pt/C catalyst (0.45 vs 0.30 A mg_{Pt}^{-1}). After 20 000 cycles of an accelerated durability test, the mass activity of the Pt nanoframes/C was sixfold higher than that of the commercial Pt/C catalyst. It was argued that the highly open structure composed of ultrathin ridges would contribute to the enhanced activity and durability of Pt cubic nanoframes by increasing the utilization efficiency of Pt atoms and preventing the aggregation on and detachment of nanoframes from the carbon support.

To further reduce the Pt loading and cost, a transition metal such as Ni, Co, Fe, or Cu was often introduced into the Pt lattice to change the composition into an alloy for enhancing the catalytic performance toward ORR.[36−38,43,50,51,57−60] The transition metal could modulate the electronic structure (the so-called d-band center) via ligand and strain effects.[22,97,98] On the one hand, the ligand effect is a result of the difference in electronegativity between two dissimilar atoms and thus electron transfer between them. On the other hand, the strain effect is caused by the strain field arising from the mismatch in lattice constant between two dissimilar metals. Both effects can help generate a favorable surface for the O_2 dissociation, as well as the removal of O and OH intermediate species, enhancing the activity of Pt-based alloy catalysts toward ORR. In addition to the direct mixing of two metals to form a Pt-based alloy, the ability to maneuver the spatial arrangement of components in the near-surface region could further enhance both the activity and durability. For example, the formation of a phase-segregated Pt skin over a bulk single-crystal alloy with the Pt_3Ni composition (a uniform layer of Pt atoms on top of a layer containing Ni atoms) could weaken the interaction between the Pt surface atoms and nonreactive oxygenated species (i.e., OH) and, ultimately, increase the number of active sites for O_2 adsorption.[99]

In one case study, Pt_3Ni rhombic dodecahedral nanoframes with a Pt skin were prepared by a face-selected carving of $PtNi_3$ solid rhombic dodecahedral nanocrystals (Figure 10).[38] The interior and exterior surfaces of this highly open structure were composed of 24 ultrathin ridges (~2 nm) with a phase-segregated Pt skin on the surface. Because of the change in electronic structure of the outermost Pt atoms by subsurface Ni, the Pt-based surface could reduce the coverage of oxygenated intermediate species (i.e., OH) to achieve an excellent activity and durability.[99] As shown in Figure 23A, compared to the commercial Pt/C and solid PtNi catalysts, the Pt_3Ni rhombic dodecahedral nanoframes with a Pt skin showed substantially higher activity, with a mass activity of ~0.97 A mg_{Pt}^{-1} at 0.95 V. In addition to the high mass activity, the Pt_3Ni nanoframes offered remarkable durability, showing negligible activity loss after 10 000 potential cycles between 0.6 and 1.0 V. In comparison, the commercial Pt/C catalysts lost ~40% of the specific surface area, giving poor durability after the same number of cycles due to the dissolution and agglomeration of the Pt nanoparticles. Phase-segregated Pt−Ni octahedral nanocrystals/nanoframes (Figure 11),[43] rhombic dodecahedral nanoframes,[58] and tetrahexahedral nanoframes[59,60] have also been fabricated to achieve greatly improved ORR performance relative to the commercial Pt/C catalyst. These results suggest that it is an effective strategy to enhance the ORR activity and durability of Pt-based catalysts through the fabrication of nanoframes made of a Pt-based alloy with controls in the spatial distributions of the different elements.

In another case study, it was found that the introduction of a new element into a Pt lattice could change the local atomic spacing due to the lattice mismatch and thus the strain effect.[100−103] Such induced compressive or tensile strain could be used to tune the catalytic activity. For example, it was demonstrated that the ORR activity of Pt nanoparticles increased by 90% when the Pt surface was compressed by ~5%, but it decreased by 40% when the surface was extended by ~5%.[100] On the one hand, for Pt-based catalysts with a moderate compressive strain, the activity enhancement can be attributed to the optimization of binding strength with the reaction intermediates of ORR based on the theoretical study.[100−103] On the other hand, for the Pt-based catalysts with a tensile strain, the higher tensile strain would lead to stronger surface binding for the reaction intermediates with Pt because of the upshift of the d-band center, thereby decreasing the overall ORR rate.

In addition to doping, it is well-known that the ultrathin structure in metal nanocrystals could also facilitate the generation of compressive strain. For example, two samples of twinned Pt−Cu−Mn decahedral nanoframes covered by high-density step atoms but with different lattice strains were prepared through a galvanic replacement approach.[37] Interestingly, the ultrafine Pt−Cu−Mn nanoframes (Figure 19) showed superior activity in an alkaline environment toward ORR, because of its ~1.5% compressive strain relative to the pentagonal Pt−Cu−Mn nanoframes. DFT calculations suggested that the ultrafine Pt−Cu−Mn nanoframes under the compressive strain led to weaker binding strengths and adsorption of oxygen-containing intermediates, which could smooth the ORR reaction path, reduce the overpotential, and enhance the ORR catalytic activity. This study confirms that strain-controlled nanoframe catalysts could be fabricated to increase the efficiency of ORR. It is worth mentioning that the decahedral and icosahedral nanocrystals are typical fivefold twinned nanocrystals containing 10 and 30 twin boundaries, respectively.[19] The significant surface strain associated with twin boundaries and side faces has also been found to be instrumental to enhancing the catalytic activity in many studies, because they alter the electronic structures of surface atoms by shifting the d-band center.[103,104]

In summary, Pt-based catalysts are the most extensively studied and promising catalysts for accelerating the sluggish ORR kinetics in PEMFC. By switching from solid nanocrystals to nanoframes consisting of ridges of only a few nanometers thick, one can improve the mass activity toward ORR owing to the high utilization efficiency of atoms and the high density of catalytically active sites on the surface. By combining Pt with other transition metals and then controlling their spatial distributions, the ORR activity of Pt-based nanoframes could be further enhanced through a modification of electronic

https://dx.doi.org/10.1021/acs.chemrev.0c00940
Chem. Rev. 2021, 121, 796−833

structure via ligand and strain effects. Furthermore, by shrinking the ridge thickness of Pt-based nanoframes and/or incorporating twin boundaries to induce strain effect, the efficiency of ORR can also be improved significantly.

Methanol Oxidation Reaction. Direct-methanol fuel cell (DMFC) is a subclass of PEMFC, in which an aqueous solution of methanol is supplied as the fuel instead of hydrogen gas.[105−107] Its main advantages include the high energy density, good electrochemical activity, relatively low price, and ease of storage and transportation of methanol. For DMFC, methanol is oxidized on the anode to generate CO_2 through methanol oxidation reaction (MOR, eq 10). The protons migrate across the proton exchange membrane (usually Nafion) to the cathode and react with oxygen on a catalyst to produce water (eq 11). At the same time, a current is formed by electron transportation from the anode to the cathode through an external circuit. The overall reaction in DMFC is given by eq 12.

anode reaction:

$$CH_3OH_{(l)} + H_2O_{(l)} \rightarrow CO_{2(g)} + 6H^+_{(aq)} + 6e^- \quad (10)$$

cathode reaction:

$$3/2O_{2(g)} + 6H^+_{(aq)} + 6e^- \rightarrow 3H_2O_{(l)} \quad (11)$$

overall reaction:

$$CH_3OH_{(l)} + 3/2O_{2(g)} \rightarrow CO_{2(g)} + 2H_2O_{(l)} \quad (12)$$

Again, Pt-based catalysts are regarded as the best candidate for accelerating the MOR on the anode, which can break the C−H bond and facilitate the oxidation of methanol.[34−36,63,107] During MOR, however, the Pt surface is easily poisoned by the reaction intermediates such as CO. In this case, the strong adsorption of CO can reduce the number of available active sites, resulting in low performance toward DMFC. To this end, many efforts have been made to improve the tolerance of Pt to CO. One effective strategy involves the modification of Pt with a second metal that supplies oxygen species to react with the neighboring Pt−CO for the formation of CO_2. Additionally, the Pt electronic structure could be altered by the metals added for weakening the Pt−CO bond. For example, various Pt−Cu solid and hollow nanocrystals with different morphologies (e.g., cube, octahedron, hexapod, dendrite, tube, and cage) exhibited better electrocatalytic activity toward MOR than the commercial Pt/C catalyst.[107] In addition to their unique structural advantages, the CO-induced poisoning effect became much weaker after alloying Pt with Cu relative to that on pure Pt, helping increase the efficiency and durability of Pt-based catalysts.

In a recent study, both $PtCu_2$ concave octopod nanoframes and PtCu ultrathin octopod nanoframes were synthesized (Figure 18A) for comparison as catalysts toward MOR.[35] It was found that $PtCu_2$ concave octopod nanoframes exhibited a mass activity (3.36 A mg_{Pt}^{-1}) that was 1.2 and 7.0 times higher than that of the PtCu ultrathin octopod nanoframes and commercial Pt/C, respectively (Figure 23B). Additionally, in comparison with the commercial Pt/C, the onset potentials for CO-stripping cyclic voltammetry on these two types of Pt−Cu nanoframes were both negatively shifted, indicating their enhanced antipoisoning ability toward CO. After the durability test that involved 2000 cycles of sweeping from −0.2 to 1.0 V, both the catalytic activity and the structure of $PtCu_2$ concave octopod nanoframes were well-preserved, while some edges of the PtCu ultrathin octopod nanoframes suffered from fragmentation, leading to collapse and reduced activity. Taken together, the $PtCu_2$ concave octopod nanoframes promise an excellent choice of catalyst toward MOR. It is worth acknowledging that several other Pt-based alloy nanoframes, such as Pt−Cu decahedral nanoframes[36] and Pt−Cu−Co rhombic dodecahedral nanoframes,[63] were also investigated. They had mass activities of 2.26 and 4.11 A mg_{Pt}^{-1}, respectively, and both values were higher than that of the commercial Pt/C catalyst.

Formic Acid Oxidation Reaction. Direct-formic acid fuel cell (DFAFC) is also a subclass of PEMFC, where the liquid fuel, formic acid, is fed directly to the anode.[108,109] For DFAFC, the anode reaction is the electrocatalytic oxidation of formic acid into CO_2 on a catalyst (formic acid oxidation reaction, FAOR, eq 13). The protons are passed through the polymer membrane to react with oxygen on a catalyst located at the cathode to produce water (eq 14). Electrons are transported through an external circuit from the anode to cathode, providing electricity to an external device. The net reaction of DFAFC is represented in eq 15.

anode reaction:

$$HCOOH_{(l)} \rightarrow CO_{2(g)} + 2H^+_{(aq)} + 2e^- \quad (13)$$

cathode reaction:

$$1/2O_{2(g)} + 2H^+_{(aq)} + 2e^- \rightarrow H_2O_{(l)} \quad (14)$$

overall reaction:

$$HCOOH_{(l)} + 1/2O_{2(g)} \rightarrow CO_{2(g)} + H_2O_{(l)} \quad (15)$$

The electrocatalysis of FAOR has been intensively studied on various metals and alloys. Among them, Pt- and Pd-based catalysts are the most effective and commonly used anode catalysts in DFAFC.[55,56,60,110,111] In the case of a Pt-based system, the catalysts are usually deactivated by the reaction intermediates such as CO during the FAOR, showing poor durability. To address this problem, the catalysts have been modified by incorporating other metals to form binary or ternary alloys. In one study, the Pt−Cu trigonal bipyramid nanoframes were demonstrated with high mass activity and durability for FAOR compared to the commercial Pt/C catalyst, as shown in Figure 23C.[110] Significantly, the current density of the Pt−Cu trigonal bipyramid nanoframes with an intermediate Pt-to-Cu molar ratio of 3.32 was ∼2.1 times higher than that of the commercial Pt/C catalyst (0.78 vs 0.38 mA mg_{Pt}^{-1}). Additionally, after 1000 cycles of a durability test, the mass activity was only reduced by 11.6% for the Pt−Cu trigonal bipyramid nanoframes but by 36.4% for the commercial Pt/C catalyst. In other studies, Pt−Cu octahedral,[56] Pt−Ni tetrahexahedral,[60] and Pt−Pd−Rh−Ag octahedral nanoframes[111] were also found to exhibit significantly enhanced catalytic activity and durability toward FAOR in comparison with the commercial Pt/C catalyst and even their solid counterparts. Collectively, these results suggest that the excellent catalytic performance toward FAOR could be largely attributed to both the structural and electronic effects of the Pt-based alloy nanoframes.

In addition to Pt-based catalysts, Pd is also widely used as a catalytic material for application in DFAFC because of its high activity toward FAOR. Recently, nanoframes made of pure Pd were synthesized by directly etching solid nanocrystals with different shapes through the manipulation of the oxidative etching and regrowth rates (Figure 9).[55] These Pd octahedral nanoframes exhibited nearly 7.5 times higher catalytic activity than that of the Pd octahedral nanocrystals toward FAOR, which was attributed to the large specific surface area, as well as the large fraction of corner and edge atoms. After 1000 cycles of the

https://dx.doi.org/10.1021/acs.chemrev.0c00940
Chem. Rev. 2021, 121, 796−833

durability test, the structure of the octahedral nanoframes was well-maintained, and they still exhibited an activity 6.5 times higher than that of the solid counterpart, demonstrating the excellent durability of nanoframes during FAOR.

4.1.2. Water Splitting. Electrocatalytic water splitting is the process that relies on the use of electricity to split water into hydrogen and oxygen gases on the catalyst-decorated electrodes.[112−114] It is an ideal solution for generating clean energy and underpinning the hydrogen economy. Because the electric conductivity of pure water is pretty low, water splitting is typically performed under acidic or alkaline conditions. In an acidic environment, protons carry the current through an electrolyte for supporting the oxygen evolution reaction (OER, eq 16) and hydrogen evolution reaction (HER, eq 17) on the anode and cathode, respectively. On the one hand, eq 18 is the overall reaction of water splitting. On the other hand, the half-cell reactions for the anodic OER and cathodic HER in an alkaline medium can be described by eqs 19 and 20, respectively. The net reaction is presented in eq 21. In general, compared to the acidic water splitting, alkaline water splitting has been studied more extensively, because metal-based catalysts are passivated to avoid corrosion in alkaline media. However, because of the sluggish kinetics of water reduction and oxidation, it is crucial to develop efficient HER and OER electrocatalysts in both acidic and alkaline media. To this regard, catalysts based on metal nanoframes provide a strong candidate.

anode reaction in acidic media:

$$H_2O_{(l)} \rightarrow 1/2O_{2(g)} + 2H^+_{(aq)} + 2e^- \quad (16)$$

cathode reaction in acidic media:

$$2H^+_{(aq)} + 2e^- \rightarrow H_{2(g)} \quad (17)$$

overall reaction in acidic media:

$$H_2O_{(l)} \rightarrow H_{2(g)} + 1/2O_{2(g)} \quad (18)$$

anode reaction in alkaline media:

$$2OH^-_{(aq)} \rightarrow H_2O_{(l)} + 1/2O_{2(g)} + 2e^- \quad (19)$$

cathode reaction in alkaline media:

$$2H_2O_{(l)} + 2e^- \rightarrow H_{2(g)} + 2OH^-_{(aq)} \quad (20)$$

overall reaction in alkaline media:

$$H_2O_{(l)} \rightarrow H_{2(g)} + 1/2O_{2(g)} \quad (21)$$

Oxygen Evolution Reaction. In this process, as shown in eqs 16 and 19, molecular oxygen is produced via several proton- and electron-coupled steps, and the reaction is highly pH-dependent. Under an acidic condition, two water molecules are oxidized to produce one oxygen molecule and four protons. In comparison, in an alkaline environment, hydroxide is transformed into water and oxygen through oxidation. Ideally, the OER catalyst should have a high activity to overcome the energy barrier. The desired catalyst should also embrace low overpotential and high durability. As discussed in the next section, Pt-based catalysts are nearly ideal for the HER at cathode and the OER at anode. However, it has been argued that Pt nanocrystals could form a poorly conducting oxide phase on their surface for their potential dissolution into the reaction solution as ionic complexes, resulting in high overpotential and poor durability.[23,112−114] In comparison, Ir- and Ru-based catalysts and their corresponding oxides during OER can serve as efficient and stable catalysts toward OER in water electrolyzers.[62,78]

On the basis of theoretical studies, when Ir is alloyed with a transition metal, the stable binding of oxygen on pure Ir becomes weaker, contributing to an enhanced OER activity. In one study, it was demonstrated that the Ir−Ni rhombic dodecahedral nanoframes exhibited a superior electrocatalytic performance toward OER in acidic media, as shown in Figure 23D.[78] Specifically, the electrochemical performance of Ir−Ni nanoframes and a commercial Ir/C catalyst was examined in 0.1 M $HClO_4$. Their mass activities were calculated to be 0.47 and 0.21 A mg_{Ir}^{-1}, respectively, indicating that the Ir−Ni nanoframes were much more competitive catalysts than the commercial Ir/C. Remarkably, after 5000 potential cycles of OER, the performance of the Ir−Ni nanoframes was largely retained, while that of Ir/C was deteriorated significantly. On the one hand, the XPS data suggested that the enhanced catalytic activity and durability could be attributed to the presence of IrO_x on the surface of Ir−Ni nanoframes, in addition to the advantages of active grain boundaries and agglomeration-free feature. On the other hand, other Ir-based catalysts toward OER were recently demonstrated, including the Ir−Ni−Cu single- and double-layered nanoframes (Figure 20).[44]

Interestingly, Rh-based nanocrystals are also excellent catalysts toward OER. In one study, the Rh−Cu truncated octahedral nanoframes were fabricated and demonstrated as highly efficient OER catalysts in an alkaline medium (i.e., 0.10 M NaOH solution).[62] It was found that the mass activity of Rh−Cu truncated octahedral nanoframes was approximately twice that of irregularly shaped Rh nanoparticles. The nanoframes also showed high durability throughout the electrochemical operation, with preserved structure of nanoframes after a long-term durability test. On the basis of the XPS results, it was argued that the formation of a large proportion of oxidized Rh atoms (63.2%) on the Rh−Cu truncated octahedral nanoframes could account for the enhanced OER performance.

Hydrogen Evolution Reaction. In the electrocatalytic water splitting, the activity of HER in an alkaline medium is typically 2−3 orders of magnitude lower than that in an acidic medium.[23,112−114] As a result, the development of effective catalysts toward HER is extremely challenging, especially for use in an alkaline environment. It involves the dissociation reaction of HO−H, followed by the generation of H_2 through the recombination of two adsorbed hydrogens. In addition to breaking the strong covalent HO−H bond, stronger H binding is also responsible for the slow HER rate in an alkaline solution. Ideally, the rational design of catalysts with abilities to dissociate water and promote hydrogen recombination can effectively improve the HER performance in an alkaline system. Among various catalysts, those based on Pt nanocrystals with different morphologies have shown promising activity and durability toward HER.[114] However, only a few of these studies deal with the use of Pt-based nanoframes.[38,64]

In one study, the Pt_3Ni rhombic dodecahedral nanoframes with a Pt skin exhibited substantially enhanced activity toward HER in an alkaline electrolyte (i.e., 0.1 M KOH solution) compared to the commercial Pt/C catalyst.[38] In another study, the Pt−Ni−Co ternary alloy nanoframes showed HER activity superior to the Pt−Ni binary alloy nanoframes and the commercial Pt/C catalyst in 0.1 M KOH solution.[64] It was speculated that the addition of Co atoms into the Pt−Ni nanoframes could enhance the oxidation of Ni species and

https://dx.doi.org/10.1021/acs.chemrev.0c00940
Chem. Rev. 2021, 121, 796−833

thereby facilitate the cleavage reaction of HO−H. Likely, the synergistic effect of Ni and Co could tune the surface formation energy of Pt−OH and thus promote the overall reaction activity toward alkaline HER. After 5000 scanning cycles between −0.3 and 0.1 V, it was found that the Pt−Ni−Co nanoframes exhibited remarkable long-term durability, while the morphology was well-preserved.

4.2. Thermal Catalysis

In this section, we include the recent progress in using metal nanoframes for the conventional thermal catalysis. We focus on a few reports on the use of metal nanoframes as catalysts to accelerate the kinetics of dehydrogenation and hydrogenation reactions.[49,61,71,74,75,83] Because of the unique and promising advantages of diverse metal nanoframes and their derivatives with different functionalities, there is a lot of room for further development by leveraging the structural merits of nanoframes to optimize the catalytic activity and/or selectivity.

4.2.1. Dehydrogenation. The catalytic, selective dehydrogenation of liquid hydrazine (N_2H_4) or solid ammonia borane ($H_3N{-}BH_3$) offers an effective method for generating hydrogen gas that can be used for fuel cells because of their high hydrogen content.[74,75,115] During the decomposition of N_2H_4 and $H_3N{-}BH_3$, there is no formation of CO_2 due to the absence of carbon atoms in these compounds. As such, there is no production of species such as CO, a product of incomplete oxidation of carbon-containing molecules, that may poison the catalysts and thus lead to poor durability. However, both N_2H_4 and $H_3N{-}BH_3$ are highly toxic compounds, which should be taken into account to prevent any contact. It has been documented in the literature that Ru- and Rh-based nanocrystals were attractive catalytic materials toward the production of hydrogen from these hydrogen storage materials.[61,74,75]

In one report, the catalytic activity and selectivity of fcc-Ru cuboctahedral nanoframes (Figure 13) toward hydrazine decomposition were investigated by benchmarking against those of solid nanoparticles made of hcp- and fcc-Ru.[75] At room temperature, hydrazine decomposition can proceed through incomplete ($3N_2H_4 \rightarrow 4NH_3 + N_2$) and complete ($N_2H_4 \rightarrow N_2 + 2H_2$) routes. Among the three catalysts tested, Figure 24A shows that the fcc-Ru nanoframes exhibited the best catalytic performance, giving an $n(H_2 + N_2)/nN_2H_4$ ratio of 1.5, 3.0, and 2.1 times as great as that of hcp- and fcc-Ru nanoparticles with average sizes of 3.1 and 3.3 nm in diameter, respectively. Remarkably, the fcc-Ru nanoframes also exhibited substantially enhanced H_2 selectivity (43.9%) for hydrazine decomposition compared to the hcp- (7.8%) and fcc- (13.7%) Ru nanoparticles. This result was consistent with a DFT prediction that the fcc phase of Ru is more active toward N−N bond breaking, leading to favorable complete hydrazine decomposition relative to the hcp phase of Ru. After 10 cycles of repeated catalytic measurements, the H_2 selectivity of fcc-Ru nanoframes remained superior, 3.4 and 2.0 times higher than that of the pristine hcp- and fcc-Ru nanoparticles. The enhancements in activity and selectivity could be attributed to the open structure, high density of low-coordination surface atoms, and the fcc phase of Ru. Similarly, in another study, the fcc-Ru octahedral nanoframes also demonstrated significantly enhanced catalytic activity toward the dehydrogenation of ammonia borane.[74] Altogether, these two studies provide the opportunity to obtain nanoframe-based catalysts with high activity and selectivity by engineering their crystal phase. In addition to Ru-based catalysts, the fcc Rh−Cu octahedral nanoframes were also applied to catalyze the dehydrogenation of hydrazine at room temperature.[61] Compared to the solid Rh−Cu nanoparticles, the fcc Rh−Cu octahedral nanoframes showed a faster rate toward the dehydrogenation of hydrazine. However, they possessed a slightly lower H_2 selectivity (31.4%) than the Rh nanoparticles (36.2%), which can be, possibly, attributed to the adverse impact of Cu.

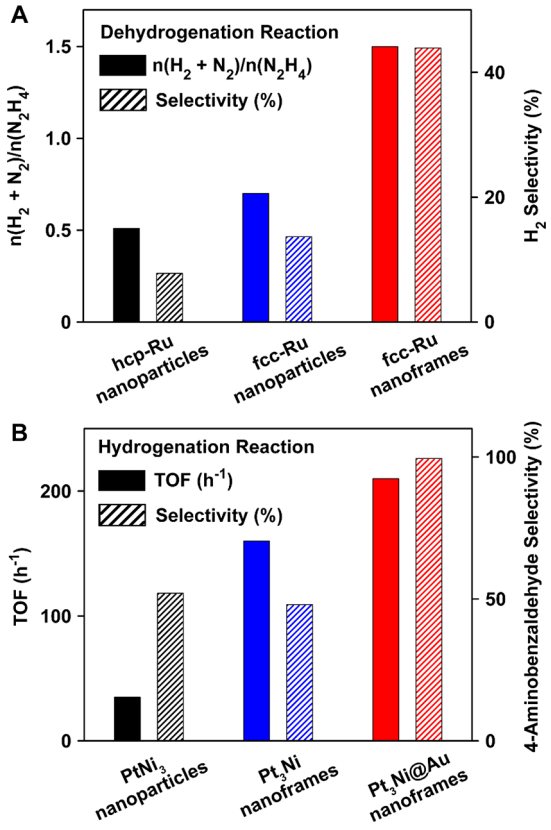

Figure 24. Applications of metal nanoframes in thermal catalysis. (A) Catalytic activity and selectivity toward the generation of hydrogen from the dehydrogenation of hydrazine and the molar ratios of the generated H_2 and N_2 over the initially added hydrazine, denoted as $n(H_2 + N_2)/n(N_2H_4)$, on hcp-Ru nanoparticles, fcc-Ru nanoparticles, and fcc-Ru nanoframes, respectively. (B) Catalytic activity and selectivity for the hydrogenation of 4-nitrobenzaldehyde on catalysts based on $PtNi_3$ nanoparticles, Pt_3Ni nanoframes, and Pt_3Ni@Au nanoframes, respectively. (A) Reproduced with permission from ref 75. Copyright 2019 American Chemical Society. (B) Reproduced with permission from ref 83. Copyright 2014 American Chemical Society.

4.2.2. Hydrogenation. Hydrogenation is an important process in industry, in which the addition of hydrogen to unsaturated organic compounds occurs in the presence of noble-metal catalysts.[116,117] For example, the hydrogenation of aromatic nitro and aldehyde compounds can produce the functionalized aromatic amines and alcohols, respectively. These chemical species are important intermediates for the production of a range of agrochemicals, pharmaceuticals, cosmetics, and polymers. Although aromatic nitro compounds can be reduced through the hydrogenation reaction, it remains challenging to promote the selectivity of a hydrogenation reaction when the reactant molecules consist of other reducible groups, such as C═C and C═O. As such, the hydrogenation of 4-nitrobenzaldehyde containing both $C{-}NO_2$ and C═O groups can often serve as a model reaction for evaluating the

https://dx.doi.org/10.1021/acs.chemrev.0c00940
Chem. Rev. 2021, 121, 796−833

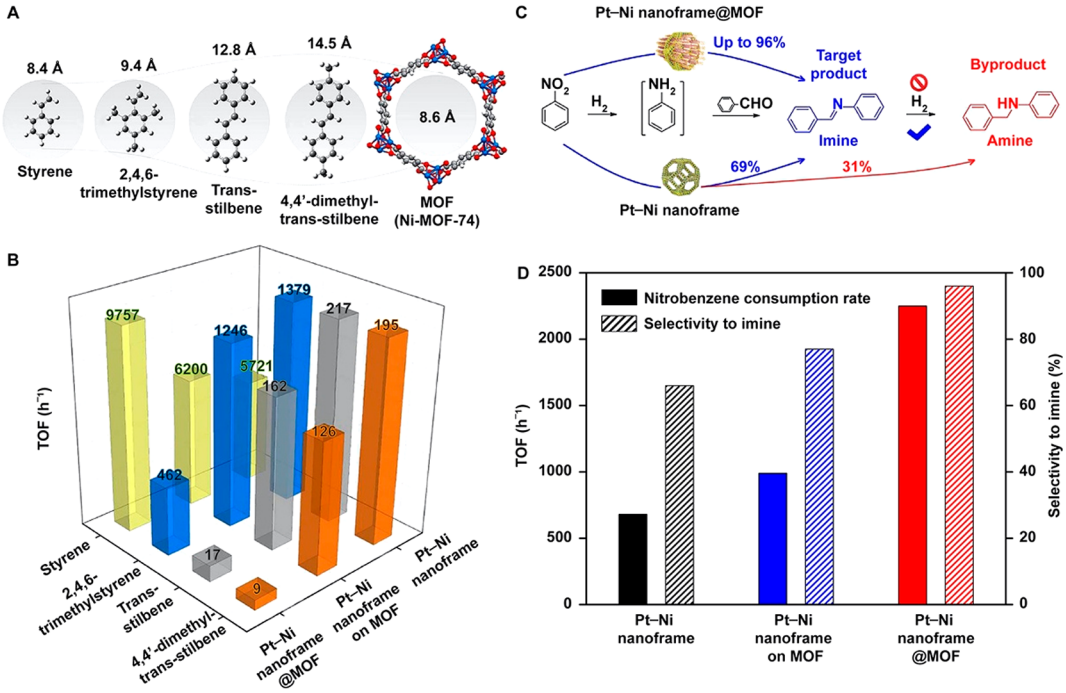

Figure 25. Application of Pt−Ni nanoframe@MOF hybrid nanostructures to thermal catalysis. (A) A comparison of the maximum diameters of four representative substrate molecules (styrene, 2,4,6-trimethylstyrene, *trans*-stilbene, and 4,4′-dimethyl-*trans*-stilbene) with the diameter of the pores in MOF (Ni-MOF-74). (B) Hydrogenation of styrene, 2,4,6-trimethylstyrene, *trans*-stilbene, and 4,4′-dimethyl-*trans*-stilbene catalyzed by the Pt−Ni nanoframes, Pt−Ni nanoframes supported on MOF, and Pt−Ni nanoframe@MOF hybrid nanostructures. (C) Schematic illustration of the size-selective catalysis in reductive imination of nitrobenzene. (D) Activity and selectivity to imine in the cascade reductive imination of nitrobenzene catalyzed by the Pt−Ni nanoframes, Pt−Ni nanoframes supported on MOF, and Pt−Ni nanoframe@MOF hybrid nanostructures. Reproduced with permission from ref 49. Copyright 2015 Nature Publishing Group.

catalytic performance of metal nanocrystals in terms of both activity and selectivity.

In one study, the Pt_3Ni@Au trimetallic nanoframes were constructed by the deposition of isolated Au clusters on the surface of Pt_3Ni truncated octahedral nanoframes through the galvanic replacement reaction between Ni and $HAuCl_4$.[83] They were further demonstrated as catalysts with high activity and selectivity toward the conversion of 4-nitrobenzaldehyde to 4-aminobenzaldehyde, together with a byproduct of 4-nitrobenzyl alcohol, under a H_2 condition at room temperature. As shown in Figure 24B, the Pt_3Ni@Au nanoframes exhibited a much higher turnover frequency (TOF, 208 h^{-1}) than those of the $PtNi_3$ solid nanocrystals (33 h^{-1}) and Pt_3Ni nanoframes (156 h^{-1}). Remarkably, the Pt_3Ni@Au nanoframes showed almost 100% selectivity toward 4-aminobenzaldehyde. It was argued that the higher value of TOF might arise from the localized electron transfer between the Au clusters and Pt_3Ni nanoframes, while the enhanced selectivity might originate from the selective adsorption of nitro groups on the surface of Au clusters. In addition to the hydrogenation of 4-nitrobenzaldehyde, other studies have also demonstrated that the hydrogenation of 4-nitrophenol to 4-aminophenol in the presence of $NaBH_4$ could be accelerated by nanoframes made of fcc-Ru or Ag−Pd alloy.[71,74]

Although metal nanoframes serve as highly active catalysts for the selective hydrogenation of organic compounds, their performance could deteriorate if the reaction mixture contained multiple competitive reducible organic compounds. By combining Pt−Ni nanoframes with a functional MOF, a nanoframe-based hybrid nanostructure was used as a catalyst to achieve efficient and selective hydrogenation of a specific olefin in a mixture with other olefin compounds.[49] It was argued that the porous architecture of the MOF could play its role as a molecular sieve to increase the selectivity for certain hydrogenation reactions depending on the size (d) of the molecule. As shown in Figure 25A, a mixture of four olefin molecules including styrene (d = 8.4 Å), 2,4,6-trimethylstyrene (d = 9.4 Å), *trans*-stilbene (d = 12.8 Å), and 4,4′-dimethyl-*trans*-stilbene (d = 14.5 Å) was used in a hydrogenation process that involved the use of Pt−Ni nanoframe@MOF hybrid nanostructures (d_{pore} = 8.6 Å) as a catalyst. While styrene molecules were small enough to pass through the pores in the MOF, the diffusion of other larger molecules would be limited, making it difficult for them to access the surface of the Pt−Ni nanoframes covered by the MOF. Figure 25B shows that the Pt−Ni nanoframe@MOF hybrid nanostructures could selectively catalyze the hydrogenation of styrene with high activity (TOF = 9757 h^{-1}) to produce a highly pure product compared to the cases of the pristine Pt−Ni nanoframes and Pt−Ni nanoframes deposited on MOF. Figure 25C illustrates that the Pt−Ni nanoframe@MOF hybrid nanostructures could be used to yield imines (the target product) instead of amines (the byproduct) in the cascade reductive imination of nitrobenzene in an ethanol solution under H_2 pressure. Figure 25D shows that the catalytic activity of Pt−Ni nanoframe@MOF hybrid nanostructures in generating imines was ∼3.3 and 2.4 times as great as those of the pristine Pt−Ni nanoframes and Pt−Ni nanoframes supported on MOF, respectively. Additionally, the Pt−Ni nanoframe@MOF hybrid nanostructures also gave a selectivity of 96% toward imine for the hydrogenation of nitrobenzene. These results suggest that the over-reduction of imine to amine can be effectively retarded, because the MOF with uniform pores can help achieve size

https://dx.doi.org/10.1021/acs.chemrev.0c00940
Chem. Rev. 2021, 121, 796−833

selectivity and suppress the diffusion of imine toward the interior Pt−Ni nanoframes once the condensation process is completed.

4.2.3. Suzuki Coupling. The Suzuki coupling refers to a Pd-catalyzed cross-coupling reaction between an organoboronate and an organohalide.[118] It represents an essential route to pharmaceuticals and agrochemicals. Recently, it was demonstrated that the encapsulation of Au octahedra in Pd cubic nanoframes could endorse the superior catalytic activity of nanoframes toward the Suzuki coupling reaction under the irradiation of a xenon lamp. In a typical synthesis, the Au octahedral nanocrystals were prepared and then used as seeds for the overgrowth of cubic Pd to generate Au@Pd core−shell nanocrystals, followed by controlling the etching and deposition rates at different sites of Pd to produce Au@Pd core−frame nanocrystals.[66] In this study, the Suzuki coupling between iodobenzene and phenylboronic acid to produce biphenyl served as a model reaction for evaluating the catalytic performance. Specifically, the yields of biphenyl were measured for the Au@Pd core−frame nanocrystals, Au octahedral nanocrystals, and Pd nanoframes, respectively. After 5 h of reaction, the yield of biphenyl for the Au@Pd core−frame nanocrystals reached over 90%, which was ∼6.9 and 5 times higher than those of Au octahedral nanocrystals (13%) and Pd nanoframes (18%), respectively. These results indicate that the encapsulation of Au octahedral nanocrystals in the Pd nanoframes can accelerate the Suzuki coupling reaction. It was speculated that the improvement can be attributed to the enhanced light absorption by Au octahedral nanocrystals, increasing the local temperature due to photothermal heating.

4.3. Photocatalysis

Photocatalysis uses a combination of catalyst and light irradiation to accelerate the kinetics of a chemical reaction.[119−121] As a green technology, photocatalysis is attractive for both chemical synthesis and environmental protection. It can also be used to convert solar energy to chemical energy. When a plasmonic metal (e.g., Au or Ag) is integrated with a catalytic metal (e.g., Pd, Pt, or Rh), it is possible to localize the light field around the surface of a nanocrystal to enhance its catalytic activity.[8,66] Additionally, metal nanoframes have been integrated with semiconductors to form hybrid nanostructures for achieving an improved catalytic efficiency.[121] Compared with semiconductor-based photocatalysts, metal nanoframes can improve the photocatalytic activity through three different mechanisms.[39−42,46,47,66] First, the metal nanoframes could retard the electron−hole recombination by serving as an electron sink for the storage of light-excited electrons.[46,47] Second, nanoframes made of a plasmonic metal featuring a strong LSPR can promote the light-harvesting capability of semiconductor in the UV, visible, or even near-infrared region depending on the size and morphology of the nanoframes involved.[39−42] Third, the nanoframes made of a plasmonic metal can absorb the light and convert it into heat, increasing the local temperature (see Section 4.2.3).[66] In this section, we discuss the photocatalytic applications of hybrid metal nanoframes containing semiconductors toward the degradation of organic compounds under light irradiation.

The photocatalytic degradation of organic pollutants by semiconductor-based photocatalysts is of great importance to environmental cleaning and protection.[46−48,121] Under light irradiation, the semiconductor-based photocatalyst could induce electron−hole pairs through a light excitation process. The electrons could then migrate to the surface of the semiconductor and be captured by the adsorbed O_2 molecules to generate superoxide anion radical (i.e., O_2^-). Concurrently, the holes could be easily trapped by OH^- on the surface of the semiconductor to further produce a hydroxyl radical species (i.e., ·OH). In the following steps, the organic pollutants would be partially or completely destroyed to form less toxic compounds and even CO_2 and H_2O molecules by the highly reactive radicals.[121] The integration of a semiconductor with plasmonic metal nanocrystals can improve the catalytic performance through the charge separation and/or light-harvesting advantages.

In one study, Au@Cu_2O core−shell nanoframes prepared through the deposition of p-type Cu_2O on the Au cubic nanoframes were used as catalysts for the degradation of methylene blue.[46] It was found that the photocatalytic degradation rate of methylene blue on the Au@Cu_2O core−shell nanoframes was much faster than that of pure Cu_2O nanospheres (2.50 vs 0.58 nM/min) in an aqueous solution under the irradiation of a xenon lamp equipped with a UV filter. Most interestingly, femtosecond pump−probe measurements revealed that the Au@Cu_2O core−shell nanoframes gave a longer lifetime for the light-excited electrons and holes compared to Cu_2O nanospheres (3.3 vs 1.0 ps). This result provided direct evidence to support the correlation between the rate of photocatalytic degradation and the lifetime of electrons and holes. It was hypothesized that the presence of Au, acting as an electron sink, could result in a more efficient electron−hole separation in the Au@Cu_2O core−shell nanoframes. As such, an increase in hole (and thus the hydroxyl radical) concentration could enhance the rate of degradation.

In another study, AgCl@Ag nanoframes consisting of uniformly distributed Ag nanoparticles on the surface of AgCl cubic nanoframes were fabricated through a simple photoreduction of the as-prepared AgCl cubic nanoframes.[47] Compared to the pristine AgCl nanoframes, the AgCl@Ag nanoframes exhibited a higher degradation rate for methyl orange dye under the irradiation of visible light. On the one hand, the UV−vis spectra confirmed that the AgCl@Ag nanoframes had a stronger extinction over the entire spectrum of visible light than that of the pristine AgCl nanoframes, arising from the LSPR of the Ag nanoparticles deposited on the nanoframes. On the other hand, transient photoluminescence spectra confirmed a restricted recombination process for the generation of electron−hole pairs in the AgCl@Ag nanoframes. These results suggest that the significantly enhanced photocatalytic performance of the AgCl@Ag nanoframes could be contributed to the strong LSPR effect of the Ag nanoparticles, together with the synergistic effect that facilitates interfacial charge transfer between Ag metal and AgCl semiconductor. With a similar strategy, it has been demonstrated that 2-D hybrid nanostructures composed of Au triangular plates and Pt triangular nanoframes on the reduced graphene oxide could serve as a highly efficient photocatalyst.[48]

5. ENHANCEMENT OF STABILITY

As discussed in Section 4, nanoframes promise augmented catalytic performance while offering an avenue to lower the cost of catalysts based on precious metals. However, given the presence of low-coordination atoms on the surface, especially those located at vertices, edges, and high-index facets, nanoframes should be considered a metastable structure kinetically trapped in a far-from-equilibrium state. As a kinetically controlled product, nanoframes are inherently less

https://dx.doi.org/10.1021/acs.chemrev.0c00940
Chem. Rev. 2021, 121, 796−833

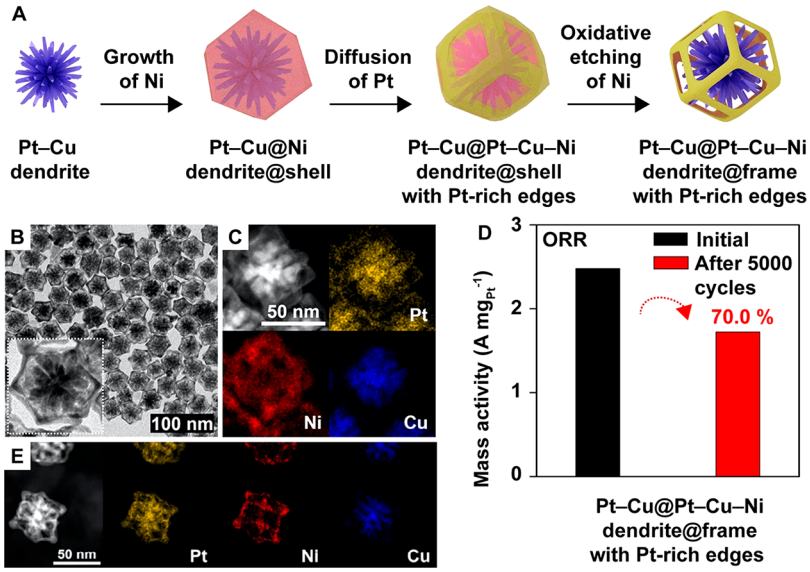

Figure 26. Stabilization of a metal nanoframe with an interior structural support. (A) Schematic illustration showing the synthesis of Pt−Cu@Pt−Cu−Ni dendrite@frame nanostructures. (B) TEM image of the nanostructures. (C) STEM image and the corresponding EDS mapping of such a nanostructure. (D) ORR mass activity of the nanostructures before and after 5000 cycles of the accelerated durability test. (E) STEM image and the corresponding EDS mapping of such a nanostructure after 5000 cycles of the accelerated durability test. Reproduced with permission from ref 50. Copyright 2017 American Chemical Society.

favorable in terms of thermodynamics relative to their solid counterparts. Therefore, they are vulnerable to morphological changes at elevated temperatures or under other harsh conditions. The elevation in temperature will supply the surface atoms with adequate kinetic energies to escape from their original locations and move to more stable sites through diffusion. For example, it was reported that Ru cuboctahedral nanoframes could only be preserved up to 300 °C in an inert atmosphere.[75] When the sample was heated to 400 °C, most of the ridges of the nanoframes would be broken, moving toward a state favored by thermodynamics.

For most catalytic applications such as fuel cell operation, NH_3 synthesis, or CO oxidation, the reactions are usually conducted at elevated temperatures and/or in acidic or alkaline media.[91−94,122−125] In these cases, nanoframes tend to fragment or collapse because of the migration of atoms, dissolution of leachable elements, and/or segregation of the elements.[37,50,51,58] It is worth pointing out that the actual working environment for some industrial catalysts is even harsher than those that are involved in the aforementioned applications. For example, the three-way catalytic converter, a device involving the use of catalytic nanoparticles based on Pd, Pt, and/or Rh to mitigate exhaust emission, operates in a broad temperature range of 150−600 °C and even up to higher temperatures depending on the engine condition.[125] In all these cases, nanoframe-based catalysts are anticipated to experience both structural and compositional changes during operation, leading to deterioration and even failure in terms of catalytic performance.[58] Taken together, it is often essential to greatly enhance the structural and compositional stability of noble-metal nanoframes before they can be adapted for practical applications. In this section, we focus on the stability (or durability) issue of nanoframes in catalysis, as well as the strategies for improving their structural robustness and compositional stability.

5.1. Reinforcement of the Backbone

Nanoframes can be mechanically reinforced by introducing a more robust structural support. For example, adding an internally positioned support could prevent the inherently flimsy nanoframe from collapsing under thermal stress or other extreme conditions. The internal support should have overall dimensions similar to those of the cavity in the nanoframe, making it impossible to detach from the nanoframe during a catalytic reaction. It should also be skeletal enough, different from the solid core in a core−frame structure, to minimize the sacrifice of catalytically active sites caused by the contact between the nanoframe and the support. Taking these factors into consideration, a structurally robust system was successfully developed, in which the Pt−Cu−Ni ternary nanoframe was structurally supported on a Pt−Cu dendrite.[50] Figure 26A shows a schematic illustration of the synthesis. Because of the difference in reduction kinetics among three precursors, namely, $Pt(acac)_2$, $Cu(acac)_2$, and $Ni(acac)_2$, in a one-pot synthesis, a dendritic core comprised of mainly Pt and Cu was initially formed in a synthesis, followed by the overgrowth of the subsequently produced Ni atoms for the generation of a Pt−Cu@Ni core−shell structure. Next, the Pt atoms migrated across the Ni matrix to the edges via directional diffusion, promoting the reduction of the remaining Cu(II) precursor in the reaction mixture for the production of a Pt−Cu−Ni frame around the Ni matrix. Finally, chemical etching with a HCl solution removed the leachable fractions of Ni and Cu, leaving behind a nanoframe supported on a dendrite in the form of Pt−Cu@Pt−Cu−Ni. Figure 26B shows a TEM image of the as-prepared Pt−Cu@Pt−Cu−Ni nanostructures, from which one can observe a rhombic dodecahedral morphology. The HAADF-STEM image and the corresponding elemental mapping data in Figure 26C further confirm the spatial distributions of the elements, revealing a Pt−Cu binary alloy and a Pt−Cu−Ni ternary alloy for the dendrite and nanoframe, respectively. The as-prepared Pt−Cu@Pt−Cu−Ni nanostructures showed a superior mass activity of 2.48 A/mg_{Pt} toward ORR at 0.9 V, which was 11 times as high as that of the commercial Pt/C. On the basis of an accelerated durability test (Figure 26D), the mass activity only decreased by 30% after 5000 cycles. The superb

https://dx.doi.org/10.1021/acs.chemrev.0c00940
Chem. Rev. 2021, 121, 796−833

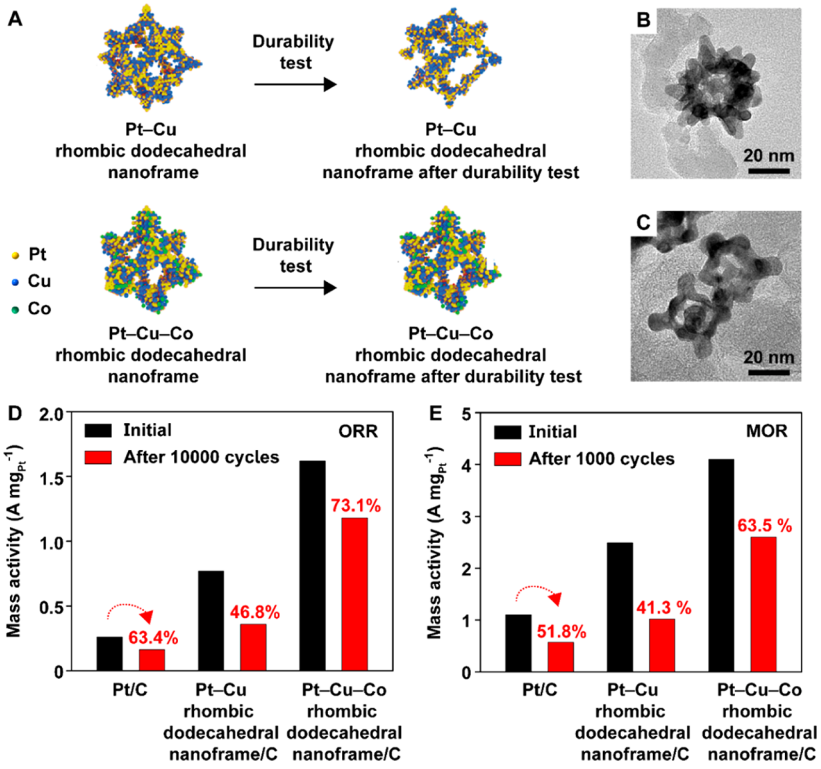

Figure 27. Preservation of metal nanoframes by introducing a dopant into the crystal lattice. (A) Schematic illustration showing changes to the binary Pt−Cu rhombic dodecahedral nanoframe and ternary Pt−Cu−Co nanoframe before and after the accelerated durability test. (B, C) TEM images of (B) Pt−Cu and (C) Pt−Cu−Co nanoframes after 1000 cycles of the accelerated durability test toward MOR. (D, E) Comparison of the mass activities of the different electrocatalysts before and after (D) 10 000 cycles of the accelerated durability test toward ORR and (E) 1000 cycles of the accelerated durability test toward MOR. Reproduced with permission from ref 63. Copyright 2018 Wiley-VCH Verlag GmbH & Co.

structure stability of the dendrite-supported Pt−Cu−Ni nanoframes was also verified by analyzing the sample post the accelerated durability test with HAADF-STEM imaging and elemental mapping. As shown in Figure 26E, there was essentially no change to the compositions for both the dendritic support and the nanoframe.

On the basis of a similar strategy, a dendrite-shaped Pt−Ni nanostructure has recently been leveraged to fortify Pt−Ni multiframes for the achievement of enhanced catalytic durability.[51] Different from the Pt−Cu@Pt−Cu−Ni nanostructure shown in Figure 26, where the Pt−Cu dendrite had a limited catalytic activity, both the inner dendrite and the outer multiframes embraced excellent catalytic activity thanks to the use of a Pt−Ni alloy, leading to a 30-time increase in ORR mass activity at 0.93 V relative to the commercial Pt/C catalyst. More importantly, the exceptional catalytic activity of the dendrite-supported Pt−Ni multiframes experienced much less loss after 5000 or 10 000 cycles of the accelerated durability test when compared with the Pt/C catalyst. This study demonstrates the feasibility to achieve both enhanced catalytic activity and long-term durability for the dendrite-fortified Pt−Ni nanoframes.

In addition to the use of a support by leveraging a dendritic structure, it has also been reported that nanoframes could be fabricated with enhanced catalytic durability if two nanoframes are combined into one unit for the generation of a double-layered nanoframe@nanoframe structure. As discussed in Section 3.3 and illustrated by Figure 20, Ir−Ni−Cu double-layered nanoframes could be obtained by leveraging the difference in reduction kinetics among four different metal precursors and post-synthesis etching.[44] Compared with the single-layered Ir−Ni−Cu nanoframes and commercial Ir/C catalyst, the as-synthesized double-layered nanoframes not only showed the highest initial Ir-based mass activity toward OER but also exhibited the best long-term durability after 2500 cycles of the accelerated durability test in an acidic medium. Specifically, the OER polarization curve, as well as their mass activity, remained essentially the same before and after the durability test. Unlike the single-layered nanoframes that tended to aggregate to a certain extent, the double-layered nanoframes retained their dispersion on the support very well during the durability test. The outstanding activity and durability of the double-layered nanoframes could be attributed to the unique nanoframe@nanoframe architecture, the formation of IrO_2 during the durability test, and the existence of multiple grain boundaries in the as-prepared nanostructures to alleviate structural deformation during the catalytic process.

A structurally more robust component can also be implanted into a nanoframe for use as a "hard skeleton" to fortify the nanoframe.[45,81,82] In one study, a hard Pt skeleton was introduced into an octahedral Au nanoframe to achieve enhanced structural stability.[82] The synthetic route includes the site-specific deposition of Pt on Au octahedral nanocrystals, selective etching of the Au core, and regrowth of Au on the Pt skeleton. Remarkably, the Au octahedral nanoframes reinforced with a Pt skeleton experienced no observable morphological change even when utilized under extreme pH conditions (e.g., at pH = 1.5, 7, and 12.5) or even treated with O_2 plasma. In comparison, under similar conditions, the Au octahedral nanoframes without a Pt skeleton were found to undertake aggregation and/or collapse for the frame structure. The outstanding stability could be attributed to the presence of an embedded hard skeleton made of Pt. Although only octahedral

https://dx.doi.org/10.1021/acs.chemrev.0c00940
Chem. Rev. 2021, 121, 796−833

and cubic Au nanoframes fortified with a Pt skeleton were demonstrated in detail in this study, it is believed that one could potentially generalize this approach for the fabrication of Pt-reinforced nanoframes with other morphologies.

5.2. Optimization of the Composition

In addition to its structure, the elemental composition of a nanoframe also contributes to its structural stability, as well as its durability in a catalytic application. On the one hand, different metals have distinct resistance to corrosion, oxidation, and reduction under harsh environments such as elevated temperature, high pressure, increased humidity, and strong acid or base, as well as other unidentified environmental factors. To this end, it is important to optimize the composition of nanoframes for a specific catalytic reaction to accommodate the specific conditions in order to achieve a long-term operation. On the other hand, one can manipulate the spatial distributions of different elements in the nanoframe and place the most resistant element at the weakest sites. For example, it is possible to fabricate a heterogeneous nanoframe, in which the most vulnerable vertices are composed of the heat-, oxidation-/reduction-, and/or acid/base-resistant elements, whereas the less vulnerable parts are made of the catalytically more active metals.

A common approach to enhancing the performance of a nanocatalyst is to add a new element, namely, a dopant, to the nanostructure.[63,126−128] It is argued that the introduction of a dopant could optimize the electronic structure of the catalytically active metal(s), alter their interactions with the reaction intermediates, and even introduce lattice strain into the system. These factors can also be exploited to prevent the dissolution of a specific metal from a catalyst during the operation process, which would consequently protect the overall structure against destruction. The choice of dopant could be a noble metal. For example, it was reported that doping Pt−Ni octahedral nanocrystals with a proper amount of Rh could greatly enhance their morphological stability during ORR.[126] The dopant can also be other transition metals, such as Mo, as shown in the case of Mo-doped Pt_3Ni octahedral nanocrystals.[127] DFT calculations suggested that the formation of surface Mo−oxide might be responsible for the enhanced durability of the Mo-doped nanocrystals. Additionally, it was reported that nonmetallic elements could also be introduced to improve the catalytic stability of metal nanocrystals. For example, P has been used to dope Pt−Ni concave octahedral nanocrystals, and the resultant nanocrystals showed greatly enhanced catalytic activity and durability under alkaline conditions.[128]

With the introduction of a small amount of Co into Pt−Cu rhombic dodecahedral nanoframes, ternary nanoframes with superior stability were obtained (Figure 27).[63] The as-obtained ternary nanoframes embraced not only enhanced catalytic activity toward both ORR and MOR but also improved structural and compositional stability compared to their binary Pt−Cu counterparts. The synthesis started from the formation of Cu-rich Pt−Cu−Co solid rhombic dodecahedral nanocrystals (at an atomic ratio of Pt/Cu/Co = 31.4:64.5:4.1), with Pt and Co atoms being mainly situated in proximity to the edges. When subjected to a selective etching of the core material using acetic acid, Pt−Cu−Co nanoframes featuring an atomic ratio of Pt/Cu/Co = 43.8:47.3:8.9 were obtained. The durability of the ternary nanoframes was then evaluated and compared with that of the binary Pt−Cu nanoframes toward ORR and MOR by applying the accelerated durability tests for 10 000 and 1000 cycles, respectively. Figure 27A−C shows that the morphology of the Pt−Cu−Co nanoframes remained essentially unaltered during the durability test, while the Pt−Cu nanoframes collapsed and lost their original morphology. To evaluate the catalytic durability, the mass activities of both types of nanoframes, as well as that of the commercial Pt/C, after the accelerated durability tests were calculated and then benchmarked against those of the same catalysts before the tests. As shown in Figure 27D,E, it is evident that the Co-doped ternary nanoframes not only showed remarkable initial mass activities toward both ORR and MOR but also retained their mass activities to the largest extent during the accelerated durability tests when benchmarked against the other two catalysts. These results indicate that elemental doping could effectively preserve the structure and the catalytic performance of metal nanoframes.

Different from doping, maneuvering the spatial distributions of the constituent elements in a nanoframe offers an alternative way to realize superior catalytic durability. In one study, a unique heterogeneous structure was demonstrated with outstanding durability toward MOR by decorating the vertices of Pt−Ni nanoframes with Au islands.[83] The Au-decorated Pt−Ni nanoframes were fabricated by decorating the vertices of Pt−Ni truncated octahedral nanocrystals with Au islands through the galvanic replacement reaction between Ni and $HAuCl_4$, followed by chemical etching to remove the solid core while the ratio of Pt to Ni was varied. When the loss of forward peak current density was compared after 3000 cycles of the accelerated durability test, the Au-decorated Pt−Ni nanoframes exhibited better durability relative to the Pt−Ni truncated octahedral nanocrystals and $PtNi_3$ nanoframes without the decoration of Au. It was argued that multiple reasons could be responsible for the enhanced durability. First, the catalytic oxidation of methanol would proceed via a more effective route in the presence of Au islands at the corners, limiting the formation of poisonous CO species. Second, the regulated chemical etching process would result in the formation of a phase-segregated Pt skin capable of protecting the open structure from dissolution. Third, the Au islands could work synergistically with Pt−Ni nanoframes in inhibiting the adsorption of poisonous intermediates onto the catalytic surface, which would prevent the loss of active sites and thus improve the long-term durability of the catalyst.

5.3. Post-Synthesis Treatment

On the one hand, as discussed above, a tight control of the composition and spatial distributions of the constituent elements during a synthesis can greatly improve the structural stability and catalytic durability of nanoframe-based catalysts. On the other hand, a post-synthesis treatment, such as those involving thermal annealing and/or acid washing of a newly prepared nanocatalyst before its use in a catalytic application, has been demonstrated to be of equal importance in maximizing the catalytic performance.[58,129,130] Such a treatment often causes alterations to the structure and/or composition of the catalyst, exerting a profound impact on the catalytic activity and durability of metal nanoframes. For example, it was reported that thermal annealing could be conducted not only to enhance contacts between the catalytic particle and the support (e.g., carbon and Al_2O_3) but also to induce a desired surface reconstruction on the catalytic particle.[129] Acid washing is often a required step before the use of Pt-based alloy catalysts (e.g., those made of Pt−Ni) in PEMFC.[130] During this process, the more reactive metal such as Ni will be leached out from the

https://dx.doi.org/10.1021/acs.chemrev.0c00940
Chem. Rev. 2021, 121, 796−833

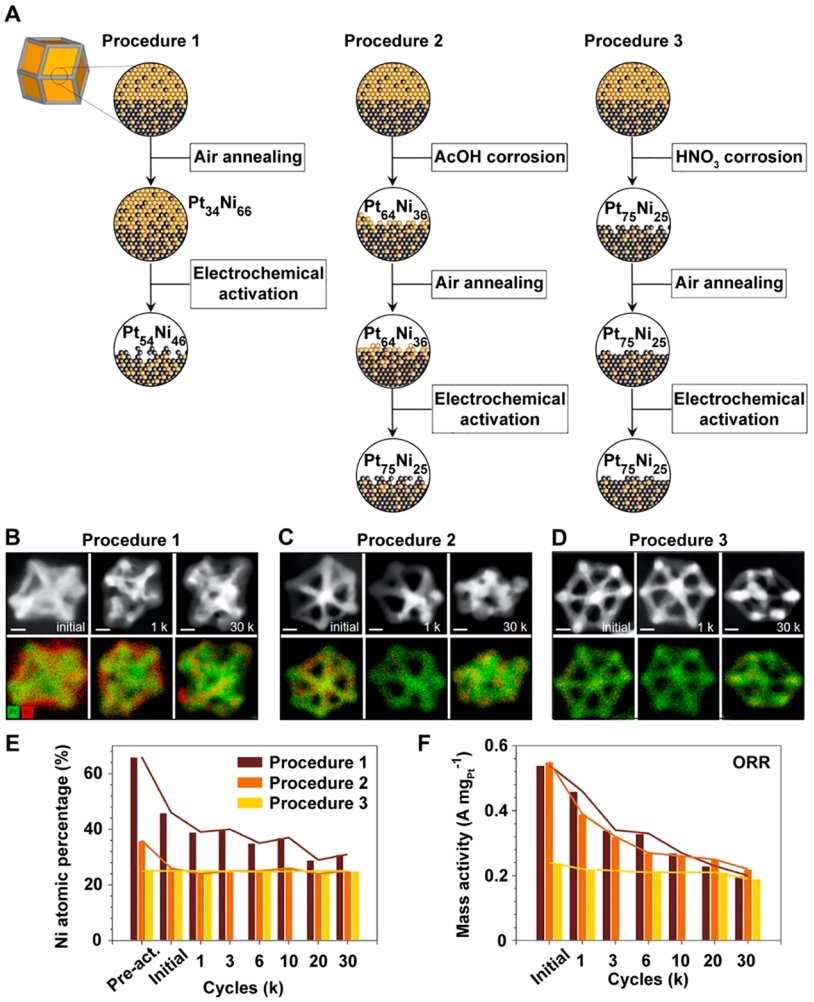

Figure 28. Comparison of metal nanoframes undergoing different post-synthesis treatments. (A) Schematic illustration of three different post-synthesis procedures for treating the Pt−Ni rhombic dodecahedral nanocrystals and the atomic structures at different stages. (B−D) HAADF-STEM and EDS images of the catalysts treated using (B) Procedure 1, (C) Procedure 2, and (D) Procedure 3. (E) Ni content and (F) ORR mass activity of the three different catalysts at various stages of test. Reproduced with permission from ref 58. Copyright 2018 American Chemical Society.

surface of the catalytic particle, generating a catalytically more active Pt-rich skin. This skin can also serve as a protective layer to prevent the more reactive metals from further dissolution by the acid. As a result, it is of critical importance to understand the effect of post-synthesis treatment on the structure and composition of nanoframes before one can come up with a suitable procedure to improve their catalytic activity and durability.

In a comparative study, the effect of a post-synthesis treatment on the catalytic activity and durability of Pt−Ni rhombic dodecahedral nanoframes as an ORR electrocatalyst was carefully examined.[58] In this work, Pt−Ni rhombic dodecahedral solid nanocrystals were first synthesized by injecting metal precursors into OAm at 265 °C and then treated using three different procedures. The treatment involved acid washing (with CH_3COOH or HNO_3), thermal annealing (in air and at 180 °C), and electrochemical activation (by potential cycling between 0.05 and 1.02 V in a $HClO_4$ solution saturated with inert gas). As illustrated in Figure 28A for the first group, the Pt−Ni rhombic dodecahedral nanocrystals were directly loaded on a carbon support without any washing step, followed by annealing in the air to remove the organic adsorbates and then electrochemical activation to get rid of the unalloyed Ni species that would easily dissolve during potential cycling. For the second and third groups, the Pt−Ni rhombic dodecahedral nanocrystals were treated with CH_3COOH (AcOH, a weak acid) and HNO_3 (a strong acid), respectively, for the formation of nanoframes, before being loaded on the same carbon support for subsequent treatments and tests. To understand the influence of the post-synthesis treatment on the composition near the surface region of these three catalysts, the elemental composition of each catalyst was quantified by collecting EDS spectra at different stages (Figure 28B−D). While the air annealing process only changed the extent of alloying and did not impact the composition of the Pt−Ni nanocrystals, the electrochemical activation could significantly reduce the Ni content for the Pt−Ni nanocrystals in groups one and two. In contrast, the catalyst in group three did not experience any compositional change in the electrochemical activation step, because a stable composition (at an atomic ratio of Pt/Ni = 75:25) had already been achieved during the HNO_3 treatment. The compositional stability of the catalyst in group three indicates that the robust surface delivered by the HNO_3 treatment could prevent the leachable element (Ni) from dissolution during potential cycling.

https://dx.doi.org/10.1021/acs.chemrev.0c00940
Chem. Rev. 2021, 121, 796−833

To evaluate the structural rigidity of these three catalysts treated using different procedures, HAADF-STEM images were collected for each sample immediately after electrochemical activation and after 1000 or 30 000 cycles of the accelerated durability test toward ORR. Figure 28B−D shows that the Pt−Ni catalytic particles in group three were preserved well. However, those in group two lost their original morphology during the durability test, and in fact, they could hardly be identified after 30 000 cycles. In comparison, the catalytic particles in group one developed an indistinct structure even before the durability test due to the dissolution of Ni and the reconstruction of the nanostructure during the electrochemical activation step. The durability of these three catalysts was also assessed using the degradation curves of the elemental composition and the ORR mass activity at 0.95 V during the durability test, as shown in Figure 28E,F, respectively. The Pt−Ni catalytic particles in group three stood out for its exceptional compositional stability, as well as high durability, although its initial mass activity was relatively low. It should be pointed out that, even though the Pt−Ni catalytic particles in group one exhibited extraordinarily high activity in the initial stage compared to the other two groups, they are not well-suited for electrocatalytic applications. As a matter of fact, they could hardly be utilized in practice, because the dissolution of leachable elements during fuel cell operation would deteriorate the membrane and ionomer. As such, it can be concluded that the treatment procedure for the third group is more appropriate for processing the Pt−Ni electrocatalysts, and the overall performance of PEMFC would benefit from the stability of the catalyst over a long haul.

It is worth emphasizing that the post-synthesis treatment may not necessarily augment the catalytic activity. As discussed in the above case study, for example, the initial activity of the Pt−Ni nanoframes involving treatment with a strong acid was compromised, but the less-defective surface would become more resistant during the prolonged testing cycles.[58] In general, the optimal structure and composition for excellent durability may not be always in line with the optimal features for superior catalytic activity. As such, a delicate balance between the catalytic activity and durability should be taken into consideration when optimizing the nanoframes for a catalytic application.

6. CONCLUDING REMARKS

Noble-metal nanocrystals with hollow interiors have received considerable interest owing to their unique properties and potential applications related to catalysis and plasmonics. Among them, nanoframes consisting of ultrathin ridges have the most open structure, allowing molecules and even macromolecules to easily enter and exit the hollow interior. This unique feature makes them excellent candidates for catalytic applications. In this review article, we first introduce a number of approaches to the fabrication or synthesis of nanoframes, including a template-assisted assembly of nanoscale building blocks, face-selected carving of solid nanocrystals, edge-selected deposition on a template followed by etching, dealloying of hollow nanocrystals, and nanoframe-directed deposition. We then use a broad spectrum of examples to illustrate the mechanistic details underlying each synthesis for the fabrication of mono-, bi-, or multimetallic nanoframes with simple or complex morphologies, as well as heterostructured and hybrid systems. We further highlight the use of these nanoframes as catalytic materials toward reactions critical to fuel cells, water splitting, as well as dehydrogenation, hydrogenation, Suzuki coupling, and pollutant degradation. At the end, we discuss the recent progress in enhancing the durability of noble-metal nanoframes in catalysis by engineering the structural and compositional designs. Despite the incredible progress over the past decade, the widespread use of this novel class of nanomaterials still faces a number of issues. Here is a short list of those challenges, together with their potential solutions.

(1) *Precise control over the surface structure of nanoframes.* In principle, the catalytic activity and/or selectivity of metal nanoframes can be enhanced by manipulating the arrangement of atoms on the surface.[19,87] However, it remains a daunting challenge to control the surface structure of nanoframes, in particular, when their ridges are reduced to a few nanometers of thickness. Only a few studies have attempted to resolve the specific facets exposed on the ridges of nanoframes.[34−37] In this regard, it is of critical importance to further expand the capacity of a synthetic protocol to precisely control the atomic composition and arrangement on the outermost surface of a nanoframe. This goal can be, possibly, achieved by optimizing the experimental parameters involved in a synthesis, including the template, temperature, solvent, metal precursor, capping agent, and colloidal stabilizer.

(2) *Elucidating the mechanistic details involved in the synthesis of nanoframes.* As discussed in Sections 2.2 and 2.3, both oxidative etching and galvanic replacement are typically involved in carving out a nanoframe from a solid nanocrystal. In general, their contributions to the carving process may change in the course of a synthesis, making it difficult to achieve a precise control over the elemental composition and morphology of the products. For example, in the one-pot synthesis of Pt−Cu nanoframes, as the dissolved O_2 was depleted from the reaction solution with time, the galvanic replacement between Cu and Pt(II) precursor, rather than the oxidative etching caused by O_2/Br^- or O_2/ I^-, might become the dominant process in the later stage of a synthesis.[35,36,56] For the synthesis of Ru nanoframes from Pd@Ru core−frame nanocrystals, however, the galvanic replacement reaction between Pd and a Ru(III) precursor only played a major role in the early stage of a synthesis.[75] As a result, it is important to differentiate the roles played by oxidative etching and galvanic replacement in the course of a synthesis by carefully controlling and monitoring the experimental conditions.

(3) *Developing nanoframes made of high-abundance and low-cost metals.* As shown in Sections 2 and 3, most of the reported nanoframes are based on low-abundance and high-cost noble metals, including Au, Pd, Pt, Rh, Ru, and Ir.[69,71] It will be beneficial to have the synthesis extended to Ag and Cu, two noble metals that are more abundant and less expensive than other noble metals while still offering key plasmonic and catalytic properties. However, it is extremely difficult to synthesize nanoframes dominated by these two metals because of their higher reactivity than all other noble metals. Recently, a facile method was developed for the synthesis of Ag cubic nanoframes by reducing templates based on silver halide (i.e., $AgCl_{0.91}Br_{0.09}$ nanocubes) with $NaBH_4$.[131] On the one hand, this successful demonstration suggests that the use of various, well-defined salt nanocrystals as the

https://dx.doi.org/10.1021/acs.chemrev.0c00940
Chem. Rev. 2021, 121, 796−833

templates may offer a simple synthetic route to Ag and Cu nanoframes. On the other hand, it was reported that Pd solid nanocrystals could be directly transformed into Pd nanoframes by carefully manipulating the etching and redeposition rates at different sites (Figure 9).[55] This may provide another route to the fabrication of Ag or Cu nanoframes. Taken together, there is an urgent need to develop a general strategy for the synthesis of nanoframes made of Ag, Cu, and many other earth-abundant metals with various morphologies and further explore their plasmonic and catalytic properties.

(4) *Achieving a clean surface for the nanoframes*. In most cases, the solution-phase synthesis of noble-metal nanoframes involves the use of a colloidal stabilizer (e.g., PVP and CTAB) and/or a capping agent (e.g., Cl^-, Br^-, and I^-).[19,87] Although the nanoframes are repeatedly washed after a synthesis, these organic/inorganic species often remain on the surface of the nanoframes due to the involvement of chemisorption. Their presence could compromise the performance of the nanoframes in heterogeneous catalysis. This issue can be addressed through the development of effective protocols for removing the chemisorbed species after the synthesis or conducting the synthesis without involving any adsorbates. UV−ozone irradiation and thermal annealing are often used for the post-synthesis removal of chemisorbed molecules.[87] However, these treatments may induce irreversible aggregation or fusion in the nanostructures. In comparison, a synthesis conducted without the addition of any possible adsorbate is more attractive in generating nanoframes with a clean surface. To this end, it was reported that Au, Pd, and Pt nanoframes free of colloidal stabilizer and capping agent could be prepared through a galvanic replacement reaction that involved nanocrystal templates directly grown on solid substrates.[80]

(5) *Understanding the thermal stability of nanoframe structures*. As showcased in Section 4, metal nanoframes possess excellent catalytic properties owing to their unique features. However, note that nanoframes are far-from-equilibrium structures that tend to have compromised thermal stability, especially during a high-temperature catalysis. On the basis of in situ TEM observations in the cases of Au nanoribbons and Pd concave icosahedra, kinetically controlled products could change their morphologies via surface reconstruction and then evolve into the thermodynamically favorable structures through bulk reconstruction when subjected to heating.[132,133] On the one hand, for the metal nanoframes with ultrathin ridges, it is expected that their equilibration pathways may differ from their solid counterparts with similar dimensions. On the other hand, because most of the nanoframe catalysts are made of alloys (e.g., the Pt_3Ni nanoframes for ORR), phase separation or intermetallic formation might occur upon heating, increasing the complexity of an equilibration pathway for nanoframes.[38,43,58−60] Taken together, there is an urgent need to understand the stability of far-from-equilibrium nanoframes under thermal stress by tracking and analyzing the equilibration pathway in situ. The results from such studies are anticipated to enable the optimization of structural and compositional designs for enhancing the structural stability and thus catalytic durability of metal nanoframes.

(6) *Scaling up the production of nanoframes*. Although a wide variety of metal nanoframes have been successfully synthesized in high quality, the protocols mainly rely on conventional batch reactors with small reaction volumes (typically, 10−200 mL). When scaled up to large reaction volumes (e.g., 1000 mL), the thermal inhomogeneity and nonuniform spatial distributions of reactants throughout the reaction solution often result in poor quality control for the products. This will be especially problematic when preparing metal nanoframes with complex morphologies. One feasible solution is based upon the adoption of a continuous-flow reactor.[134,135] When the reaction solution is dispersed into a continuous train of small droplets, this system offers an opportunity to achieve high production volume while still maintaining a good control over the product quality.

(7) *Integrating noble-metal nanoframes with other functional materials*. In recent years, hybrid nanostructures consisting of a combination of two or more functional components have received ever-increasing interest in the field of catalysis. Because of the synergistic effect and/or coupling effect, the hybrid nanostructures can offer greatly enhanced or even completely new catalytic properties. For example, as discussed in Sections 3.3 and 4.2, an MOF has been successfully grown on the surface of Pt−Ni nanoframes to form a unique hybrid nanomaterial.[49] During the hydrogenation reaction involving a mixture of four different olefins, it is possible to achieve a high selectivity by limiting the access of substrate molecules larger than the pores of the MOF. In addition, other hybrid nanostructures based on metal nanoframes and semiconductors have been designed and fabricated to achieve photocatalysis in the context of chemical synthesis and environmental cleaning, as discussed in Section 4.3.[46−48] It is anticipated that integration of noble-metal nanoframes with other functional materials will bring in new properties and/or enhanced performance.

In conclusion, there is still a number of challenges that need to be addressed before we can elevate noble-metal nanoframes to the next level of success. It is hoped that the concepts and case studies presented in this review article can serve as a resource or starting point for researchers who are interested in developing new types of metal nanoframes and/or exploring their novel applications. Once our knowledge of this new class of nanomaterials has accumulated to a certain level, it might become a reality to design and rationally fabricate noble-metal nanoframes with the explicit properties for a specific application.

AUTHOR INFORMATION

Corresponding Author

Dong Qin − *School of Materials Science and Engineering, Georgia Institute of Technology, Atlanta, Georgia 30332, United States;* orcid.org/0000-0001-5206-5912; Email: dong.qin@mse.gatech.edu

Authors

Tung-Han Yang − *School of Materials Science and Engineering, Georgia Institute of Technology, Atlanta, Georgia 30332, United States;* orcid.org/0000-0001-6161-4397

https://dx.doi.org/10.1021/acs.chemrev.0c00940
Chem. Rev. 2021, 121, 796−833

Jaewan Ahn − *School of Materials Science and Engineering, Georgia Institute of Technology, Atlanta, Georgia 30332, United States*
Shi Shi − *School of Materials Science and Engineering, Georgia Institute of Technology, Atlanta, Georgia 30332, United States*
Peng Wang − *School of Materials Science and Engineering, Georgia Institute of Technology, Atlanta, Georgia 30332, United States*
Ruoqi Gao − *School of Materials Science and Engineering, Georgia Institute of Technology, Atlanta, Georgia 30332, United States*

Complete contact information is available at: https://pubs.acs.org/10.1021/acs.chemrev.0c00940

Notes

The authors declare no competing financial interest.

Biographies

Tung-Han Yang received his B.S. in Chemical Engineering from the National Cheng Kung University, Taiwan, in 2009. He studied at National Tsing Hua University, Taiwan, toward his M.S. and Ph.D. in Materials Science and Engineering in 2011 and 2017, respectively. From 2015 to 2017, he was a visiting Ph.D. student in Prof. Younan Xia's group at Georgia Tech. As a postdoctoral fellow under the supervision of Prof. Dong Qin at Georgia Tech, his current research focuses on the development of SERS for investigating nanocrystal growth, chemical reaction, and polymer physics. From 2021, he will start a tenure-track faculty position in the Department of Chemical Engineering at National Tsing Hua University, Taiwan.

Jaewan Ahn received his B.S. and Ph.D. in Materials Science and Engineering from Georgia Tech in 2015 and 2019, respectively. His doctoral research in Prof. Dong Qin's lab focused on the design and rational synthesis of multimetallic nanocrystals for plasmonics and catalysis. He is currently a postdoctoral fellow at the Korea Advanced Institute of Science and Technology (KAIST), where he is working toward the development of novel substrates featuring excellent SERS properties for applications as gas sensors with high selectivity.

Shi Shi is a Ph.D. student majoring in Materials Science and Engineering under the supervision of Prof. Dong Qin at Georgia Tech. She received her B.S. in Materials Physics and M.S. in Materials Science and Engineering from Nanjing University and Shanghai Jiao Tong University in 2014 and 2017, respectively. Her current research interests focus on bifunctional metal nanocrystals for catalyzing and reporting on chemical reactions by SERS.

Peng Wang received his B.S. in Inorganic Nonmetallic Materials Engineering from the Shandong University of Science and Engineering in 2010. He received his M.S. and Ph.D. in Materials Science from the Harbin Institute of Technology in 2012 and 2016, respectively. He began his position as a lecturer at Shandong University of Technology in July 2016. From 2018 to 2020, he was a postdoctoral fellow in Prof. Dong Qin's lab, during which time he focused on the design and rational synthesis of Ag-based bimetallic nanocrystals for applications in SERS.

Ruoqi Gao is a Ph.D. student in Materials Science and Engineering under the supervision of Prof. Dong Qin at Georgia Tech. She received her B.S. in Materials Science and Engineering from the Wuhan University of Technology in 2019. Her research focuses on bimetallic and trimetallic nanocrystals with integrated plasmonic and catalytic properties for monitoring chemical reactions by SERS.

Dong Qin is an Associate Professor of Materials Science and Engineering at Georgia Tech, with an adjunct appointment in the School of Chemistry and Biochemistry. Her academic records include a B.S. in Chemistry from Fudan University (1990), a Ph.D. in Physical Chemistry with Prof. Hai-Lung Dai from University of Pennsylvania (1996), a postdoctoral stint with Prof. George M. Whitesides at Harvard University (1996−1997), and an MBA from the University of Washington (2003). Before joining Georgia Tech in 2012, she held administrative positions as Associate Dean for Research in the School of Engineering and Applied Science at Washington University in St. Louis (2007−2011) and Associate Director of Center for Nanotechnology at the University of Washington (2002−2007). Her research group pioneered galvanic-replacement free synthesis of Ag-based bimetallic nanocrystals as unique bifunctional probes for probing catalytic reactions by SERS. Her current research focuses on the development of SERS as a new paradigm for in situ monitoring the heterogeneous nucleation in nanocrystal growth, the competitive binding of ligands on the surface of metal nanocrystals, and chemical reactions at the catalytically significant surface of metal nanocrystals.

ACKNOWLEDGMENTS

We acknowledge the support from the National Science Foundation (CHE-1412006 and CHE-1708300), ACS Petroleum Research Fund (PRF No. 59664-ND10), and startup funds from Georgia Tech. T.H.Y. acknowledges the Scholarship from the Postdoctoral Study Abroad Program of the Ministry of Science and Technology of Taiwan. P.W. acknowledges the partial support from the China Scholarship Council.

ABBREVIATIONS

2-D = two-dimensional
3-D = three-dimensional
AFC = alkaline fuel cell
CTAB = cetyltrimethylammonium bromide
CTAC = cetyltrimethylammonium chloride
DFAFC = direct-formic acid fuel cell
DFT = density functional theory
DMF = *N*,*N*-dimethylformamide
DMFC = direct-methanol fuel cell
DNA = deoxyribonucleic acid
DOE = Department of Energy
FAOR = formic acid oxidation reaction
FCC = face-centered cubic
EDS = energy-dispersive X-ray spectroscopy
EG = ethylene glycol
ETA = ethanolamine
HAADF = high-angle annular dark-field
HCP = hexagonal close packing
HER = hydrogen evolution reaction
HOR = hydrogen oxidation reaction
HRTEM = high-resolution TEM
LSPR = localized surface plasmon resonance
MCFC = molten carbonate fuel cell
MOF = metal−organic framework
MOR = methanol oxidation reaction
Ni-MOF-74 = MOF of Ni_2dobdc (where $dobdc^{4-}$ refers to 2,5-dioxidoterephthalate)
OAm = oleylamine
ODA = octadecylamine
OER = oxygen evolution reaction
ORR = oxygen reduction reaction
PAFC = phosphoric acid fuel cell

https://dx.doi.org/10.1021/acs.chemrev.0c00940
Chem. Rev. 2021, 121, 796−833

PEMFC = proton-exchange membrane fuel cell
PGM = platinum-group metal
PVP = poly(vinylpyrrolidone)
SERS = surface-enhanced Raman scattering
STEM = scanning transmission electron microscopy
SOFC = solid oxide fuel cell
TEG = triethylene glycol
TEM = transmission electron microscopy
TOF = turnover frequency
XANES = X-ray absorption near-edge structure
XPS = X-ray photoelectron spectroscopy
XRD = X-ray diffraction

REFERENCES

(1) Mizuno, N.; Misono, M. Heterogeneous Catalysis. *Chem. Rev.* **1998**, *98*, 199−218.
(2) Somorjai, G. A.; Li, Y. Impact of Surface Chemistry. *Proc. Natl. Acad. Sci. U. S. A.* **2011**, *108*, 917−924.
(3) Stamenkovic, V. R.; Strmcnik, D.; Lopes, P. P.; Markovic, N. M. Energy and Fuels from Electrochemical Interfaces. *Nat. Mater.* **2017**, *16*, 57−69.
(4) Liu, L.; Corma, A. Metal Catalysts for Heterogeneous Catalysis: From Single Atoms to Nanoclusters and Nanoparticles. *Chem. Rev.* **2018**, *118*, 4981−5079.
(5) Zhang, J.; Winget, S. A.; Wu, Y.; Su, D.; Sun, X.; Xie, Z.-X.; Qin, D. Ag@Au Concave Cuboctahedra: A Unique Probe for Monitoring Au-Catalyzed Reduction and Oxidation Reactions by Surface-Enhanced Raman Spectroscopy. *ACS Nano* **2016**, *10*, 2607−2616.
(6) Xia, Y.; Xiong, Y.; Lim, B.; Skrabalak, S. E. Shape-Controlled Synthesis of Metal Nanocrystals: Simple Chemistry Meets Complex Physics? *Angew. Chem., Int. Ed.* **2009**, *48*, 60−103.
(7) Gilroy, K. D.; Ruditskiy, A.; Peng, H.-C.; Qin, D.; Xia, Y. Bimetallic Nanocrystals: Syntheses, Properties, and Applications. *Chem. Rev.* **2016**, *116*, 10414−10472.
(8) Shi, S.; Qin, D. Bifunctional Metal Nanocrystals for Catalyzing and Reporting on Chemical Reactions. *Angew. Chem., Int. Ed.* **2020**, *59*, 3782−3792.
(9) Sun, X.; Yang, X.; Zhang, Y.; Ding, Y.; Su, D.; Qin, D. Pt-Ag Cubic Nanocages with Wall Thickness Less Than 2 nm and Their Enhanced Catalytic Activity Toward Oxygen Reduction. *Nanoscale* **2017**, *9*, 15107−15114.
(10) Wu, Y.; Sun, X.; Yang, Y.; Li, J.; Zhang, Y.; Qin, D. Enriching Silver Nanocrystals with a Second Noble Metal. *Acc. Chem. Res.* **2017**, *50*, 1774−1784.
(11) Gao, C.; Low, J.; Long, R.; Kong, T.; Zhu, J.; Xiong, Y. Heterogeneous Single-Atom Photocatalysts: Fundamentals and Applications. *Chem. Rev.* **2020**, *120*, 12175−12216.
(12) Qin, R.; Liu, K.; Wu, Q.; Zheng, N. Surface Coordination Chemistry of Atomically Dispersed Metal Catalysts. *Chem. Rev.* **2020**, *120*, 11810−11899.
(13) Ross, M. B.; De Luna, P.; Li, Y.; Dinh, C.-T.; Kim, D.; Yang, P.; Sargent, E. H. Designing Materials for Electrochemical Carbon Dioxide Recycling. *Nat. Catal.* **2019**, *2*, 648−658.
(14) Zhang, Y.; Wu, Y.; Qin, D. Rational Design and Synthesis of Bifunctional Metal Nanocrystals for Probing Catalytic Reactions by Surface-Enhanced Raman Scattering. *J. Mater. Chem. C* **2018**, *6*, 5353−5362.
(15) Ahn, J.; Zhang, L.; Qin, D. Transforming Noble-Metal Nanocrystals into Complex Nanostructures through Facet-Selective Etching and Deposition. *ChemNanoMat* **2020**, *6*, 5−14.
(16) Ahn, J.; Kim, J.; Qin, D. Orthogonal Deposition of Au on Different Facets of Ag Cuboctahedra for the Fabrication of Nanoboxes with Complementary Surfaces. *Nanoscale* **2020**, *12*, 372−379.
(17) Shi, S.; Zhang, Y.; Ahn, J.; Qin, D. Revitalizing Silver Nanocrystals as a Redox Catalyst by Modifying Their Surface with an Isocyanide-Based Compound. *Chem. Sci.* **2020**, *11*, 11214−11223.
(18) Liu, M.; Zhao, Z.; Duan, X.; Huang, Y. Nanoscale Structure Design for High-Performance Pt-Based ORR Catalysts. *Adv. Mater.* **2019**, *31*, 1802234.
(19) Shi, Y.; Lyu, Z.; Zhao, M.; Chen, R.; Nguyen, Q. N.; Xia, Y. Noble-Metal Nanocrystals with Controlled Shapes for Catalytic and Electrocatalytic Applications. *Chem. Rev.* **2020**, DOI: 10.1021/acs.chemrev.0c00454.
(20) Long, R.; Zhou, S.; Wiley, B. J.; Xiong, Y. Oxidative Etching for Controlled Synthesis of Metal Nanocrystals: Atomic Addition and Subtraction. *Chem. Soc. Rev.* **2014**, *43*, 6288−6310.
(21) Li, J.; Liu, J.; Yang, Y.; Qin, D. Bifunctional Ag@Pd-Ag Nanocubes for Highly Sensitive Monitoring of Catalytic Reactions by Surface-Enhanced Raman Spectroscopy. *J. Am. Chem. Soc.* **2015**, *137*, 7039−7042.
(22) Zhao, M.; Wang, X.; Yang, X.; Gilroy, K. D.; Qin, D.; Xia, Y. Hollow Metal Nanocrystals with Ultrathin, Porous Walls and Well-Controlled Surface Structures. *Adv. Mater.* **2018**, *30*, 1801956.
(23) Park, J.; Kwon, T.; Kim, J.; Jin, H.; Kim, H. Y.; Kim, B.; Joo, S. H.; Lee, K. Hollow Nanoparticles as Emerging Electrocatalysts for Renewable Energy Conversion Reactions. *Chem. Soc. Rev.* **2018**, *47*, 8173−8202.
(24) Qian, J.; Shen, M.; Zhou, S.; Lee, C.-T.; Zhao, M.; Lyu, Z.; Hood, Z. D.; Vara, M.; Gilroy, K. D.; Wang, K.; et al. Synthesis of Pt Nanocrystals with Different Shapes Using the Same Protocol to Optimize Their Catalytic Activity Toward Oxygen Reduction. *Mater. Today* **2018**, *21*, 834−844.
(25) Hayden, B. E. Particle Size and Support Effects in Electrocatalysis. *Acc. Chem. Res.* **2013**, *46*, 1858−1866.
(26) Van Hardeveld, R.; Hartog, F. The Statistics of Surface Atoms and Surface Sites on Metal Crystals. *Surf. Sci.* **1969**, *15*, 189−230.
(27) Shao, M.; Peles, A.; Shoemaker, K. Electrocatalysis on Platinum Nanoparticles: Particle Size Effect on Oxygen Reduction Reaction Activity. *Nano Lett.* **2011**, *11*, 3714−3719.
(28) Dai, Y.; Lu, P.; Cao, Z.; Campbell, C. T.; Xia, Y. The Physical Chemistry and Materials Science behind Sinter-Resistant Catalysts. *Chem. Soc. Rev.* **2018**, *47*, 4314−4331.
(29) Xia, Y.; Yang, X. Toward Cost-Effective and Sustainable Use of Precious Metals in Heterogeneous Catalysts. *Acc. Chem. Res.* **2017**, *50*, 450−454.
(30) Nosheen, F.; Anwar, T.; Siddique, A.; Hussain, N. Noble Metal Based Alloy Nanoframes: Syntheses and Applications in Fuel Cells. *Front. Chem.* **2019**, *7*, 456.
(31) Fang, Z.; Wang, Y.; Liu, C.; Chen, S.; Sang, W.; Wang, C.; Zeng, J. Rational Design of Metal Nanoframes for Catalysis and Plasmonics. *Small* **2015**, *11*, 2593−2605.
(32) Wang, X.; Ruditskiy, A.; Xia, Y. Rational Design and Synthesis of Noble-Metal Nanoframes for Catalytic and Photonic Applications. *Natl. Sci. Rev.* **2016**, *3*, 520−533.
(33) Wang, X.; Figueroa-Cosme, L.; Yang, X.; Luo, M.; Liu, J.; Xie, Z.; Xia, Y. Pt-Based Icosahedral Nanocages: Using a Combination of {111} Facets, Twin Defects, and Ultrathin Walls to Greatly Enhance Their Activity Toward Oxygen Reduction. *Nano Lett.* **2016**, *16*, 1467−1471.
(34) Xiong, L.; Sun, Z.; Zhang, X.; Zhao, L.; Huang, P.; Chen, X.; Jin, H.; Sun, H.; Lian, Y.; Deng, Z.; et al. Octahedral Gold-Silver Nanoframes with Rich Crystalline Defects for Efficient Methanol Oxidation Manifesting a CO-Promoting Effect. *Nat. Commun.* **2019**, *10*, 3782.
(35) Luo, S.; Shen, P. K. Concave Platinum−Copper Octopod Nanoframes Bounded with Multiple High Index Facets for Efficient Electrooxidation Catalysis. *ACS Nano* **2017**, *11*, 11946−11953.
(36) Zhang, Z.; Luo, Z.; Chen, B.; Wei, C.; Zhao, J.; Chen, J.; Zhang, X.; Lai, Z.; Fan, Z.; Tan, C.; et al. One-Pot Synthesis of Highly Anisotropic Five-Fold-Twinned PtCu Nanoframes Used as a Bifunctional Electrocatalyst for Oxygen Reduction and Methanol Oxidation. *Adv. Mater.* **2016**, *28*, 8712−8717.
(37) Qin, Y.; Zhang, W.; Guo, K.; Liu, X.; Liu, J.; Liang, X.; Wang, X.; Gao, D.; Gan, L.; Zhu, Y.; et al. Fine-Tuning Intrinsic Strain in Penta-Twinned Pt−Cu−Mn Nanoframes Boosts Oxygen Reduction Catalysis. *Adv. Funct. Mater.* **2020**, *30*, 1910107.

https://dx.doi.org/10.1021/acs.chemrev.0c00940
Chem. Rev. 2021, 121, 796−833

(38) Chen, C.; Kang, Y.; Huo, Z.; Zhu, Z.; Huang, W.; Xin, H. L.; Snyder, J. D.; Li, D.; Herron, J. A.; Mavrikakis, M.; et al. Highly Crystalline Multimetallic Nanoframes with Three-Dimensional Electrocatalytic Surfaces. *Science* **2014**, *343*, 1339−1343.
(39) Ahn, J.; Wang, D.; Ding, Y.; Zhang, J.; Qin, D. Site-Selective Carving and Co-Deposition: Transformation of Ag Nanocubes into Cancaved Nanocrystals Encased by Ag-Au Alloy Frames. *ACS Nano* **2018**, *12*, 298−307.
(40) Zhang, L.; Liu, T.; Liu, K.; Han, L.; Yin, Y.; Gao, C. Gold Nanoframes by Nonepitaxial Growth of Au on AgI Nanocrystals for Surface-Enhanced Raman Spectroscopy. *Nano Lett.* **2015**, *15*, 4448−4454.
(41) Lu, X.; Au, L.; McLellan, J.; Li, Z.-Y.; Marquez, M.; Xia, Y. Fabrication of Cubic Nanocages and Nanoframes by Dealloying Au/Ag Alloy Nanoboxes with an Aqueous Etchant Based on $Fe(NO_3)_3$ or NH_4OH. *Nano Lett.* **2007**, *7*, 1764−1769.
(42) Au, L.; Chen, Y.; Zhou, F.; Camargo, P. H. C.; Lim, B.; Li, Z.-Y.; Ginger, D. S.; Xia, Y. Synthesis and Optical Properties of Cubic Gold Nanoframes. *Nano Res.* **2008**, *1*, 441−449.
(43) Oh, A.; Baik, H.; Choi, D. S.; Cheon, J. Y.; Kim, B.; Kim, H.; Kwon, S. J.; Joo, S. H.; Jung, Y.; Lee, K. Skeletal Octahedral Nanoframe with Cartesian Coordinates via Geometrically Precise Nanoscale Phase Segregation in a Pt@Ni Core−Shell Nanocrystal. *ACS Nano* **2015**, *9*, 2856−2867.
(44) Park, J.; Sa, Y. J.; Baik, H.; Kwon, T.; Joo, S. H.; Lee, K. Iridium-Based Multimetallic Nanoframe@Nanoframe Structure: An Efficient and Robust Electrocatalyst Toward Oxygen Evolution Reaction. *ACS Nano* **2017**, *11*, 5500−5509.
(45) Yoo, S.; Kim, J.; Choi, S.; Park, D.; Park, S. Two-Dimensional Nanoframes with Dual Rims. *Nat. Commun.* **2019**, *10*, 5789.
(46) Mahmoud, M. A.; Qian, W.; El-Sayed, M. A. Following Charge Separation on the Nanoscale in Cu_2O−Au Nanoframe Hollow Nanoparticles. *Nano Lett.* **2011**, *11*, 3285−3289.
(47) Han, C.; Ge, L.; Chen, C.; Li, Y.; Zhao, Z.; Xiao, X.; Li, Z.; Zhang, J. Site-Selected Synthesis of Novel Ag@AgCl Nanoframes with Efficient Visible Light Induced Photocatalytic Activity. *J. Mater. Chem. A* **2014**, *2*, 12594−12600.
(48) Lou, Z.; Fujitsuka, M.; Majima, T. Two-Dimensional Au-Nanoprism/Reduced Graphene Oxide/Pt-Nanoframe as Plasmonic Photocatalysts with Multiplasmon Modes Boosting Hot Electron Transfer for Hydrogen Generation. *J. Phys. Chem. Lett.* **2017**, *8*, 844−849.
(49) Li, Z.; Yu, R.; Huang, J.; Shi, Y.; Zhang, D.; Zhong, X.; Wang, D.; Wu, Y.; Li, Y. Platinum−Nickel Frame within Metal-Organic Framework Fabricated in situ for Hydrogen Enrichment and Molecular Sieving. *Nat. Commun.* **2015**, *6*, 8248.
(50) Park, J.; Kanti Kabiraz, M.; Kwon, H.; Park, S.; Baik, H.; Choi, S.-I.; Lee, K. Radially Phase Segregated PtCu@PtCuNi Dendrite@Frame Nanocatalyst for the Oxygen Reduction Reaction. *ACS Nano* **2017**, *11*, 10844−10851.
(51) Kwon, H.; Kabiraz, M. K.; Park, J.; Oh, A.; Baik, H.; Choi, S.-I.; Lee, K. Dendrite-Embedded Platinum−Nickel Multiframes as Highly Active and Durable Electrocatalyst Toward the Oxygen Reduction Reaction. *Nano Lett.* **2018**, *18*, 2930−2936.
(52) Liu, W.; Li, L.; Yang, S.; Gao, J.; Wang, R. Self-Assembly of Heterogeneously Shaped Nanoparticles into Plasmonic Metamolecules on DNA Origami. *Chem. - Eur. J.* **2017**, *23*, 14177−14181.
(53) Zhan, P.; Dutta, P. K.; Wang, P.; Song, G.; Dai, M.; Zhao, S.-X.; Wang, Z.-G.; Yin, P.; Zhang, W.; Ding, B.; et al. Reconfigurable Three-Dimensional Gold Nanorod Plasmonic Nanostructures Organized on DNA Origami Tripod. *ACS Nano* **2017**, *11*, 1172−1179.
(54) Xiong, Y.; Wiley, B.; Chen, J.; Li, Z.-Y.; Yin, Y.; Xia, Y. Corrosion-Based Synthesis of Single-Crystal Pd Nanoboxes and Nanocages and Their Surface Plasmon Properties. *Angew. Chem., Int. Ed.* **2005**, *44*, 7913−7917.
(55) Wang, Z.; Wang, H.; Zhang, Z.; Yang, G.; He, T.; Yin, Y.; Jin, M. Synthesis of Pd Nanoframes by Excavating Solid Nanocrystals for Enhanced Catalytic Properties. *ACS Nano* **2017**, *11*, 163−170.
(56) Nosheen, F.; Zhang, Z.-C.; Zhuang, J.; Wang, X. One-Pot Fabrication of Single-Crystalline Octahedral Pt−Cu Nanoframes and Their Enhanced Electrocatalytic Activity. *Nanoscale* **2013**, *5*, 3660−3663.
(57) Han, L.; Liu, H.; Cui, P.; Peng, Z.; Zhang, S.; Yang, J. Alloy Cu_3Pt Nanoframes through the Structure Evolution in Cu-Pt Nanoparticles with a Core-Shell Construction. *Sci. Rep.* **2015**, *4*, 6414.
(58) Chen, S.; Niu, Z.; Xie, C.; Gao, M.; Lai, M.; Li, M.; Yang, P. Effects of Catalyst Processing on the Activity and Stability of Pt−Ni Nanoframe Electrocatalysts. *ACS Nano* **2018**, *12*, 8697−8705.
(59) Ding, J.; Bu, L.; Guo, S.; Zhao, Z.; Zhu, E.; Huang, Y.; Huang, X. Morphology and Phase Controlled Construction of Pt−Ni Nanostructures for Efficient Electrocatalysis. *Nano Lett.* **2016**, *16*, 2762−2767.
(60) Wang, C.; Zhang, L.; Yang, H.; Pan, J.; Liu, J.; Dotse, C.; Luan, Y.; Gao, R.; Lin, C.; Zhang, J.; et al. High-Indexed Pt_3Ni Alloy Tetrahexahedral Nanoframes Evolved through Preferential CO Etching. *Nano Lett.* **2017**, *17*, 2204−2210.
(61) Zhang, Z.-P.; Zhu, W.; Yan, C.-H.; Zhang, Y.-W. Selective Synthesis of Rhodium-Based Nanoframe Catalysts by Chemical Etching of 3d Metals. *Chem. Commun.* **2015**, *51*, 3997−4000.
(62) Park, J.; Kim, J.; Yang, Y.; Yoon, D.; Baik, H.; Haam, S.; Yang, H.; Lee, K. RhCu 3D Nanoframe as a Highly Active Electrocatalyst for Oxygen Evolution Reaction under Alkaline Condition. *Adv. Sci.* **2016**, *3*, 1500252.
(63) Kwon, T.; Jun, M.; Kim, H. Y.; Oh, A.; Park, J.; Baik, H.; Joo, S. H.; Lee, K. Vertex-Reinforced PtCuCo Ternary Nanoframes as Efficient and Stable Electrocatalysts for the Oxygen Reduction Reaction and the Methanol Oxidation Reaction. *Adv. Funct. Mater.* **2018**, *28*, 1706440.
(64) Oh, A.; Sa, Y. J.; Hwang, H.; Baik, H.; Kim, J.; Kim, B.; Joo, S. H.; Lee, K. Rational Design of Pt-Ni-Co Ternary Alloy Nanoframe Crystals as Highly Efficient Catalysts Toward Alkaline Hydrogen Evolution Reaction. *Nanoscale* **2016**, *8*, 16379−16386.
(65) Gruzeł, G.; Arabasz, S.; Pawlyta, M.; Parlinska-Wojtan, M. Conversion of Bimetallic $PtNi_3$ Nanopolyhedra to Ternary PtNiSn Nanoframes by Galvanic Replacement Reaction. *Nanoscale* **2019**, *11*, 5355−5364.
(66) Yang, L.; Zhan, Q.; Wang, Z.; Chen, Q.; Tong, J.; Fang, D.; Xia, L.; Jin, M. Construction of Light-Harvesting System for Enhanced Catalytic Performance of Pd Nanoframes Toward Suzuki Coupling Reaction. *J. Mater. Chem. A* **2017**, *5*, 10150−10153.
(67) McEachran, M.; Keogh, D.; Pietrobon, B.; Cathcart, N.; Gourevich, I.; Coombs, N.; Kitaev, V. Ultrathin Gold Nanoframes through Surfactant-Free Templating of Faceted Pentagonal Silver Nanoparticles. *J. Am. Chem. Soc.* **2011**, *133*, 8066−8069.
(68) Shahjamali, M. M.; Bosman, M.; Cao, S.; Huang, X.; Cao, X.; Zhang, H.; Pramana, S. S.; Xue, C. Surfactant-Free Sub-2 nm Ultrathin Triangular Gold Nanoframes. *Small* **2013**, *9*, 2880−2886.
(69) Sun, X.; Qin, D. Co-Titration of $AgNO_3$ and $HAuCl_4$: A New Route to the Synthesis of Ag@Ag−Au Core−Frame Nanocubes with Enhanced Plasmonic and Catalytic Properties. *J. Mater. Chem. C* **2015**, *3*, 11833−11841.
(70) Tsuji, M.; Kidera, T.; Yajima, A.; Hamasaki, M.; Hattori, M.; Tsuji, T.; Kawazumi, H. Synthesis of Ag−Au and Ag−Pd Alloy Triangular Hollow Nanoframes by Galvanic Replacement Reactions without and with Post-Treatment Using NaCl in an Aqueous Solution. *CrystEngComm* **2014**, *16*, 2684−2691.
(71) Li, J.; Sun, X.; Qin, D. Ag-Enriched Ag-Pd Bimetallic Nanoframes and Their Catalytic Properties. *ChemNanoMat* **2016**, *2*, 494−499.
(72) Xu, L.; Luo, Z.; Fan, Z.; Yu, S.; Chen, J.; Liao, Y.; Xue, C. Controllable galvanic Synthesis of Triangular Ag−Pd Alloy Nanoframes for Efficient Electrocatalytic Methanol Oxidation. *Chem. - Eur. J.* **2015**, *21*, 8691−8695.
(73) Park, J.; Wang, H.; Vara, M.; Xia, Y. Platinum Cubic Nanoframes with Enhanced Catalytic Activity and Durability Toward Oxygen Reduction. *ChemSusChem* **2016**, *9*, 2855−2861.
(74) Ye, H.; Wang, Q.; Catalano, M.; Lu, N.; Vermeylen, J.; Kim, M. J.; Liu, Y.; Sun, Y.; Xia, X. Ru Nanoframes with an fcc Structure and Enhanced Catalytic Properties. *Nano Lett.* **2016**, *16*, 2812−2817.

https://dx.doi.org/10.1021/acs.chemrev.0c00940
Chem. Rev. 2021, 121, 796−833

(75) Zhao, M.; Hood, Z. D.; Vara, M.; Gilroy, K. D.; Chi, M.; Xia, Y. Ruthenium Nanoframes in the Face-Centered Cubic Phase: Facile Synthesis and Their Enhanced Catalytic Performance. *ACS Nano* **2019**, *13*, 7241−7251.
(76) Xie, S.; Lu, N.; Xie, Z.; Wang, J.; Kim, M. J.; Xia, Y. Synthesis of Pd−Rh Core−Frame Concave Nanocubes and Their Conversion to Rh Cubic Nanoframes by Selective Etching of the Pd Cores. *Angew. Chem., Int. Ed.* **2012**, *51*, 10266−10270.
(77) Pei, J.; Mao, J.; Liang, X.; Chen, C.; Peng, Q.; Wang, D.; Li, Y. Ir−Cu Nanoframes: One-Pot Synthesis and Efficient Electrocatalysts for Oxygen Evolution Reaction. *Chem. Commun.* **2016**, *52*, 3793−3796.
(78) Jin, H.; Hong, Y.; Yoon, J.; Oh, A.; Chaudhari, N. K.; Baik, H.; Joo, S. H.; Lee, K. Lanthanide Metal-Assisted Synthesis of Rhombic Dodecahedral MNi (M = Ir and Pt) Nanoframes Toward Efficient Oxygen Evolution Catalysis. *Nano Energy* **2017**, *42*, 17−25.
(79) Ahn, J.; Qin, D. Fabrication of Nanoscale Cage Cubes by Drilling Orthogonal, Intersected Holes through All Six Side Faces of Ag Nanocubes. *Chem. Mater.* **2019**, *31*, 9179−9187.
(80) Hajfathalian, M.; Gilroy, K. D.; Golze, S. D.; Yaghoubzade, A.; Menumerov, E.; Hughes, R. A.; Neretina, S. A Wulff in a Cage: The Confinement of Substrate-Based Structures in Plasmonic Nanoshells, Nanocages, and Nanoframes Using Galvanic Replacement. *ACS Nano* **2016**, *10*, 6354−6362.
(81) Jang, H.-J.; Ham, S.; Acapulco, J. A. I., Jr.; Song, Y.; Hong, S.; Shuford, K. L.; Park, S. Fabrication of 2D Au Nanorings with Pt Framework. *J. Am. Chem. Soc.* **2014**, *136*, 17674−17680.
(82) Ham, S.; Jang, H.-J.; Song, Y.; Shuford, K. L.; Park, S. Octahedral and Cubic Gold Nanoframes with Platinum Framework. *Angew. Chem., Int. Ed.* **2015**, *54*, 9025−9028.
(83) Wu, Y.; Wang, D.; Zhou, G.; Yu, R.; Chen, C.; Li, Y. Sophisticated Construction of Au Islands on Pt−Ni: An Ideal Trimetallic Nanoframe Catalyst. *J. Am. Chem. Soc.* **2014**, *136*, 11594−11597.
(84) Liu, X.; Zhang, F.; Jing, X.; Pan, M.; Liu, P.; Li, W.; Zhu, B.; Li, J.; Chen, H.; Wang, L.; et al. Complex Silica Composite Nanomaterials Templated with DNA Origami. *Nature* **2018**, *559*, 593−−598.
(85) Li, N.; Shang, Y.; Han, Z.; Wang, T.; Wang, Z.-G.; Ding, B. Fabrication of Metal Nanostructures on DNA Templates. *ACS Appl. Mater. Interfaces* **2019**, *11*, 13835−13852.
(86) Vitos, L.; Ruban, A. V.; Skriver, H. L.; Kollár, J. The Surface Energy of Metals. *Surf. Sci.* **1998**, *411*, 186−202.
(87) Yang, T.-H.; Shi, Y.; Janssen, A.; Xia, Y. Surface Capping Agents and Their Roles in Shape-Controlled Synthesis of Colloidal Metal Nanocrystals. *Angew. Chem., Int. Ed.* **2020**, *59*, 15378−15401.
(88) Xia, X.; Wang, Y.; Ruditskiy, A.; Xia, Y. 25_{th} Anniversary Article: Galvanic Replacement: A Simple and Versatile Route to Hollow Nanostructures with Tunable and Well-Controlled Properties. *Adv. Mater.* **2013**, *25*, 6313−6333.
(89) Zhang, L.; Roling, L. T.; Wang, X.; Vara, M.; Chi, M.; Liu, J.; Choi, S. I.; Park, J.; Herron, J. A.; Xie, Z.; et al. Platinum-based Nanocages with Subnanometer-thick Walls and Well-defined, Controllable Facets. *Science* **2015**, *349*, 412−416.
(90) Gilroy, K. D.; Yang, X.; Xie, S.; Zhao, M.; Qin, D.; Xia, Y. Shape-Controlled Synthesis of Colloidal Metal Nanocrystals by Replicating the Surface Atomic Structure on the Seed. *Adv. Mater.* **2018**, *30*, 1706312.
(91) Yousfi-Steiner, N.; Moçotéguy, Ph.; Candusso, D.; Hissel, D. A Review on Polymer Electrolyte Membrane Fuel Cell Catalyst Degradation and Starvation Issues: Causes, Consequences and Diagnostic for Mitigation. *J. Power Sources* **2009**, *194*, 130−145.
(92) Mazumder, V.; Lee, Y.; Sun, S. Recent Development of Active Nanoparticle Catalysts for Fuel Cell Reactions. *Adv. Funct. Mater.* **2010**, *20*, 1224−1231.
(93) Abdalla, A. M.; Hossain, S.; Azad, A. T.; Petra, P. M. I.; Begum, F.; Eriksson, S. G.; Azad, A. K. Nanomaterials for Solid Oxide Fuel Cells: A Review. *Renewable Sustainable Energy Rev.* **2018**, *82*, 353−368.
(94) Zhang, L.; Chang, Q.; Chen, H.; Shao, M. Recent Advances in Palladium-Based Electrocatalysts for Fuel Cell Reactions and Hydrogen Evolution Reaction. *Nano Energy* **2016**, *29*, 198−219.
(95) Zhu, X.; Huang, L.; Wei, M.; Tsiakaras, P.; Shen, P. K. Highly Stable Pt-Co Nanodendrite in Nanoframe with Pt Skin Structured Catalyst for Oxygen Reduction Electrocatalysis. *Appl. Catal., B* **2021**, *281*, 119460.
(96) Wu, Y.; Yi, Y.; Sun, Z.; Sun, H.; Guo, T.; Zhang, M.; Cui, L.; Jiang, K.; Peng, Y.; Sun, J. Bimetallic Fe-Ni Phosphide Carved Nanoframes Toward Efficient Overall Water Splitting and Potassium-ion Storage. *Chem. Eng. J.* **2020**, *390*, 124515.
(97) Nørskov, J. K.; Rossmeisl, J.; Logadottir, A.; Lindqvist, L.; Kitchin, J. R.; Bligaard, T.; Jónsson, H. Origin of the Overpotential for Oxygen Reduction at a Fuel-Cell Cathode. *J. Phys. Chem. B* **2004**, *108*, 17886−17892.
(98) Greeley, J.; Stephens, I. E. L.; Bondarenko, A. S.; Johansson, T. P.; Hansen, H. A.; Jaramillo, T. F.; Rossmeisl, J.; Chorkendorff, I.; Nørskov, J. K. Alloys of Platinum and Early Transition Metals as Oxygen Reduction Electrocatalysts. *Nat. Chem.* **2009**, *1*, 552−556.
(99) Stamenkovic, V. R.; Fowler, B.; Mun, B. S.; Wang, G.; Ross, P. N.; Lucas, C. A.; Marković, N. M. Improved Oxygen Reduction Activity on $Pt_3Ni(111)$ via Increased Surface Site Availability. *Science* **2007**, *315*, 493−497.
(100) Wang, H.; Xu, S.; Tsai, C.; Li, Y.; Liu, C.; Zhao, J.; Liu, Y.; Yuan, H.; Abild-Pedersen, F.; Prinz, F. B.; et al. Direct and Continuous Strain Control of Catalysts with Tunable Battery Electrode Materials. *Science* **2016**, *354*, 1031−−1036.
(101) Wang, L.; Zeng, Z.; Gao, W.; Maxson, T.; Raciti, D.; Giroux, M.; Pan, X.; Wang, C.; Greeley, J. Tunable Intrinsic Strain in Two-Dimensional Transition Metal Electrocatalysts. *Science* **2019**, *363*, 870−874.
(102) Schnur, S.; Groß, A. Strain and Coordination Effects in the Adsorption Properties of Early Transition Metals: A Density-Functional Theory Study. *Phys. Rev. B: Condens. Matter Mater. Phys.* **2010**, *81*, No. 033402.
(103) Luo, M.; Guo, S. Strain-Controlled Electrocatalysis on Multimetallic Nanomaterials. *Nat. Rev. Mater.* **2017**, *2*, 17059.
(104) Wu, J.; Qi, L.; You, H.; Gross, A.; Li, J.; Yang, H. Icosahedral Platinum Alloy Nanocrystals with Enhanced Electrocatalytic Activities. *J. Am. Chem. Soc.* **2012**, *134*, 11880−11883.
(105) Munjewar, S. S.; Thombre, S. B.; Mallick, R. K. Approaches to Overcome the Barrier Issues of Passive Direct Methanol Fuel Cell−Review. *Renewable Sustainable Energy Rev.* **2017**, *67*, 1087−1104.
(106) Li, X.; Faghri, A. Review and Advances of Direct Methanol Fuel Cells (DMFCS) Part I: Design, Fabrication, and Testing with High Concentration Methanol Solutions. *J. Power Sources* **2013**, *226*, 223−240.
(107) Chaudhari, N. K.; Hong, Y.; Kim, B.; Choi, S.-I.; Lee, K. Pt−Cu Based Nanocrystals as Promising Catalysts for Various Electrocatalytic Reactions. *J. Mater. Chem. A* **2019**, *7*, 17183−17203.
(108) Rees, N. V.; Compton, R. G. Sustainable Energy: A Review of Formic Acid Electrochemical Fuel Cells. *J. Solid State Electrochem.* **2011**, *15*, 2095−2100.
(109) Yu, X.; Pickup, P. G. Recent Advances in Direct Formic Acid Fuel Cells (DFAFC). *J. Power Sources* **2008**, *182*, 124−132.
(110) Chen, S.; Su, H.; Wang, Y.; Wu, W.; Zeng, J. Size-Controlled Synthesis of Platinum−Copper Hierarchical Trigonal Bipyramid Nanoframes. *Angew. Chem., Int. Ed.* **2015**, *54*, 108−113.
(111) Saleem, F.; Ni, B.; Yong, Y.; Gu, L.; Wang, X. Ultra-Small Tetrametallic Pt-Pd-Rh-Ag Nanoframes with Tunable Behavior for Direct Formic Acid/Methanol Oxidation. *Small* **2016**, *12*, 5261−5268.
(112) Roger, I.; Shipman, M. A.; Symes, M. D. Earth-Abundant Catalysts for Electrochemical and Photoelectrochemical Water Splitting. *Nat. Rev. Chem.* **2017**, *1*, 3.
(113) Carmo, M.; Fritz, D. L.; Mergel, J.; Stolten, D. A Comprehensive Review on PEM Water Electrolysis. *Int. J. Hydrogen Energy* **2013**, *38*, 4901−4934.
(114) Hu, C.; Zhang, L.; Gong, J. Recent Progress Made in the Mechanism Comprehension and Design of Electrocatalysts for Alkaline Water Splitting. *Energy Environ. Sci.* **2019**, *12*, 2620−2645.
(115) Axet, M. R.; Philippot, K. Catalysis with Colloidal Ruthenium Nanoparticles. *Chem. Rev.* **2020**, *120*, 1085−1145.

https://dx.doi.org/10.1021/acs.chemrev.0c00940
Chem. Rev. 2021, 121, 796−833

(116) Zang, W.; Li, G.; Wang, L.; Zhang, X. Catalytic Hydrogenation by Noble-Metal Nanocrystals with Well-Defined Facets: A Review. *Catal. Sci. Technol.* **2015**, *5*, 2532−2553.
(117) Zhang, L.; Zhou, M.; Wang, A.; Zhang, T. Selective Hydrogenation over Supported Metal Catalysts: From Nanoparticles to Single Atoms. *Chem. Rev.* **2020**, *120*, 683−733.
(118) Fihri, A.; Bouhrara, M.; Nekoueishahraki, B.; Basset, J.-M.; Polshettiwar, V. Nanocatalysts for Suzuki Cross-Coupling Reactions. *Chem. Soc. Rev.* **2011**, *40*, 5181−5203.
(119) Wang, Q.; Domen, K. Particulate Photocatalysts for Light-Driven Water Splitting: Mechanisms, Challenges, and Design Strategies. *Chem. Rev.* **2020**, *120*, 919−985.
(120) Dutta, S. K.; Mehetor, S. K.; Pradhan, N. Metal Semiconductor Heterostructures for Photocatalytic Conversion of Light Energy. *J. Phys. Chem. Lett.* **2015**, *6*, 936−944.
(121) Gellé, A.; Jin, T.; de la Garza, L.; Price, G. D.; Besteiro, L. V.; Moores, A. Applications of Plasmon-Enhanced Nanocatalysis to Organic Transformations. *Chem. Rev.* **2020**, *120*, 986−1041.
(122) Garagounis, I.; Kyriakou, V.; Skodra, A.; Vasileiou, E.; Stoukides, M. Electrochemical Synthesis of Ammonia in Solid Electrolyte Cells. *Front. Energy Res.* **2014**, *2*, 1.
(123) Chen, M. S.; Cai, Y.; Yan, Z.; Gath, K. K.; Axnanda, S.; Goodman, D. W. Highly Active Surfaces for CO Oxidation on Rh, Pd, and Pt. *Surf. Sci.* **2007**, *601*, 5326−5331.
(124) Joo, S. H.; Park, J. Y.; Tsung, C.-K.; Yamada, Y.; Yang, P.; Somorjai, G. A. Thermally Stable Pt/Mesoporous Silica Core−Shell Nanocatalysts for High-Temperature Reactions. *Nat. Mater.* **2009**, *8*, 126−131.
(125) Rood, S.; Eslava, S.; Manigrasso, A.; Bannister, C. Recent Advances in Gasoline Three-Way Catalyst Formulation: A Review. *Proc. Inst. Mech. Eng., Part D* **2020**, *234*, 936−949.
(126) Beermann, V.; Gocyla, M.; Willinger, E.; Rudi, S.; Heggen, M.; Dunin-Borkowski, R. E.; Willinger, M.-G.; Strasser, P. Rh-Doped Pt−Ni Octahedral Nanoparticles: Understanding the Correlation between Elemental Distribution, Oxygen Reduction Reaction, and Shape Stability. *Nano Lett.* **2016**, *16*, 1719−1725.
(127) Huang, X.; Zhao, Z.; Cao, L.; Chen, Y.; Zhu, E.; Lin, Z.; Li, M.; Yan, A.; Zettl, A.; Wang, Y. M.; et al. High-Performance Transition Metal−Doped Pt_3Ni Octahedra for Oxygen Reduction Reaction. *Science* **2015**, *348*, 1230−1234.
(128) Wang, S.; Xiong, L.; Bi, J.; Zhang, X.; Yang, G.; Yang, S. Structural and Electronic Stabilization of PtNi Concave Octahedral Nanoparticles by P Doping for Oxygen Reduction Reaction in Alkaline Electrolytes. *ACS Appl. Mater. Interfaces* **2018**, *10*, 27009−27018.
(129) Chi, M.; Wang, C.; Lei, Y.; Wang, G.; Li, D.; More, K. L.; Lupini, A.; Allard, L. F.; Markovic, N. M.; Stamenkovic, V. R. Surface Faceting and Elemental Diffusion Behaviour at Atomic Scale for Alloy Nanoparticles During In Situ Annealing. *Nat. Commun.* **2015**, *6*, 8925.
(130) Han, B.; Carlton, C. E.; Kongkanand, A.; Kukreja, R. S.; Theobald, B. R.; Gan, L.; O'Malley, R.; Strasser, P.; Wagner, F. T.; Shao-Horn, Y. Record Activity and Stability of Dealloyed Bimetallic Catalysts for Proton Exchange Membrane Fuel Cells. *Energy Environ. Sci.* **2015**, *8*, 258−266.
(131) Zhao, J.; Cheng, X.; Zhao, G.; Lu, Y.; Wang, Y.; Wang, H.; Chen, H. Ag Nanoframes: Controllable Reduction of $AgCl_xBr_{1-x}$ Nanocubes. *Chem. Commun.* **2019**, *55*, 5571−5574.
(132) Li, P.; Han, Y.; Zhou, X.; Fan, Z.; Xu, S.; Cao, K.; Meng, F.; Gao, L.; Song, J.; Zhang, H.; et al. Thermal Effect and Rayleigh Instability of Ultrathin 4H Hexagonal Gold Nanoribbons. *Matter* **2020**, *2*, 658−665.
(133) Gilroy, K. D.; Elnabawy, A. O.; Yang, T.-H.; Roling, L. T.; Howe, J.; Mavrikakis, M.; Xia, Y. Thermal Stability of Metal Nanocrystals: An Investigation of the Surface and Bulk Reconstructions of Pd Concave Icosahedra. *Nano Lett.* **2017**, *17*, 3655−3661.
(134) Ma, J.; Lee, S. M.-Y.; Yi, C.; Li, C.-W. Controllable Synthesis of Functional Nanoparticles by Microfluidic Platforms for Biomedical Applications − a Review. *Lab Chip* **2017**, *17*, 209−226.
(135) Niu, G.; Ruditskiy, A.; Vara, M.; Xia, Y. Toward Continuous and Scalable Production of Colloidal Nanocrystals by Switching from Batch to Droplet Reactors. *Chem. Soc. Rev.* **2015**, *44*, 5806−5820.

https://dx.doi.org/10.1021/acs.chemrev.0c00940
Chem. Rev. 2021, 121, 796−833